Master's Thesis

Modelling the aerotaxis of *Shewanella oneidensis*

Modellierung der Aerotaxis von *Shewanella oneidensis*

prepared by

Henning Zwirnmann

from Witten

at the Max-Planck Institute for Dynamics and Self-Organization

Thesis period:	30 April 2015 until 29 October 2015
Supervisor:	Dr. Marco G. Mazza
Second referee:	Prof. Dr. Stephan Herminghaus

Abstract

Shewanella oneidensis (*S.o.*) are a species of bacteria that can adapt to a broad variety of living conditions. This includes both aerobic and anaerobic environments and renders them interesting not only for scientific purposes, but also from an industrial point of view: They can be component of microbial fuel cells or facilitate bioremediation of water. In this work, we perform molecular dynamics simulations of particles representing these bacteria to analyse their behaviour in an aerobic environment. Due to their oxygen consumption, a gradient in this concentration is established in the system, which in turn leads to the formation of a so-called *aerotactic band*. We study the dependence of the bacterial dynamics on different physical parameters and quantify changes the system undergoes by means of correlation functions.

Zusammenfassung

Shewanella oneidensis (*S.o.*) sind eine Spezies von Baktieren, die unter unterschiedlichsten Lebensbedingungen überleben können. Dies beinhaltet vor allem sowohl aerobe als auch anaerobe Umgebungen und macht *S.o.* nicht nur von einem wissenschaftlichen Standpunkt aus interessant, sondern auch nützlich für industrielle Zwecke: So können sie mutmaßlich als Bestandteile einer "lebenden" Batterie oder zur Wiederaufbereitung von verschmutztem Wasser dienen. In dieser Arbeit führen wir numerische Experimente mit *S.o.* durch, indem wir mittels von Molekulardynamiksimulationen das Verhalten von Bakterien in einem aeroben System modellieren. Dadurch, dass sie Sauerstoff verbrauchen, stellt sich ein Konzentrationsgradient im System ein, welcher wiederum zur Bildung einer speziellen Struktur, des sogenannten *aerotaktischen Bandes*, führt. Wir variieren verschiedene Parameter und quantifizieren Veränderungen im System mittels geeigneter Korrelationsfunktionen.

Contents

List of Figures

1. Introduction

Many biological microorganisms have evolved mechanisms that allow them to propagate actively through their environment. Only by this means they can explore it effectively and react to stimuli they sense therein. Microorganisms with this feature are also called *active swimmers* and include amoeba, bacteria or other kinds of living cells. While this mechanism has been known and under research for almost 100 years (see e.g. [1]), the modelling of the dynamics of active swimmers in the face of statistical physics is a rather new branch. Starting with the seminal work of Vicsek [2], it has attracted remarkable interest in the last 20 years. These systems are intrinsically in a nonequilibrium state. They differ from boundary-driven nonequilibrium systems studied in the past as the driving and dissipation occur at the scale of the individual particle.

The aim of the project is to numerically simulate a system of active swimmers and reproduce behaviour and phenomenology of real bacteria in an experiment. To this end, we implement a set of rules governing their dynamics in a molecular dynamics (MD) simulation that originate from experimental observations. Here we especially focus on the interplay of the bacteria with the oxygen dissolved in the system. Figure 1.1 shows the simulation setup: The bacteria are confined to a flat volume, i.e. between two microscopic slides. In the centre of the system a cylinder resembles an air bubble from which oxygen diffuses into the surrounding medium

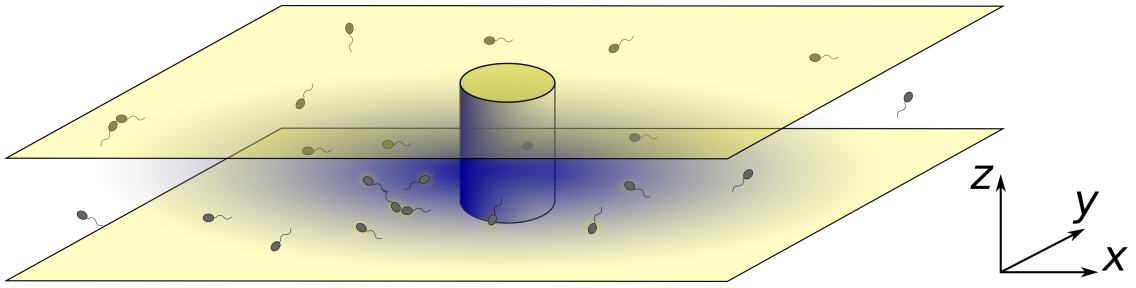

Figure 1.1.: Simulation setup: particles swim confined to the volume between two walls. The blue overlay around the cylinder in the centre indicates the diffusing oxygen

(not shown in the drawing).

The real counterpart to our model particles is a species of bacteria called *Shewanella oneidensis* (*S.o.*). They are capable of exchanging electrons with their environment and thus respiring outside their cell membrane. By this means these bacteria are able to live under either aerobic or anaerobic conditions. Apart from biological, biochemical and physical interests this feature renders *S.o.* also interesting for industrial use, e.g. in microbial fuel cells and wastewater management [3]. By comparing the results from our simulations to the real experiments we hope to be able to make further progress understanding the behaviour of the bacteria and the parameters the latter depends on.

This thesis is structured in the following way: In Chap. 2, we first describe the biological and biochemical fundamentals of *Shewanella oneidensis* (Chap. 2.1) as well as the basic ansatzes to analyse their dynamics from the point of view of non-equilibrium statistical physics (Chap. 2.2). Chapter 3 deals with the physical model and the equations of motion that are at the bottom of our MD simulations. We then describe how we implement these equations in the actual program code in Chap. 4. In the following chapter (Chap. 5) we present the simulation results and show how the system behaves while varying our model parameters. We conclude this work with the summary and the outlook in Chap. 6.

2. Theory

2.1. The model organism: *Shewanella oneidensis*

Shewanella is a genus of monotrichous, Gram-negative and rod-shaped bacteria typically living in aquatic environments (see Fig. 2.1). The species *Shewanella oneidensis* (*S.o.*) was first described in 1999 [4], named after Oneida Lake in New York state, US, where the first sample was collected. They are bacteria with typical lengths between $2-3$ µm and diameters of $0.4-0.7$ µm [3]. The special interest in *S.o.* from a scientific point of view arises from the fact that they can live in both aerobic and anaerobic surroundings, which renders them *facultatively anaerobic bacteria*. *S.o.* implements the electron pump mechanism on their outer cellular membrane. They have evolved several breathing mechanisms enabling them to target metal oxides, in addition to oxygen, as electron acceptors. Also, the bacteria can form biofilms or congregate dynamically in vicinity of a suitable acceptor [5]. Because of their capability to exchange electrons with the environment outside their body (therefore the term "exoelectrogen") they can conceivably be used in microbial fuel cells (*MFCs*) [6]. The same property makes them also interesting for wastewater treatment: When the bacteria target e.g. soluble uranium(VI) as an electron acceptor, it is reduced to insoluble uranium(IV) which precipitates and can thus kept away from the water cycle. The full genome was sequenced in 2002 [7], which both allowed to gain deep insights into basic biochemical mechanisms and facilitated further research.

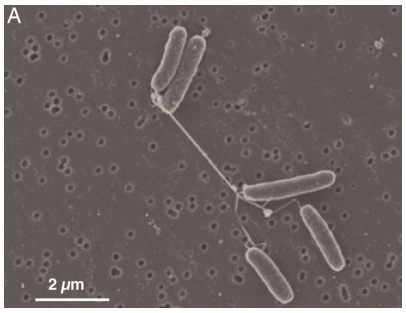

Figure 2.1.: SEM image of *S.o.* forming nanowires [8]

2.1.1. Flagellar motion and movement mechanisms

As we said above, *S.o.* are a monotrichous species, i.e. they have a single polar flagellum. Because of this they are typical "pusher" bacteria where counterclockwise rotation of the flagellum produces forward propagation, while clockwise rotation leads to rearward movement, i.e. in the direction of the flagellum itself. Bacteria using only these two mechanisms for propagation employ a so-called "run-reverse" strategy: After a time of forward movement they reverse the rotation direction of their flagella, thus moving backward, before they reverse once more. Slight changes from the original direction result from rotational diffusion and, possibly, an external flow field [9]. *Shewanella putrefaciens* and probably other *Shewanella* species, such as *S.o.*, follow a "run-reverse-flick" mechanism [10]: At the transition between backward and forward movements they flick their flagellum once afterwards, thus turning around with an average turning angle of around 90 degrees (see Fig. 2.2). This behaviour is considered to be especially advantageous during chemotaxis (see Chap. 2.1.3) [11–13].

In contrast to *S.o.*, *Escherichia coli*, the classical bacterial model organism, perform a "run-and-tumble" strategy. *E.coli* are a peritrichous species, i.e. they have several flagella distributed all over the body that rotate counterclockwise in the "run" phase. Sometimes one or more flagella reverse their rotation and thus account for a "tumbling" event with the bacterium rotating its body in a random direction without propagating. Afterwards another run phase starts [14]. The tumbling frequency depends on the environment: *E.coli* have been found to perform prolonged run phases swimming along a favourable chemical gradient, e.g. towards a nutrient [15]. Thus this mechanism is strongly related to chemotaxis, too.

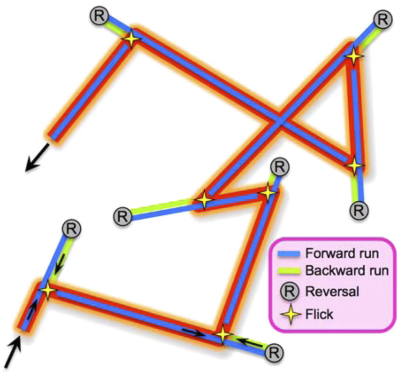

Figure 2.2.: Run-reverse-flick motion pattern [11]

2.1.2. Respiration mechanisms

Respiration on its most fundamental level means donating one's terminal metabolic electrons: Humans breathe air that contains oxygen, which is a good electron acceptor and thus can be reduced easily in our mitochondria. Since bacteria do not have mitochondria they have evolved different mechanisms to respire: *S.o.* prefer to reduce oxygen dissolved in their environment, but can also live under anaerobic conditions. There are several ways of extracellular electron transport allowing them to reduce insoluble electron acceptors (IEA), including metal oxides such as Fe(III) or Mn(IV) (see Fig. 2.3) [3]:

- *Cytochromes* are special proteins that reside on the outer cell membrane. These facilitate electron transfer to a metal oxide particle that is in direct contact with the bacterium [16] (see Fig. 2.3 A).
- *Bacterial nanowires* are electrically conductive filaments appended to the outer cell membrane of the bacteria. Their length is of nanometer-scale with electron transport rates of roughly 10^6/s and resistivities of around $1\,\Omega\,\mathrm{cm}$ [8, 17] (see Fig. 2.3 B).
- Organic compounds called *chelators* bind to soluble electron acceptors, thus facilitating intra- or extracellular electron transfer [18] (see Fig. 2.3 C).
- *Flavins*, another kind of organic compounds, serve as electron shuttles transporting electrons to an IEA. In contrast to the transfer via cytochromes the individual does not need to contact the IEA directly to employ this pathway [19] (see Fig. 2.3 D).

2.1.3. *Taxis*, *kinesis* and *biofilms*

Taxis (from Greek τάξις, "arrangement, order") is a behaviour found in many animal species characterized by directed movement along a varying external stimulus. Several mechanisms have been described, e.g. *chemotaxis* (along chemical gradients [21]), *phototaxis* (along gradients in light intensity [22]) and *magnetotaxis* (along a gradients in magnetic fields [23]). Besides chemotaxis during nutrient search *S.o.* also perform *aerotaxis*, i.e. they look for an ideal oxygen concentration in their environment. To do so, they use special proteins in their outer membrane that measure and compare said concentration at different points in time. Due to their small size

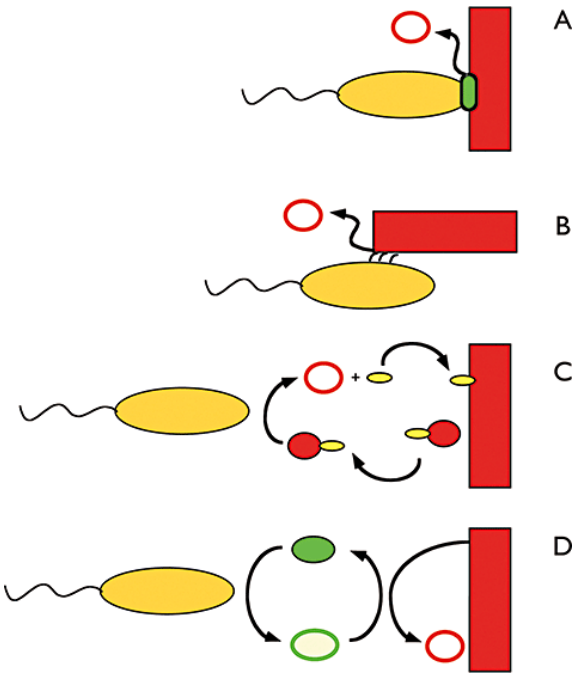

Figure 2.3.: Extracellular respiration mechanisms: bacterium (orange oval), IEA (red rectangle), reduced IEA particle (open red circle) [20]

comparing concentrations simultaneously at different positions (*tropotaxis*) is not possible because fluctuations are not detectable on that length scale.

Aerotaxis can finally lead to the formation of the so-called "aerotactic band", which is a region of high bacterial density with high motility. Figure 2.4 shows the formation of an aerotactic band in a colony of *S.o.* for two cases: When the oxygen concentration at the meniscus is 100 %, the band develops at a bigger distance from it than when the oxygen is only at air level (21 %). This indicates that there is an ideal oxygen concentration where the bacteria stay preferably. The earliest descriptions of similar behaviour in bacteria are due to observations by Engelmann (1881, [24]) and Beijerinck (1893, [25]).

While directed movement due to a stimulus and its gradient is called *taxis*, the

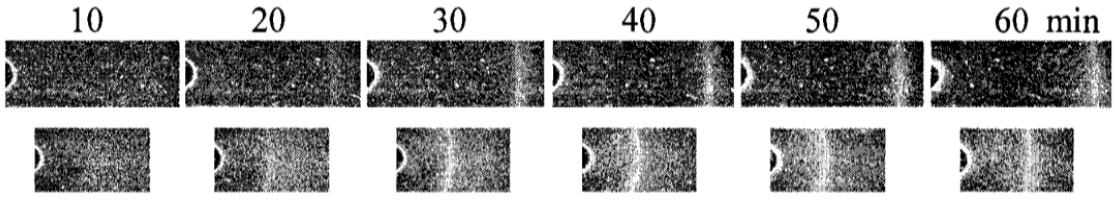

Figure 2.4.: Formation of an aerotactic band. The oxygen concentration at the meniscus (left side) is 100 % (upper panel) and 21 % (lower panel), respectively. [26]

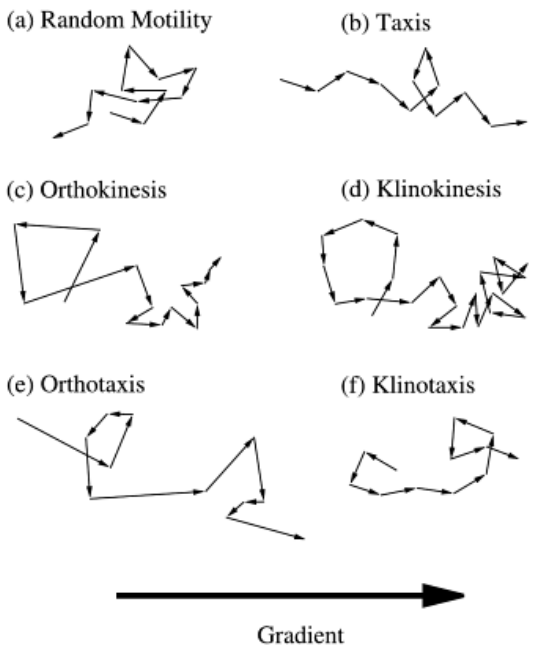

Figure 2.5.: Comparison of *taxis* and *kinesis* [28]

term *kinesis* (from Greek κίνεσις, "movement") describes undirected movement due to the stimulus intensity. This may involve both changes in speed (*orthokinesis*) or turning frequency (*klinokinesis*) [27]. Hence, we can say the process governing the formation of the aerotactic band is primarily dominated by either klinotaxis or -kinesis. The different mechanisms are depicted in Fig. 2.5.

S.o. have been found to perform *electrokinesis* in an anaerobic environment in the presence of an IEA, including both speed variations and abrupt reversals of the

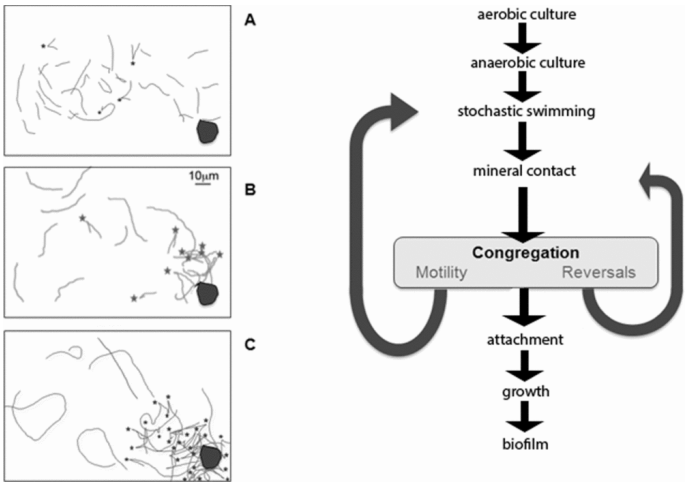

Figure 2.6.: Scheme of *S.o.* congregating near an IEA. The black stars in the left pictures mark a reversal event. [29]

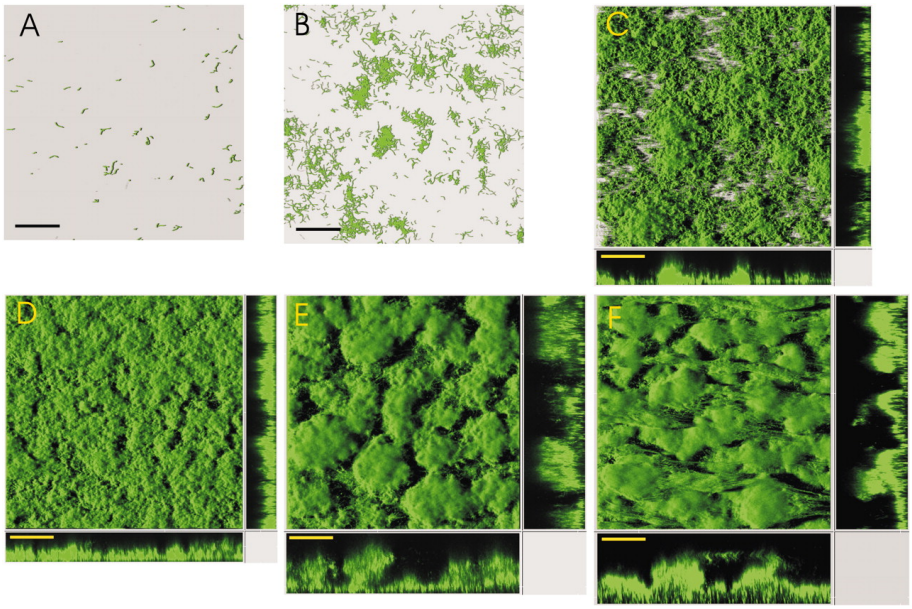

Figure 2.7.: Biofilm formation of *S.o.* on a glass surface in a flow chamber [5]

direction of motion [29, 30]. However, in this case, no chemoattractant is involved, but the behaviour is dependent on the time passed since the last contact to the acceptor. It finally leads to a congregation of the bacteria in vicinity to the IEA as sketched in Fig. 2.6.

Figure 2.6 also points out that the bacteria not only congregate close to an IEA, but finally attach to it and form a biofilm. In contrast to the previously described, dynamic situations, they now become static and form a network as can be seen in Fig. 2.7. In order to respire they can now make use of any of the mechanisms for extracellular electron transport described in Chap. 2.1.2 [5].

2.2. Nonequilibrium statistical physics

The studies of systems with a large number of particles in their equilibrium was a main task dealt with by physicists such as Maxwell, Boltzmann and Gibbs in the second half of the 19th and the early 20th century. They provided a theoretical foundation for thermodynamics that was up to then mostly based on empirical observations. In contrast to that, nonequilibrium statistical physics, i.e. the description of how particles behave when the system is not in an equilibrium state, is a rather new branch with no such general framework. Several approaches exist, though, some of which we will describe and apply to our model. We focus especially on the mutual interaction of a particle density and the concentration of a chemoattractant.

Without loss of generality we consider the case of one-dimensional motion if not mentioned otherwise. There are various ways to deduce the following equations. Our description is loosely based on [14], [31] and [32].

2.2.1. Langevin equation for Brownian particles

We begin by studying a Brownian particle in a simple fluid in one dimension, i.e. we deal with a passive particle whose motion is strongly influenced by the surrounding bath. Its mesoscopic equation of motion thus reads

$$m\dot{v} = -\gamma v + F_{\text{fluct}} \ . \tag{2.1}$$

The right-hand side is composed of two parts: viscous damping with coefficient γ, which leads to an exponential slowdown of the particle, and a randomly fluctuating force F_{fluct}. Both are due to collisions of the swimmer with the fluid molecules. Based on the nature of F_{fluct} we can postulate two properties:

$$\langle F_{\text{fluct}}(t)\rangle = 0, \tag{2.2}$$

$$\langle F_{\text{fluct}}(t)F_{\text{fluct}}(t')\rangle = \Gamma\delta(t-t'), \tag{2.3}$$

where $\delta(t)$ is Dirac's delta function. These equations imply that we interpret F_{fluct} as a stochastic force: Its average vanishes and collisions are uncorrelated in time (Γ is a constant). These properties make F_{fluct} a so-called *Langevin force* and Eq. (2.1) a *Langevin equation* for v, respectively. If we further postulate that all cumulants of F_{fluct} higher than the second are zero, we call F_{fluct} a *Gaussian white noise* and have thus fully determined the process. Pictorially the force can be imagined as a δ-function accelerating particles in an instant.

Making use of the equipartition theorem one can conclude from the velocity correlation function $\langle v(t)v(t')\rangle$ that Γ in Eq. (2.3) is related to the damping coefficient γ in Eq. (2.1):

$$\Gamma = \gamma k_{\text{B}}T. \tag{2.4}$$

This is a very simple version of a *fluctuation-dissipation theorem* connecting the fundamental microscopic property Γ to the macroscopic quantity γ. Furthermore it is possible to express the mean square displacement $\langle(x(t)-x(0))^2\rangle$ in terms of the

velocity correlation function. With the definition of the diffusion coefficient,

$$D \equiv \lim_{t\to\infty} \frac{\langle (x(t) - x(0))^2 \rangle}{2t}, \tag{2.5}$$

one can then obtain the so-called *Stokes-Einstein relation*

$$D = \frac{k_B T}{\gamma}. \tag{2.6}$$

2.2.2. Equations of motion for active swimmers

The simple Langevin Eq. (2.1) can serve as a basis to describe the motion of our bacteria. There are fundamental differences, though, that shall be highlighted in the following, together with their consequences.

We can make use of Eq. (2.6) to compute the theoretically expected diffusion coefficient for a bacterium: Assuming that Stokes' law ($\gamma = 6\pi\eta a$) is valid, which is a good assumption at low Reynolds numbers as in our case (see below), and inserting the viscosity of water $\eta = 10^{-3}\,\mathrm{kg\,m^{-1}\,s^{-1}}$, the particle diameter $a = 2\,\mu\mathrm{m}$ and a typical temperature of $T = 293\,\mathrm{K}$ yields $D \approx 0.11\,\mu\mathrm{m^2\,s^{-1}}$. This is far below the actually observed value for bacteria similar to *S.o.*: *Vibrio alginolyticus*, another monotrichous bacterium performing run-reverse-flick locomotion, has a diffusivity of $D = 220\,\mu\mathrm{m^2\,s^{-1}}$[11]. In other words, if *V. alginolyticus* diffused according to the fluctuation-dissipation theorem, we would expect a temperature of more than 500 000 K. Hence, they cannot be treated as simple Brownian particles.

This difference results from the fact that these bacteria are by no means passive particles but instead can propagate actively using their flagellum, as described in Chap. 2.1. They gain energy needed for this active locomotion from their environment, which is why they make use of chemo- and aerotaxis (see Chap. 2.1.3). Hence, we do not expect the ensemble-averaged velocity $v(t)$ to decay to zero exponentially with time as for Brownian particles. Instead it should stay at a constant value v_0 for every particle, depending on its internal energy, as long as resources are available, which we typically assume. In contrast to the speed, the orientation e of a particle can change naturally due to e.g. noise or collisions.

Another fact that makes our system differ from passive Brownian particles concerns inertia: If one calculates the Reynolds number $\mathcal{R} \equiv av/\nu$ for the situation at hand (particle diameter $a \approx 1\,\mu\mathrm{m}$, speed $v \approx 10\,\mu\mathrm{m\,s^{-1}}$ and kinematic viscosity $\nu \approx 10^6\,\mu\mathrm{m\,s^{-2}}$ of water) one arrives at values of $\mathcal{R} \approx 10^{-5}$, which is indeed very

small. As $\mathcal{R}$ indicates the ratio of inertial to viscous forces we conclude that the former do not play a role for our particles. In fact if a bacterium with initial speed $v = 30\,\mu\mathrm{m\,s}^{-1}$ stops its flagellum, it will only move roughly $10^{-11}\,\mathrm{m}$ before it comes to rest [33]. Hence, we can safely neglect the inertia term in Eq. (2.1). We do not consider acceleration due to gravity, either, because its effects are even smaller as the bacterial mass density is typically only slightly bigger than that of water.

Based on these considerations we arrive at two equations governing the dynamics of our active swimmers:

$$\frac{\mathrm{d}x}{\mathrm{d}t} = v_0 e(t), \tag{2.7}$$

$$\frac{\mathrm{d}e}{\mathrm{d}t} = F_{\mathrm{fluct}} + F_{\mathrm{ext}}, \tag{2.8}$$

which is a deterministic equation for the position x and a Langevin equation for the orientation e. The additional term F_{ext} accounts for other force contributions, e.g. inter-particle forces, as mentioned previously.

2.2.3. Fokker-Planck and diffusion equation

Instead of describing the dynamics of a particle by solving its microscopic equations of motion one can also focus on the statistics of the particle's position. One possibility to do so is to describe the temporal evolution of the particle probability distribution function $p(x,t)$ under influence of drift and diffusion in the system. This is determined by a *Fokker-Planck equation*, which in one dimension reads:

$$\frac{\partial p(x,t)}{\partial t} = -\frac{\partial}{\partial x}\left(A(x)p(x,t)\right) + \frac{1}{2}\frac{\partial^2}{\partial x^2}\left(B(x)p(x,t)\right). \tag{2.9}$$

$A(x)$ and $B(x)$ describe the strength of drift and diffusion, respectively, and may themselves depend on the spatial coordinate. $p(x,t)$ is related to the actual particle density $n(x,t)$ by means of the relation $n(x,t) = N_{\mathrm{part}}\; p(x,t)$ where N_{part} is the total number of particles. Given the data from our observations we can approximate N_{part} in fact as constant during one experiment as there is almost no cell division or death on our time scale. One can show that this treatment is indeed equivalent to the description via a Langevin equation with noise term F_{fluct} as described in Chap. 2.2.1, i.e. the solutions $x(t)$ are identical. During the proof of this equivalence one has to overcome difficulties regarding F_{fluct} which are at the core of the so-called *Itô-Stratonovich dilemma*.

If we assume that both A and B in Eq. (2.9) no longer depend on space we arrive at a *drift-* (or *advection-*) *diffusion equation*:

$$\frac{\partial p(x,t)}{\partial t} = -A\frac{\partial}{\partial x}p(x,t) + \frac{1}{2}B\frac{\partial^2}{\partial x^2}p(x,t). \tag{2.10}$$

This equation is related to Fick's law of diffusion if we furthermore assume that there is no drift in the system ($\Rightarrow A = 0$):

$$\frac{\partial p(x,t)}{\partial t} = D\frac{\partial^2}{\partial x^2}p(x,t). \tag{2.11}$$

Here we have inserted the classical diffusion coefficient $D \equiv B/2$. We can make use of this equation to describe the evolution of the oxygen concentration $c(x,t)$ in our system. To this end, we multiply by the total initial oxygen concentration C_0 first (similarly to what is done above with N_{part}). Furthermore we must add a term that accounts for bacterial oxygen consumption, i.e. $\int_V c(x,t)\mathrm{d}x \neq C_0$ for $t > t_0$ in general. We choose the consumption term to be proportional to the particle density n itself, thus yielding

$$\frac{\partial c(x,t)}{\partial t} = D\frac{\partial^2}{\partial x^2}c(x,t) - \kappa\theta(c(x,t))n(x,t). \tag{2.12}$$

We identify κ as *bacterial consumption rate*, which can be determined experimentally, too. The added term also contains the Heaviside function $\theta(c)$ that accounts for the fact that the bacteria only consume oxygen if there is any at all. We also know that $D = 2 \times 10^3\,\mu\mathrm{m}^2\,\mathrm{s}^{-1}$ is in fact constant, being the diffusion rate of dissolved oxygen in water [34].

2.2.4. Velocity-jump processes

Another approach to describe cell motility is by means of a *linear transport equation* as done in [32], [35] and [36]. It is based on a mass balance equation, but also takes into account cell velocity and stochastic reorientations. The latter are modelled as a Poisson process with frequency λ, thus yielding

$$\frac{\partial p(\boldsymbol{x},\boldsymbol{v},t)}{\partial t} + \boldsymbol{v}\cdot\boldsymbol{\nabla}p(\boldsymbol{x},\boldsymbol{v},t) = -\lambda p(\boldsymbol{x},\boldsymbol{v},t) + \lambda\int T(\boldsymbol{v},\boldsymbol{v}')p(\boldsymbol{x},\boldsymbol{v}',t)\mathrm{d}\boldsymbol{v}', \tag{2.13}$$

where $\boldsymbol{\nabla}$ only acts as a spatial derivative operator. $p(\boldsymbol{x}, \boldsymbol{v}, t)$ hence describes the probability of finding a particle with velocity $\boldsymbol{v}$ at $(\boldsymbol{x}, t)$. $T(\boldsymbol{v}, \boldsymbol{v}')$ is the reorientation kernel defining the probability for a jump from $\boldsymbol{v}'$ to $\boldsymbol{v}$ given the jump actually occurs. Therefore T is normalized such that $\int T(\boldsymbol{v}, \boldsymbol{v}')\mathrm{d}\boldsymbol{v} = 1 \; \forall \; \boldsymbol{v}'$.

For a simple one-dimensional case we can show that the diffusion equation follows immediately from the transport equation (2.13). To that end we assume that both λ and v are constant, so the only possible velocities are $\pm v_0$. We define a probability p^l for particles moving to the left and p^r to the right:

$$\frac{\partial p^l(x,t)}{\partial t} + v_0 \frac{\partial p^l(x,t)}{\partial x} = -\lambda p^l(x,t) + \lambda p^r(x,t), \tag{2.14}$$

$$\frac{\partial p^r(x,t)}{\partial t} - v_0 \frac{\partial p^r(x,t)}{\partial x} = -\lambda p^r(x,t) + \lambda p^l(x,t). \tag{2.15}$$

By adding and subtracting Eq. (2.14) and (2.15) it follows that the total particle density $p(x,t) = p^r(x,t) + p^l(x,t)$ and the particle probability flux $j(x,t) = v_0(p^r(x,t) - p^l(x,t))$ obey the equations

$$\frac{\partial p}{\partial t} + \frac{\partial j}{\partial x} = 0, \tag{2.16}$$

$$\frac{\partial j}{\partial t} + 2\lambda j = -v_0^2 \frac{\partial p}{\partial x}. \tag{2.17}$$

Taking the spatial derivative of Eq. (2.17) and using Eq. (2.16) yields the *telegraph equation*:

$$\frac{\partial^2 p(x,t)}{\partial t^2} + 2\lambda \frac{\partial p(x,t)}{\partial t} = v_0^2 \frac{\partial^2 p(x,t)}{\partial x^2}. \tag{2.18}$$

From this again follows the classical Fickian diffusion equation (Eq. (2.11)) in the limit $\lambda \to \infty$, $v_0 \to \infty$, $v_0^2/2\lambda \equiv D$.

We can tailor the ansatz (2.13) to our model by specifying how λ and T have to look like: In our case λ must depend on the motility rule we choose. In Chap. 3 we describe three different variants where λ can be function of particle coordinate or rather oxygen concentration at that position, speed and orientation. Independently of that choice we know that T has to be of the form $T(\boldsymbol{v}, \boldsymbol{v}') = \delta(\boldsymbol{v}_{xy} + \boldsymbol{v}'_{xy})$. Here the index xy describes the velocity in the x-y plane because a velocity jump event always leads to an orientation change in that plane.

2.2.5. Chemotaxis equation

The typical way to describe the diffusion of the density of a bacterial species $a(\boldsymbol{x}, t)$ influenced by a chemoattractant with concentration $\rho(\boldsymbol{x}, t)$ is by means of the *Keller-Segel* approach. In 1970 they analysed aggregations in a species of amoeba (*Dictyostelium discoideum*) due to a chemical (*acrasin*) [37]. Their considerations are based on the conservation of the number of amoeba as well as several assumptions regarding diffusion and production of said chemical, thus yielding four equations for the temporal evolution. Further simplifications allowed them to exclude an intermediate product and an enzyme from the system of equations, which finally lead to the *chemotaxis* or *Patlak-Keller-Segel-Alt (PKSA) equation*

$$\frac{\partial a}{\partial t} = -\boldsymbol{\nabla} \cdot \left(\frac{\delta \cdot a}{\rho} \boldsymbol{\nabla} \rho \right) + \boldsymbol{\nabla} \cdot (D_2 \boldsymbol{\nabla} a), \tag{2.19}$$

where δ is a constant. We see that the second term on the right-hand side describes the regular diffusion of cells with coefficient D_2 that might depend on a or ρ itself. The first term of the right-hand side governs the interaction of amoeba and chemical by generating a flux towards high acrasin concentrations (provided $\delta > 0$). In [32] the authors show how the PKSA equation follows from the linear transport equation (Eq. (2.13)) by imposing restrictions on the reorientation kernel T or the turning rate λ.

The equation for a is complemented by another equation for ρ,

$$\frac{\partial \rho}{\partial t} = -\frac{kK}{1 + K\rho} \rho + a f(\rho) + D_\rho \boldsymbol{\nabla}^2 \rho, \tag{2.20}$$

with constants k, K and D_ρ, and $af(\rho)$ accounting for amoebal production of acrasin.

In the derivation of Eq. (2.19) the authors argue that the part of the amoeba flux due to acrasin has to be proportional to its gradient, analogously to the flux of heat being dependent on temperature gradient. However, this assumption is only valid when spatial variations in the latter are reasonably small. This might not be justified in our system because a large bacterial density as is the case inside the aerotactic band leads to a steep gradient. Hence, we cannot make use of the PKSA equation to model our system.

2.2.6. Solutions to the diffusion equation

In this chapter we want to find out what kind of solutions for $\rho(x)$ we can expect. To this end, we assume that the diffusion equation (Eq. (2.11)) holds with a diffusion rate $D \equiv D(x)$ that is space-dependent. For this case, the equation reads

$$\frac{\partial \rho(x,t)}{\partial t} = \frac{\partial}{\partial x}\left(D(x)\frac{\partial}{\partial x}\rho(x,t)\right). \tag{2.21}$$

We suppose that the form of the diffusion rate is as follows:

$$D(x) = D_0 + k\tanh(x_0 - x). \tag{2.22}$$

The parameter x_0 represents the interface of the oxygen-rich region: This shape of $D(x)$ yields high particle diffusion for $x < x_0$ and low diffusion for $x > x_0$ with control parameters D_0 and k. The first region can be identified with an aerobic environment where particles have high speed and reverse their orientation rarely, whereas the second regime stands for anaerobic surroundings with low speed and frequent turning, thus accounting for a low diffusion. We will later show that these assumptions are indeed justified (see Chap. 5.2.6).

To simplify eq. (2.21) further, we focus on its steady-state solutions, hence $\frac{\partial \rho}{\partial t} = 0$. After inserting Eq. (2.22) into it one can easily find the solution

$$\rho(x) = \frac{c_1}{k-1} e^{\frac{D_0(k-1)(x_0-x)}{D_0^2-k^2}} \left(D_0\cosh(x_0-x) + k\sinh(x_0-x)\right)^{\frac{(k-1)k}{k^2-D_0^2}} + c_2 \tag{2.23}$$

with two integration constants c_1 and c_2. We plot Eqs. (2.22) and (2.23) for $c_1 = 1$, $c_2 = 0$, $k = 7$, $D_0 = 10$ and for two values of the oxygen interface $x_0 = 5$ and $x_0 = 10$, respectively, in Fig. 2.8. One can see that ρ peaks approximately at x_0, while it drops steeply down to 0 for $x > x_0$ and to a value larger than zero for $x < x_0$ in the interval considered. Varying x_0 shifts both functions from one point to another, while the form of the curves stays the same.

This functional behaviour captures some of the features we expect: The result can be interpreted as a travelling band with the maximum density in the transition zone between the aerobic and the anaerobic region in the system. It also makes sense to identify the functional dependence of D with the shape of the oxygen concentration c itself. If we suppose that there is an oxygen source at $x = 0$, it also makes sense that the band travels towards it, i.e. $t(x_0 = 5) > t(x_0 = 10)$. On the contrary, we

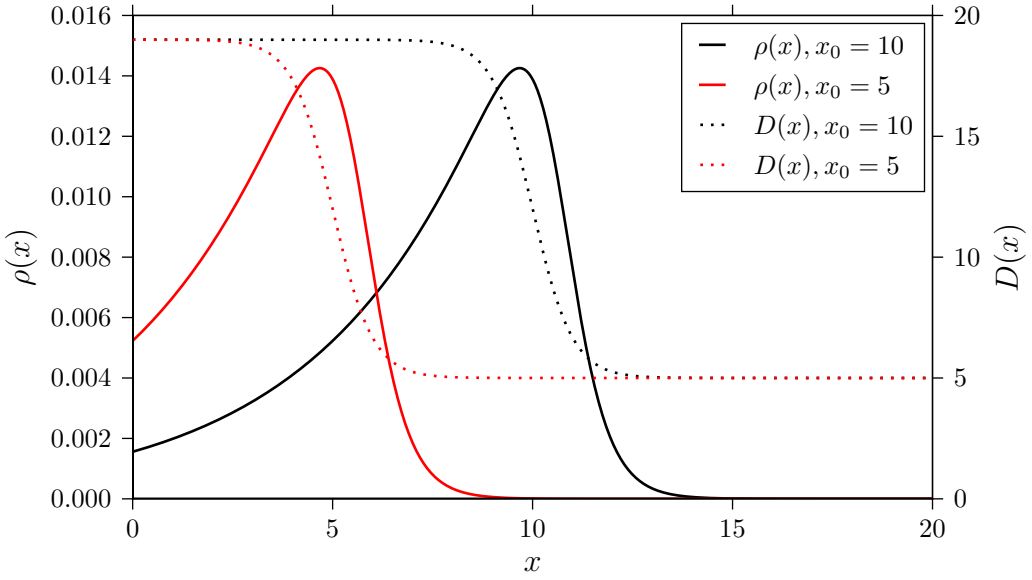

Figure 2.8.: Diffusion rate and particle density according to Eqs. (2.22) and (2.23)

would also expect that the height of the peak rises because more and more particles join the band. However, as we have not normalized ρ, the integral over it does not stay constant so we lose particles in this model. We also need to keep in mind that we consider steady-state situations that are typically not obtained in our system, which is intrinsically in a non-equilibrium state.

3. Model description

3.1. Equations of motion

In the following we describe the equations of motion that we solve for every particle i in our MD simulations and the individual contributions to them. They are based on the previously derived equations for active particles (Eqs. (2.7) and (2.8)):

$$\dot{\boldsymbol{r}}_i(t) = v_i\left(c(\boldsymbol{r}_i, t)\right)\boldsymbol{e}_i(t) + \frac{1}{\gamma_\mathrm{f}}\boldsymbol{F}_i(t), \tag{3.1}$$

$$\dot{\boldsymbol{e}}_i(t) = \boldsymbol{\eta}_{\perp,i}(t) - \lambda_i(t)\boldsymbol{e}_i(t) + \boldsymbol{g}_{\mathrm{c},\,i}(t) + \boldsymbol{g}_{\mathrm{w},\,i}(t) + \boldsymbol{g}_{\mathrm{ox},\,i}(t). \tag{3.2}$$

We can see that the change of position $\boldsymbol{r}_i$ is purely deterministic: One contribution is due to the particle's velocity v_i that can depend on the local oxygen concentration c as described in Chap. 3.2. The second contribution arises from a pairwise interparticle force $\boldsymbol{F}_i$ realized by means of a WCA potential and controlled by a parameter γ_f (see Chap. 3.3).

Changes in the orientation $\boldsymbol{e}_i$ result from multiple contributions that can be interpreted as torques: $\boldsymbol{\eta}_{\perp,i}$ is the part of a random noise vector $\boldsymbol{\eta}_i$ that is orthogonal to $\boldsymbol{e}_i$. In order to keep the orientation at unity length, we employ a Lagrangian multiplier λ_i. By demanding that the torque be orthogonal to the orientation we obtain a unique value for λ_i. By this means we no longer need to normalize the orientation in every step and can instead maintain a time-continuous version of the algorithm [38]. Further contributions arise from collisions with other particles or walls ($\boldsymbol{g}_{\mathrm{c},\,i}$ and $\boldsymbol{g}_{\mathrm{w},\,i}$, cf. Chap. 3.4) and from interactions with the oxygen field ($\boldsymbol{g}_{\mathrm{ox},\,i}$, cf. Chap. 3.5).

3.2. Speed distribution and dependence on oxygen

Every particle has a base speed $v_{0,i}$ drawn from a given distribution (see Fig. 3.1) that stays constant during one simulation. The distribution is composed of two

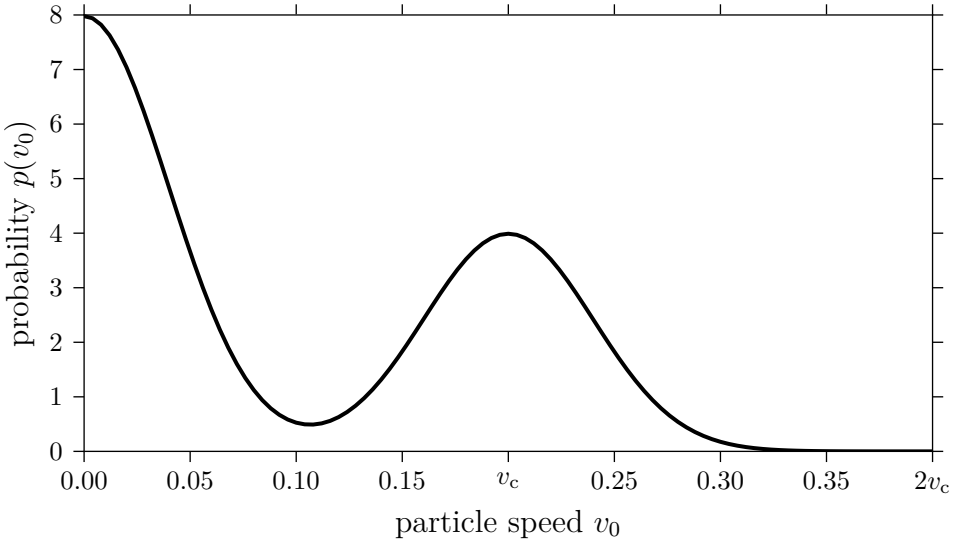

Figure 3.1.: Initial speed distribution with $v_c = 0.2$ and $\sigma_{v_c} = 0.04$

identical Gaussian distributions, one centered at zero, and the other at v_c, each with the same standard deviation σ_{v_c}:

$$p(v_0) \sim \begin{cases} \frac{1}{\sqrt{2\pi}\sigma_{v_c}} \left[2 \exp\left(\frac{-v_0^2}{2\sigma_{v_c}^2}\right) + \exp\left(\frac{-(v_0+v_c)^2}{2\sigma_{v_c}^2}\right) + \exp\left(\frac{-(v_0-v_c)^2}{2\sigma_{v_c}^2}\right) \right], & 0 \le v_0 \le 2v_c \\ 0, & \text{else} \end{cases} \tag{3.3}$$

One can see that the higher peak at $v_0 = 0$ results from the fact that an outcome smaller than zero is projected on the respective positive value. Also, to prevent unrealistically high values the distribution is truncated at $v_{\max} = 2\ v_c$. This model results from visual inspection of the motility of a colony of *S.o.* in video microscopy where some of the particles are highly motile, whereas others hardly move at all.

The only way of varying the bacterial speed is from its dependence on the oxygen concentration at the position of the particle. In every simulation we choose among three different models (see Fig. 3.2):

(i) constant: $v_i(c) = v_{0,i}$ everywhere (3.4)

(ii) two-state: $$v_i(c) = \begin{cases} v_{0,i} + v_{\text{high}}, & c > c_t \\ v_{0,i}, & c < c_t \end{cases} \tag{3.5}$$

(iii) proportional: $$v_i(c) = \begin{cases} v_{0,i} + m_{\text{ox}}(c - c_t), & c > c_t \\ v_{0,i}, & c < c_t. \end{cases} \tag{3.6}$$

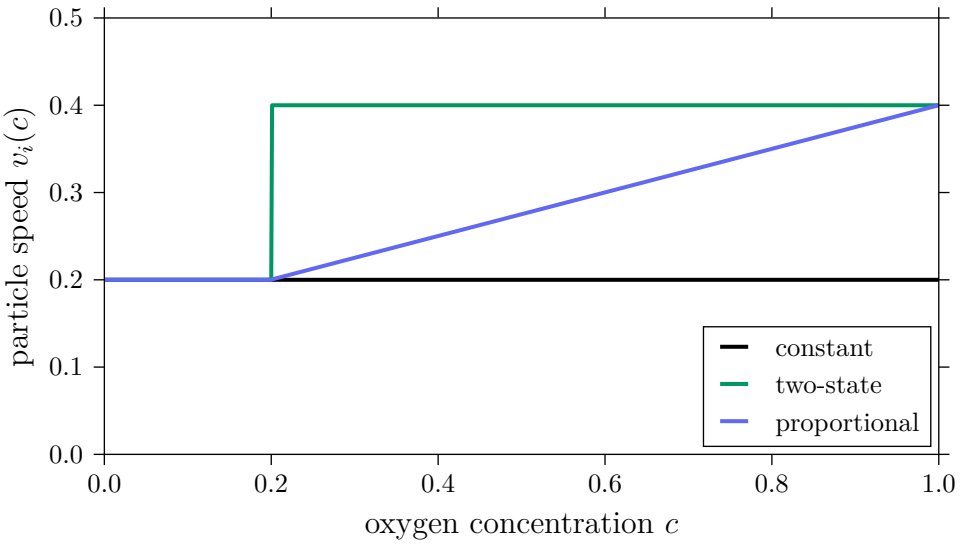

Figure 3.2.: Comparison of models for $v_i(c)$ for particles with $v_{0,i} = 0.2$, $c_\mathrm{t} = 0.2$, $v_\mathrm{high} = 0.2$ and $m_\mathrm{ox} = 0.25$

c_t is a threshold concentration, i.e. the smallest oxygen concentration the bacteria react to. Together with the other parameters v_high and m_ox, respectively, it needs to be chosen appropriately.

3.3. Interparticle force

Bacteria have rigid outer cellular membranes. Thus we can simplify our model by treating them as hard spheres. This choice neglects the fact that *S.o.* are in fact elongated, cylindrical rods (as described in Chap. 2.1), but is still a very good approximation. We choose the *Weeks-Chandler-Andersen* (*WCA*) potential [39], which is a shifted and truncated Lennard-Jones potential and thus only contains a repulsive part to model the hard sphere interaction:

$$V_\mathrm{WCA}(r) = \begin{cases} 4\epsilon\left(\frac{\sigma^{12}}{r^{12}} - \frac{\sigma^6}{r^6}\right) + \epsilon, & r \leq 2^{1/6}\sigma, \\ 0, & r > 2^{1/6}\sigma, \end{cases} \tag{3.7}$$

where $r = |\boldsymbol{r}|$ is the particle distance, σ the particle diameter and ϵ the energy scale. The potential is used to assign a volume to each particle, thus preventing them from overlapping. ϵ can be thought of as the membrane stiffness: The higher its value, the bigger is the value of the potential (see Fig. 3.3) and thus the displacement after

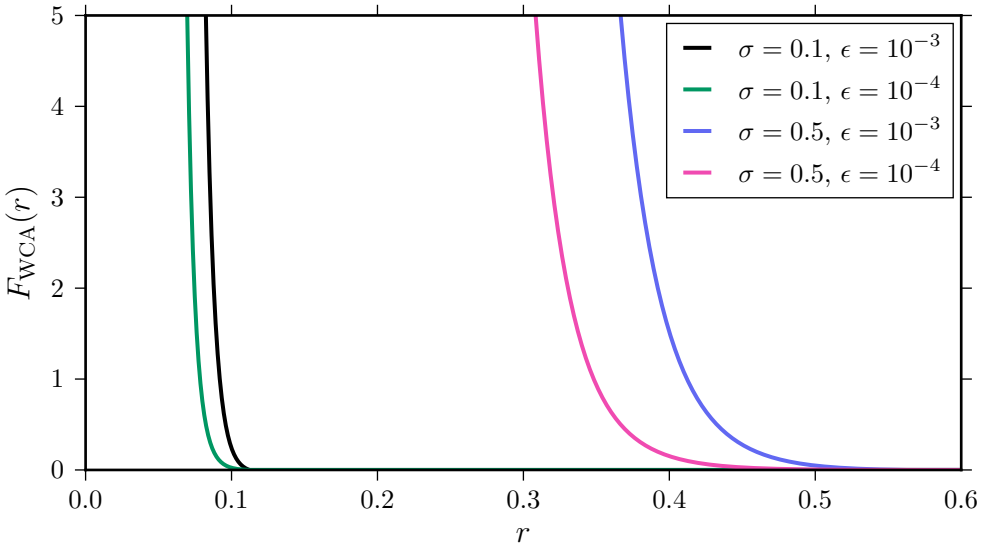

Figure 3.3.: Comparison of the WCA force for different values of σ and ϵ

a collision due to the force. The force derived from Eq. (3.7) is

$$\boldsymbol{F}_{\mathrm{WCA}}(\boldsymbol{r}) = -\boldsymbol{\nabla} V_{\mathrm{WCA}}(\boldsymbol{r}) = \begin{cases} 24\epsilon \left(2\frac{\sigma^{12}}{r^{14}} - \frac{\sigma^6}{r^8}\right)\boldsymbol{r}, & r \leq 2^{1/6}\sigma, \\ 0, & r > 2^{1/6}\sigma. \end{cases} \tag{3.8}$$

If a particle interacts with more than just one other particle, all contributions are simply added up (superposition principle). Because the parameter γ_{f} in the equations of motion (Eq. (3.1)) is redundant with ϵ for the WCA force, we set $\gamma_{\mathrm{f}} = 1$ for all simulations.

3.4. Collisions

Apart from shifting particles involved in a collision due to the WCA potential we also need to rotate their orientation afterwards. The actual collision mechanism is unknown, but we assume a billiard-like behaviour: While the component parallel to the force $\boldsymbol{F}$ is inverted, the component perpendicular to it is not changed (see also Fig. 3.4):

$$\boldsymbol{g}_{\mathrm{c}} = -2(\boldsymbol{e} \cdot \hat{\boldsymbol{F}})\hat{\boldsymbol{F}} \tag{3.9}$$

We apply this mechanism only if the scalar product of the orientation of a particle and the force vector is negative, because otherwise it leads to unphysical behaviour.

Collisions with walls (i.e. the air bubble or boundaries in z-direction) follow the

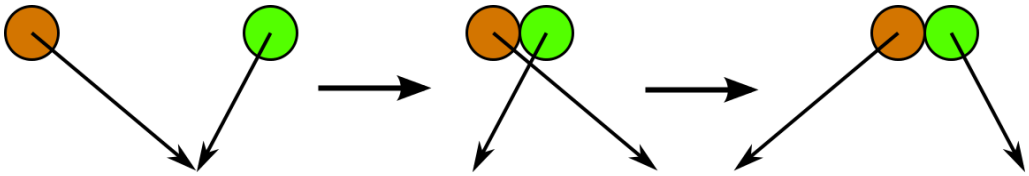

Figure 3.4.: Collision process

same mechanism, i.e. the component parallel to the plane of reflection with unit normal vector $\hat{\boldsymbol{n}}$ stays constant whereas the perpendicular component is reversed:

$$\boldsymbol{g}_{\mathrm{w}} = -2(\boldsymbol{e} \cdot \hat{\boldsymbol{n}})\hat{\boldsymbol{n}} \tag{3.10}$$

3.5. Aerotactic mechanisms

We have seen in Chap. 2.1.3 that the bacterial motility, i.e. propagation speed and frequency of orientation reversals, changes under influence of a chemoattractant. Thus velocity-jump events as described in Chap. 2.2.4 can be seen as the result of klinokinetic or -tactic behaviour. We model this feature by reversing the orientation of a particle in the x-y plane:

$$\boldsymbol{g}_{\mathrm{ox}} = -2(e_x\hat{\boldsymbol{x}} + e_y\hat{\boldsymbol{y}}), \tag{3.11}$$

where $\boldsymbol{e} = e_x\hat{\boldsymbol{x}} + e_y\hat{\boldsymbol{y}} + e_z\hat{\boldsymbol{z}}$ is the orientation of a particle. In our simulation we cannot set the turning frequency directly. Instead we vary the probability of a turning event p_{turn}, from which follows said frequency. These probabilities have to be understood as probabilities per time step, i.e. if we increase the time step length δt we also have to increase the probability. We compare three different models for the turning probability that are depicted in Fig. 3.5:

(i) "Harris rule": The higher the oxygen concentration is, the faster a particle and the bigger its turning probability [30]:

$$p_{\mathrm{turn}} = p_{\mathrm{turn}}(v) \sim v \sim c \tag{3.12}$$

(ii) "Anti-Harris rule": The lower the oxygen concentration is, the higher the turning probability:

$$p_{\mathrm{turn}} = p_{\mathrm{turn}}(c) \sim c_0 - c \tag{3.13}$$

(iii) "Mazzag rule": The turning probability is minimal at a constant value p_0 for an ideal oxygen concentration in the range $c_{\text{ideal, min}} < c < c_{\text{ideal, max}}$. For too high concentrations it is $k_1 p_0$, while for too low concentrations it is $k_2 p_0$ ($1 \leq k_1 \leq k_2$). Between these regions there are buffer zones, i.e. $c_{\text{ideal, max}} < c < c_{\text{buffer, max}}$ and $c_{\text{buffer, min}} < c < c_{\text{ideal, min}}$. The actual value of p_{turn} depends on the orientation of the particle $\boldsymbol{e}$ with respect to the local oxygen gradient [40]:

$$p_{\text{turn}}(c) = \begin{cases} p_0, & \begin{cases} c_{\text{ideal, min}} < c < c_{\text{ideal, max}} \\ c_{\text{ideal, max}} < c < c_{\text{buffer, max}} \text{ and } \boldsymbol{e} \cdot \boldsymbol{\nabla} c \leq 0 \\ c_{\text{buffer, min}} < c < c_{\text{ideal, min}} \text{ and } \boldsymbol{e} \cdot \boldsymbol{\nabla} c \geq 0 \end{cases} \\ k_1 p_0, & \begin{cases} c > c_{\text{buffer, max}} \\ c_{\text{ideal, max}} < c < c_{\text{buffer, max}} \text{ and } \boldsymbol{e} \cdot \boldsymbol{\nabla} c > 0 \end{cases} \\ k_2 p_0, & \begin{cases} c < c_{\text{buffer, min}} \\ c_{\text{buffer, min}} < c < c_{\text{ideal, min}} \text{ and } \boldsymbol{e} \cdot \boldsymbol{\nabla} c < 0 \end{cases} \end{cases} \tag{3.14}$$

In [40], the authors suggest using $k_1 = k_2 = 5$ for *Azospirillum brasilense*, a species with similar characteristics as *S.o.*

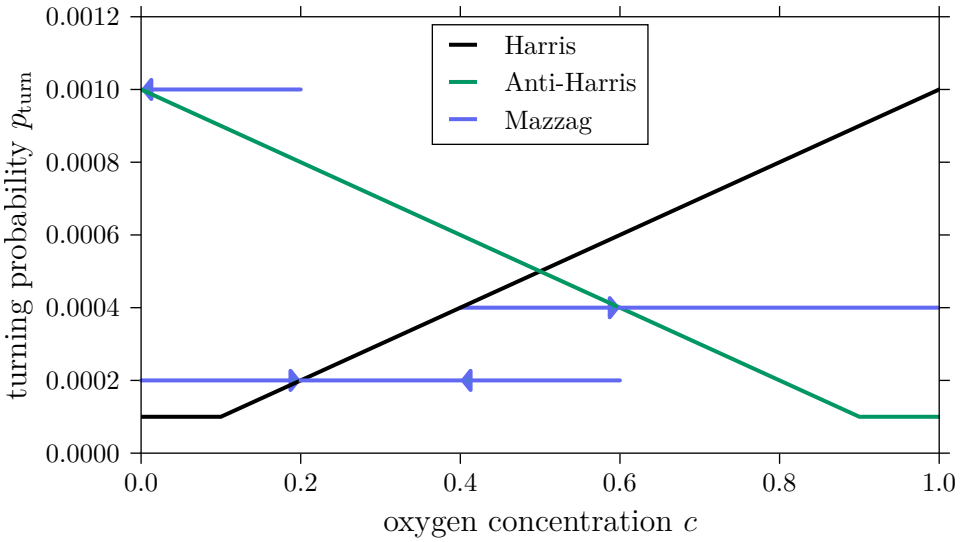

Figure 3.5.: Turning probabilities for different aerotactic mechanisms

4. Computational methods

4.1. Integration scheme

The integration scheme relies on a simple Euler forward algorithm. As the simulation takes place in an overdamped regime (see Chap. 2.1.1), there is no acceleration influencing the speed of the particles. This assumption allows us to maintain a first-order integration scheme, treating changes in position $\boldsymbol{r}_i$ and orientation $\boldsymbol{e}_i$ independently of each other. Thus, the time-discrete versions of Eq. (3.1) and (3.2) with time step δt at times $t, t+1$ read

$$\boldsymbol{r}_i^{t+1} = \boldsymbol{r}_i^t + \left(v_i^t(c)\boldsymbol{e}_i^t + \frac{1}{\gamma_\mathrm{f}} \boldsymbol{F}_i^t \right) \delta t, \tag{4.1}$$

$$\boldsymbol{e}_i^{t+1} = \boldsymbol{e}_i^t + (\boldsymbol{\eta}_{\perp,i}^t - \lambda_i^t \boldsymbol{e}_i^t)\delta t + \boldsymbol{g}_{\mathrm{c},\,i}^t + \boldsymbol{g}_{\mathrm{w},\,i}^t + \boldsymbol{g}_{\mathrm{ox},\,i}^t \,. \tag{4.2}$$

4.2. Oxygen diffusion scheme

We include an air bubble in the centre of our system that cannot be accessed by the bacteria. To account for diffusing oxygen, we employ a finite-difference diffusion scheme, i.e. we subdivide our volume into square cells along the x- and y-axis, neglecting fluctuations in the confined z-direction. The scheme is a centered space, forward time Euler algorithm with a five-point stencil and periodic boundary conditions, based on Eq. (2.12), which becomes

$$c_{i,j}^{t+1} = c_{i,j}^t + \frac{D\delta t}{\delta x^2}(c_{i-1,j}^t + c_{i+1,j}^t + c_{i,j-1}^t + c_{i,j+1}^t - 4c_{i,j}^t) - \kappa n_{i,j}^t \delta t. \tag{4.3}$$

D is the diffusion constant of dissolved oxygen in water and $n_{i,j}^t$ the number of particles with consumption rate κ in cell i, j. To account for the θ-function in Eq. (2.12) we set the minimal value of $c_{i,j}^t$ to zero. We also need to specify initial conditions for our system to define it completely. We choose a uniform distribution, which also makes sense from a physical point of view if we define $t = 0$ as the point

in time at which the experimental cell is closed:

$$c^0_{i,j} \equiv c_0 \equiv C_0/N_{\text{cells}} \; \forall \; i, j, \tag{4.4}$$

where C_0 and N_{cells} are the initial oxygen content and the number of cells in the system, respectively.

A Von-Neumann stability analysis shows that the numerical diffusion scheme (4.3) is *conditionally stable* [41], i.e. it yields a stable solution only under the condition

$$\delta t \leq \frac{\delta x^2}{4D}. \tag{4.5}$$

Cells that are located fully inside the air bubble do not follow Eq. (4.3): Because oxygen diffusion in air is six orders of magnitude faster than in water [34] we assume that it takes place immediately. Hence, we define the oxygen concentration as the average of all the cells in question. Also, we have the possibility to add a number of virtual cells $N_{\text{cells, virtual}}$ to the bubble that do not show up in the system physically but are capable of storing oxygen. In this way we can decouple the physical size of the bubble from the oxygen stored inside, setting the total initial oxygen in our system to $C_0^{\text{total}} = c_0(N_{\text{cells}} + N_{\text{cells, virtual}})$.

4.3. Choice of time step δt

The introduction of the WCA potential sets an upper bound for the time step δt: If we choose the latter too big, two particles that do not sense each other in step t, i.e. their distance r^t is $\geq 2^{1/6}\sigma$, can significantly overlap in step $t+1$ if things go bad. Such overlaps create immense, unphysical forces that can lead to a cascade of particle jumps through (and out of) the simulation box. Therefore, we demand that the minimal distance of two particles should be σ even in a worst-case scenario:

$$\sigma \leq r^{t+1} = r^t - 2 \cdot (v_{\max} + F_{\max})\delta t \tag{4.6}$$

$$= 2^{1/6}\sigma - 2 \cdot (2\, v_{\text{c}} + F(\sigma))\delta t \tag{4.7}$$

$$\Rightarrow \delta t \lesssim 10^{-2} \tag{4.8}$$

The last result arises from inserting the values we typically use in our simulations ($\sigma = 0.1, v_{\text{c}} = 0.2, \epsilon = 10^{-4}$). With this choice we can avoid unphysical forces at least for the situation described here, i.e. two particles initially not sensing each

other, with maximum speed towards each other, each pushed by the maximum force additionally. Still it does not cover *all* possible situations, e.g. in a multi-particle collision or due to external forces. As such cases only happen very rarely we settle for the condition derived, but additionally check for too big forces in the code.

4.4. Choice of units

As far as units are concerned, we need to distinguish between three different choices:

- real physical units as from the experiment,
- reduced MD units used in the simulation and
- coordinates in the unit box.

Assuming all particles are of same mass, we are only dealing with two different dimensions dictating the particles' dynamics (time and space). Hence, we need to employ two independent quantities from the experiment to adapt the simulation to it. If we choose

- particle diameter $\sigma = 1.0\,\mu\text{m}$ ($\equiv 0.1$ distance unit),
- diffusion constant $D = 2.0 \times 10^3\,\mu\text{m}^2\,\text{s}^{-1}$ ($\equiv 1$ diffusion unit) of dissolved oxygen in water,

one time unit is equal to $5 \times 10^{-2}\,\text{s}$. Thus, we are able to set all other physical quantities, such as turning frequencies or filling fractions, in accordance with the experimental scale, too. In contrast to that, for the potential parameter ϵ and the bacterial consumption rate κ we use values obtained empirically from our simulations. This is due to the fact that the former is an empirical model with unknown parameters, whereas the latter is only very difficult to access in an experiment. Reduced or MD units are typically used to avoid the occurrence of very large or small numbers during calculations that lead to loss of precision. Apart from that, it simplifies the equations of motion to relevant quantities and allows for the comparison of arbitrary simulations. In order to save computation time, the simulation volume is scaled to a unit box. This means that the particles' coordinates are scaled to the range $(-0.5, 0.5] \times (-0.5, 0.5] \times (-0.5, 0.5]$ instead of $[0, L_x) \times [0, L_y) \times [0, L_z)$. This feature simplifies especially the calculations effected by the periodic boundary conditions. Only when calculating the WCA potential real distances need to be employed to obtain consistent results.

4.5. Simulation parameters

The simulation takes place in a flat, rectangular box, very similar to a system of bacteria confined to the volume in a specimen holder (see Fig. 1.1). Therefore, we call our system a quasi-2d system, with periodic boundary conditions in the x-y plane and reflective walls in z-direction. The air bubble is modelled as a cylinder in the centre stretching the whole z-direction with constant size. In Table 4.1 the important simulation parameters are summarized as well as their typical quantities and values in terms of MD units, respectively.

Type	Description	Name	Typical size
numerical	number of simulation steps	N_{steps}	$10^5 - 10^7$
	length of time step	δt	10^{-2}
	cell size during oxygen diffusion	δx	1
constant	container height	L_z	1
	particle size	σ	0.1
	number of particles	N_{part}	10^4
	potential steepness	ϵ	10^{-4}
	force parameter	γ_{f}	1
	oxygen diffusion constant	D	1
	centre of speed distribution	v_{c}	0.2
	width of speed distribution	$\sigma_{v_{\text{c}}}$	0.04
	initial oxygen per cell	c_0	1
variable	filling fraction	ϕ	$10^{-2} - 10^{-4}$
	system size	L_x, L_y	$25 - 250$
	size of air bubble	r_{bubble}	$0.1\, L_x$
	noise strength	η	$0.1 - 5$
	bacterial oxygen consumption	κ	$10^{-3} - 10^{-4}$
	number of cells	N_{cells}	$L_x L_y/(\delta x)^2$
	number of virtual cells	$N_{\text{cells, virtual}}$	$0 - 10^4$
	total initial oxygen content	C_0^{total}	$10^4 - 10^5$
model	turning mechanisms		Harris, Anti-Harris, Mazzag
	turning probability	p_{turn}	$0 - 10^{-2}$
	velocity dependence on oxygen		none, proportional, two-state

Table 4.1.: Parameters used during simulations

5. Analysis

In the following we present the results of our simulations. We do not describe the results of every parameter combination, but instead figure out which parameters are crucial for our model and which are rather optional.

First we want to clarify our naming and plotting conventions: We denote the position of a particle with $\boldsymbol{r}$, measured from the centre of the system. $r = |\boldsymbol{r}|$ is then the distance to the centre and $\hat{\boldsymbol{r}} = \boldsymbol{r}/r$ a unit vector pointing in direction of $\boldsymbol{r}$. With Δr we denote a displacement. Finally, $\boldsymbol{e}$ is the orientation of a particle and $\boldsymbol{v} = v\boldsymbol{e}$ its velocity. When referring to an absolute time t or an interval Δt, we use the reduced time unit as derived in Chap. 4.4.

There are several possibilities to analyse the results: Typically we use space-time plots to show both the spatial and the temporal evolution of a quantity, e.g. of the average filling fraction $\langle\phi\rangle$. The angular brackets denote both an average over 360°, i.e. all particles at a distance r from the center axis, and over an ensemble of independent simulations with the same parameters. In the same manner, we plot the evolution of the average particle speed $\langle v\rangle$ and oxygen concentration $\langle c\rangle$. Another means of visualization of our system is to plot a top view of the particles, where we typically restrain limit the number of particles to 2000 to allow a clear picture. Here, quiver plots enable us to present both particle distributions as well as their speeds and orientations.

To analyse the structure of our system in more detail, we calculate various functions: The radial distribution function $g(\Delta r)$, defined via the relation

$$g(\Delta r) \equiv \left\langle \frac{1}{\rho N_{\text{part}}} \sum_{i=1}^{N_{\text{part}}} \sum_{j=1, j\neq i}^{N_{\text{part}}} \delta(\Delta r - |\boldsymbol{r}_i - \boldsymbol{r}_j|) \right\rangle, \tag{5.1}$$

tells us how many other particles one particle on average finds in a distance Δr. ρ and N_{part} are the global particle density and number of particles, respectively, and $\delta(r)$ is Dirac's delta function. The angular brackets denote an ensemble average.

We also study a number of autocorrelation functions

$$C(f(x), \Delta x) = \frac{\langle f(x) f(x + \Delta x) \rangle}{\langle f(x) \rangle \langle f(x + \Delta x) \rangle}, \tag{5.2}$$

where x is an independent variable. Here we focus on the particle orientation $\boldsymbol{e}$ as a function of either distance from the centre of the system r or time t. To simplify our notation, we define the functions

$$C_1^{ee}(r, \Delta r) \equiv \langle \boldsymbol{e}(r) \cdot \boldsymbol{e}(r + \Delta r) \rangle \,, \tag{5.3}$$

$$C_2^{ee}(r, \Delta r) \equiv \left\langle (\boldsymbol{e}(r) \cdot \boldsymbol{e}(r + \Delta r))^2 \right\rangle, \tag{5.4}$$

and

$$C_1^{ee}(t, \Delta t) \equiv \langle \boldsymbol{e}(t) \cdot \boldsymbol{e}(t + \Delta t) \rangle \,, \tag{5.5}$$

$$C_2^{ee}(t, \Delta t) \equiv \left\langle (\boldsymbol{e}(t) \cdot \boldsymbol{e}(t + \Delta t))^2 \right\rangle, \tag{5.6}$$

respectively. We note that we only consider x- and y-components of the orientation because the relevant dynamics take place only in this plane. The former two functions can tell us how particles are oriented with respect to each other, whereas from the latter we infer how rigidly a particle keeps its direction.

Another useful quantity to describe positional order in the system is the scalar product of particle position (with respect to the centre of the system) and its orientation,

$$C_1^{re}(r, t) \equiv \langle \hat{\boldsymbol{r}}(r, t) \cdot \boldsymbol{e}(r, t) \rangle \tag{5.7}$$

and

$$C_2^{re}(r, t) \equiv \left\langle (\hat{\boldsymbol{r}}(r, t) \cdot \boldsymbol{e}(r, t))^2 \right\rangle, \tag{5.8}$$

respectively. These functions are no autocorrelation functions, but we can still use them to describe the structure of our system: If a majority of the particles moves towards the centre, C_1^{re} will show a negative amplitude. C_2^{re} will also show an amplitude, even though it is weaker because of the square, but from this quantity we can mainly infer if there are many particles moving perpendicular to the centre of the system.

5.1. Regular system

5.1.1. Parameter choice

In the following we consider a system of swimmers with the parameters given in Table 5.1. The plots that do not show single particles are calculated based on an average of 100 simulations with the same parameter choice, but different initial random seeds. We want to stress here that we have set $k_1 = 1$, meaning that oxygen only acts as an attractant in the system and never as a repellent. Therefore, particles only want to escape regions with a too low oxygen concentration, but are not affected by too high concentrations, e.g. next to the bubble.

5.1.2. Density and speed

Figure 5.1 shows space-time plots of the average local filling fraction $\langle\phi\rangle$, speed $\langle v\rangle$ and oxygen concentration $\langle c\rangle$. The grey regions in Fig. 5.1(a) and (b) indicate the space occupied by the cylinder that is not accessible to the particles and the dashed, vertical line marks its boundary.

Filling fraction and speed remain homogeneous up to $t \approx 5000$. At this time, the oxygen concentration has decayed in the whole system and a gradient has formed towards the bubble. A short calculation shows why this must be the case: The initial oxygen content in the system is $C_0 = 62500$ (not considering the additional cells in the centre). The total oxygen consumption is $C_{\text{consumed}} = \kappa N_{\text{part}} t = 61250$ for $t =$

Parameter	Value
number of particles	$N_{\text{part}} = 12250$
system size	$L_x = L_y = 2500\,\sigma, L_z = 10\,\sigma$
filling fraction	$\phi_0 \approx 1.06 \times 10^{-4}$
noise	$\eta = 5$
speed dependence	none ($v(c) = v_0$)
initial oxygen concentration	$c_0 = 1$
additional cells inside bubble	$N_{\text{cells, virtual}} = 10^4$
total initial oxygen content	72500
consumption rate	$\kappa = 10^{-3}$
aerotactic mechanism	Mazzag
turning probabilities	$p_{\text{turn}} = 0.00125$, $k_1 = 1$, $k_2 = 5$
oxygen concentration thresholds	$c_{\text{ideal, min}} = 0.1$, $c_{\text{buffer, min}} = 0.05$

Table 5.1.: Parameters used for the simulations in Chap. 5.1.1

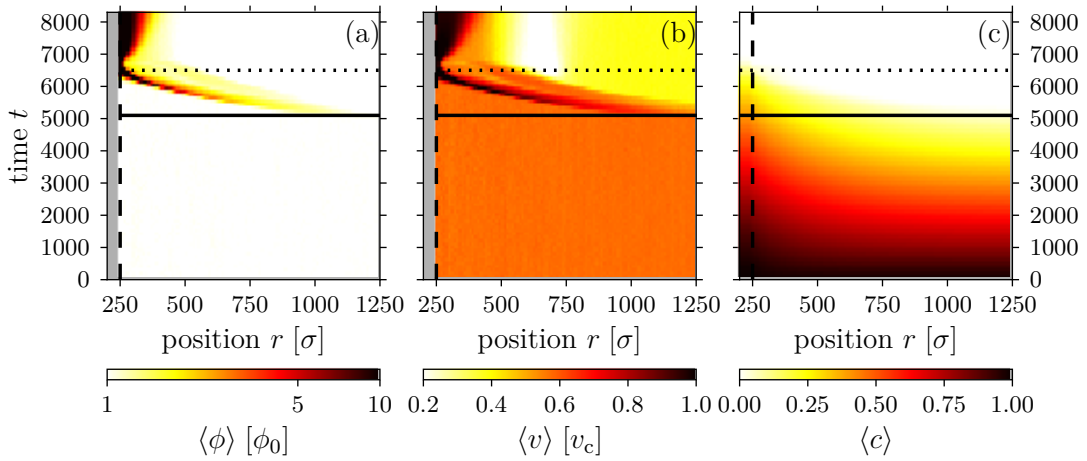

Figure 5.1.: Space-time plots of mean local filling fraction $\langle\phi\rangle$, mean speed $\langle v\rangle$ and mean oxygen concentration $\langle c\rangle$

5000, so the average concentration per cell is now $\langle c\rangle = (C_0 - C_{\text{consumed}})/N_{\text{cells}} = 0.02$. This result does not yet consider the contribution from additional oxygen diffusing out of the bubble, which is naturally higher for cells closer to the center. However, the value is of the same order of magnitude as the concentration thresholds $c_{\text{ideal, min}} = 0.1$ and $c_{\text{buffer, min}} = 0.05$ determining particle reversals.

At $t \geq 5100$ (solid, horizontal line), the filling fraction at a distance of $r/\sigma \approx 1100 \pm 100$ is already slightly higher than the average, as is confirmed in Fig. 5.2. This region of higher density moves towards the centre of the system, further increasing in density, until its densest part with $\langle\phi\rangle \approx 50\,\phi_0$ reaches the bubble at $t \approx 6500$ (dotted line in Fig. 5.1(a)). This happens only after some of the faster particles

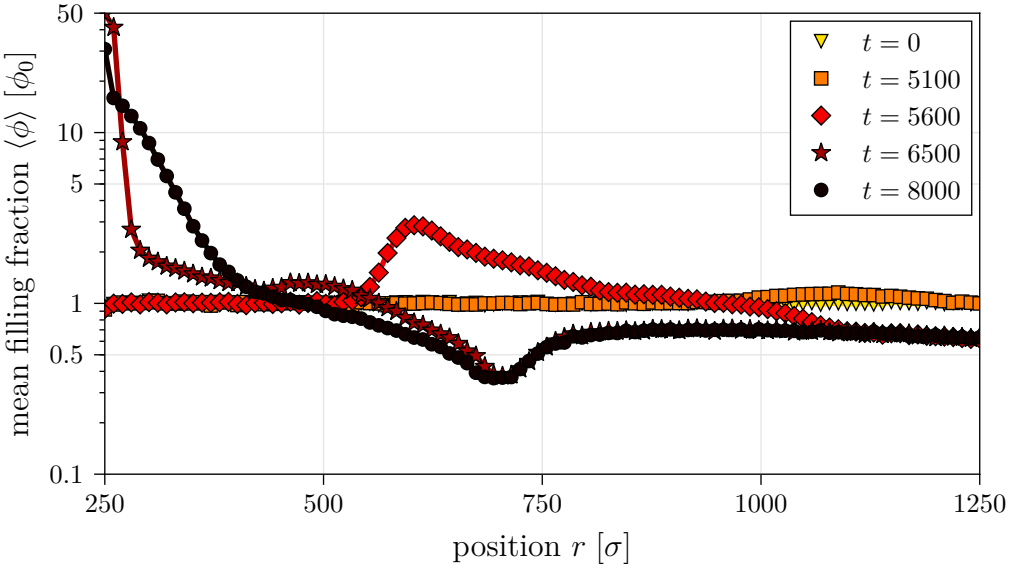

Figure 5.2.: Filling fraction profiles

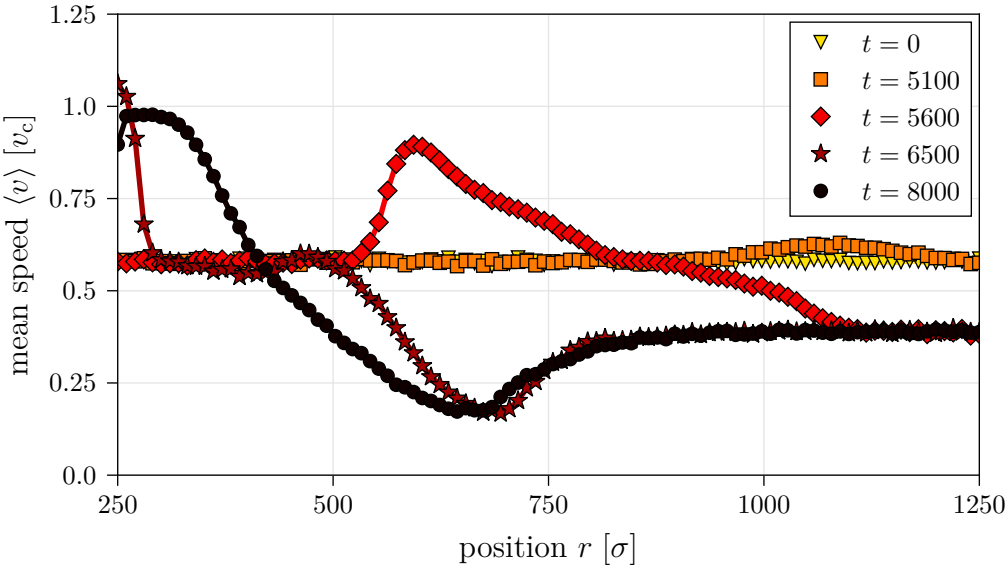

Figure 5.3.: Speed profiles

already did so, starting with $t \approx 6300$. Figure 5.2 also shows us that the average particle density behind the band falls to values below average because fast particles have left this area. The additional minimum at $650 \lesssim r/\sigma \lesssim 750$ is probably due to the fact that from this region also the slightly slower particles have been able to follow the band, leaving only particles with $v \approx 0$. For $t \gtrsim 6800$, the maximum density decreases again and the particles spread in a larger area around the bubble. This is due to the oxygen concentration that is now everywhere below the necessary level for aerobic behaviour so the particles diffuse freely again, with a higher reversal rate than in the beginning of the simulation, though.

The overall average speed for our velocity distribution $p(v)$ from Eq. (3.3) with $v_c = 0.2$ and $\sigma_{v_c} = 0.04$ is $\bar{v} = \int vp(v)\mathrm{d}v \approx 0.115 = 0.575\ v_c$. When we compare this value to Figs. 5.1(b) and 5.3, respectively, we find that the band consists largely of particles faster than that. In contrast to that, the speed in the dilute region behind the band is much below average. This is especially the case for $550 \lesssim r/\sigma \lesssim 750$, coinciding with the low-density region visible in Fig. 5.2. For large t the speed close to the bubble is still higher than average, but some of the fast particles have already diffused into more distant regions of the system, as described above.

We show additionally the oxygen profiles at the specific points in time in Fig. A.1. One can see that the homogeneous initial distribution changes into an approximately exponential decay for $5100 \leq t \leq 6500$, while the region where $\langle c \rangle = 0$ approaches the centre.

5.1.3. Positional and orientational ordering

Figures 5.4(a) and 5.5 show the temporal evolution of the radial distribution function $g(\Delta r)$. To remove confinement effects due to walls in z-direction, we normalize the results with the initial radial distribution function at $t = 0$. By this means we do not neglect the excluded volume of the bubble, though, which is especially important if there are many particles next to it, i.e. for $t \gtrsim 6500$. In this case, the "true" value of $g(\Delta r)$ is higher than the one we present. For $t \lesssim 6000$ the system is completely homogeneous with $g(\Delta r) \approx 1$, while for $t > 6000$ we can see that the particle density inside the band is much higher than in the bulk. However, these plots tell

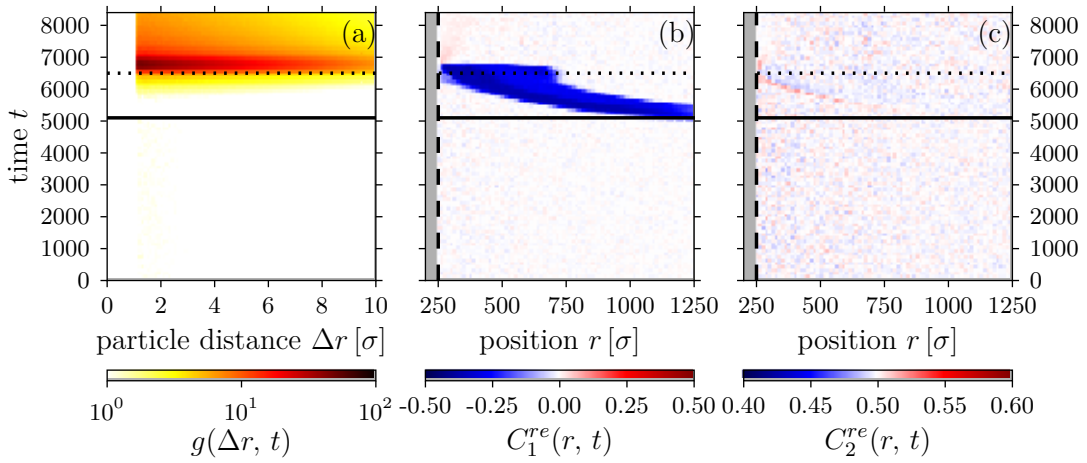

Figure 5.4.: Space-time plots of radial distribution function $g(\Delta r, t)$ and position-orientation scalar products $C^{re}_{1/2}(r, t)$

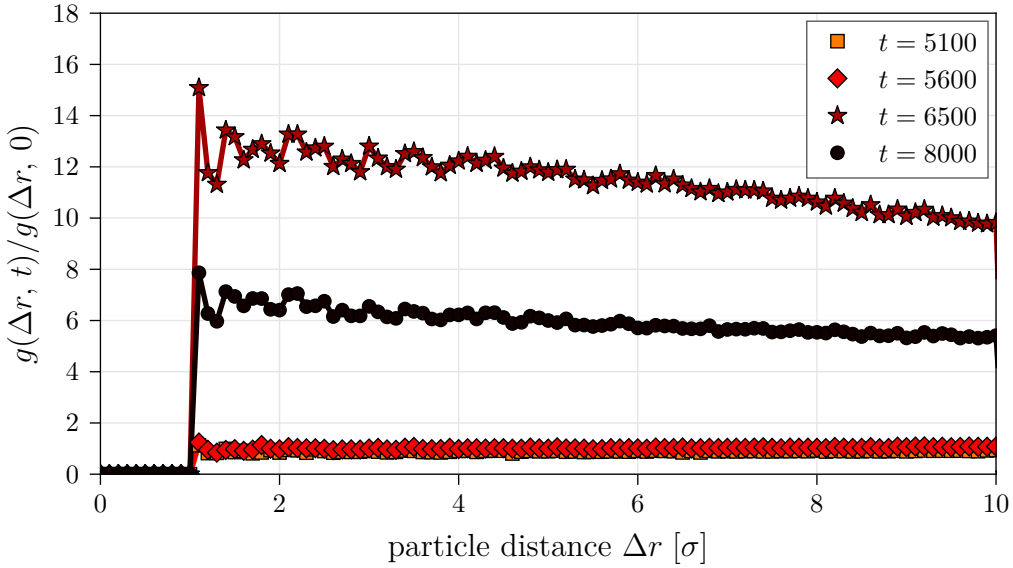

Figure 5.5.: Normalized radial distribution function $g(\Delta r, t)$

us that there is no fine structure inside the band because the only peak of $g(\Delta r)$ is at $\Delta r/\sigma \approx 1.5$.

$C_1^{re}(r,t)$ provides more information about the average particle orientation. For $t < 5000$, $C_1^{re}(r,t) \approx 0$, which indicates that initially the particles have no preferred direction of motion, i.e. they diffuse freely through the system. In contrast to that, inside the band this quantity is negative. This is due to the fact that it is negative for particles swimming towards the origin of the system (equal to the centre of the cylinder), which is just the case for a propagating band. Comparing this to Fig. 5.1(a), we can see that the lower boundary of this curve in r-t space indeed coincides with the region of maximum density. Figure 5.6 shows this comparison again: While there is no amplitude for $t = 0$ and $t = 6800$, $C_1^{re} \neq 0$ for the other times, so the particles show directed motion towards the centre.

$C_2^{re}(r,t)$ in Fig. 5.4(c) does not show any notable feature. At first sight this seems to be contrary to the amplitude that the non-squared average scalar product shows. This apparent contradiction can be solved considering the fact that the square of quantity with an absolute smaller than 1 is even smaller, and is finally averaged out because the average is taken over many particles. However, we present this plot here to compare it to the same function for a system with lower noise (see Chap. 5.2).

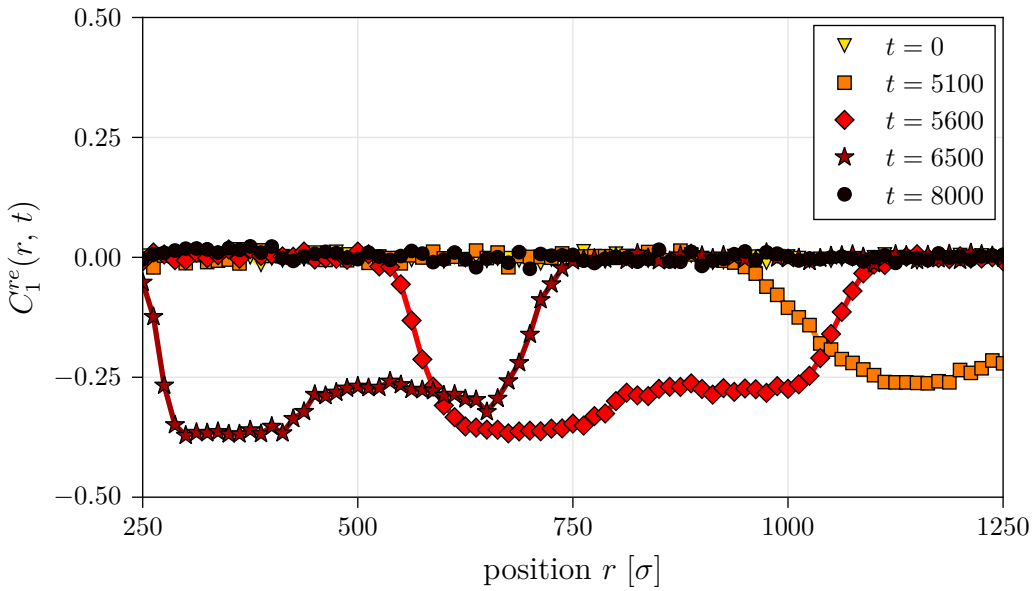

Figure 5.6.: Profiles of position-orientation scalar product $C_1^{re}(r,t)$

5.1.4. Correlation functions

In Fig. 5.7 we present the spatial orientation correlation functions $C_1^{ee}(r, \Delta r)$ and $C_2^{ee}(r, \Delta r)$ for specific times. The bin widths are $5.7\,\sigma$ for r and $0.5\,\sigma$ for Δr. We also show the average filling fraction $\langle\phi\rangle$ as a color plot, i.e. single bars from Fig. 5.1 and graphs from Fig. 5.2, respectively. One should have in mind this quantity when considering where the amplitudes in the correlation plots result from: Because the number of particles itself does not go into the correlation functions, a value that results from considering a region with high density might need to be interpreted

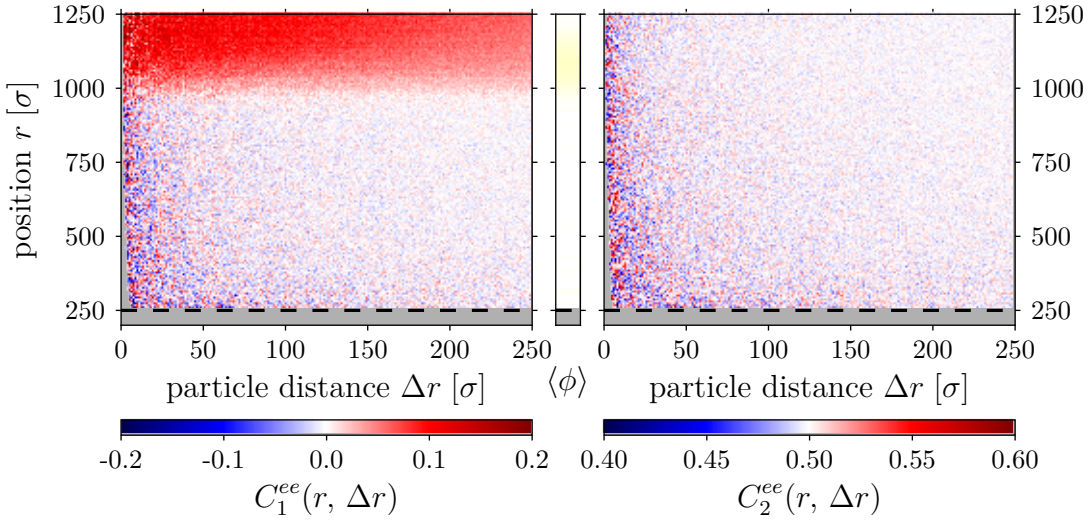

(a) $t = 5100$: early band situation

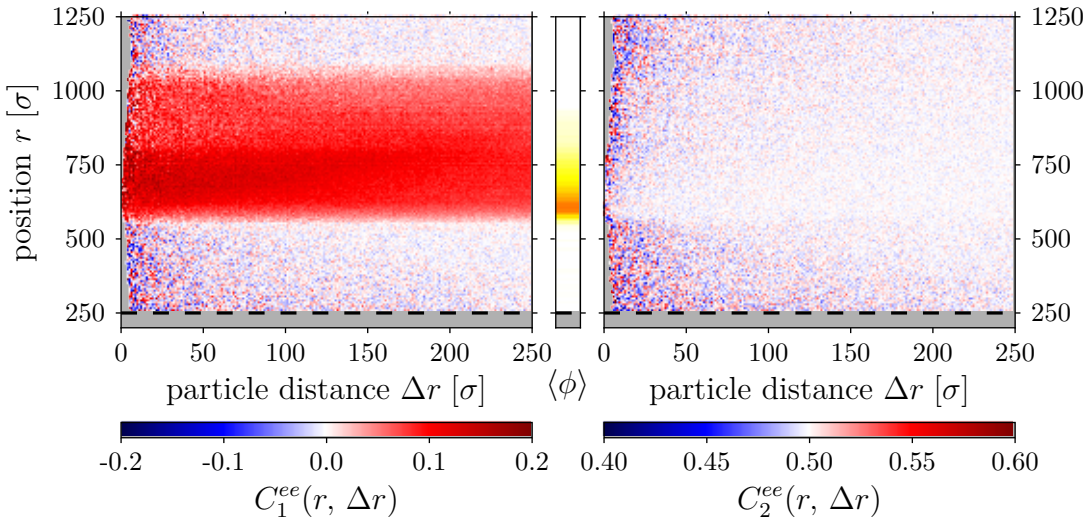

(b) $t = 5600$: intermediate band situation

Figure 5.7.: Spatial orientation correlation functions for different times t

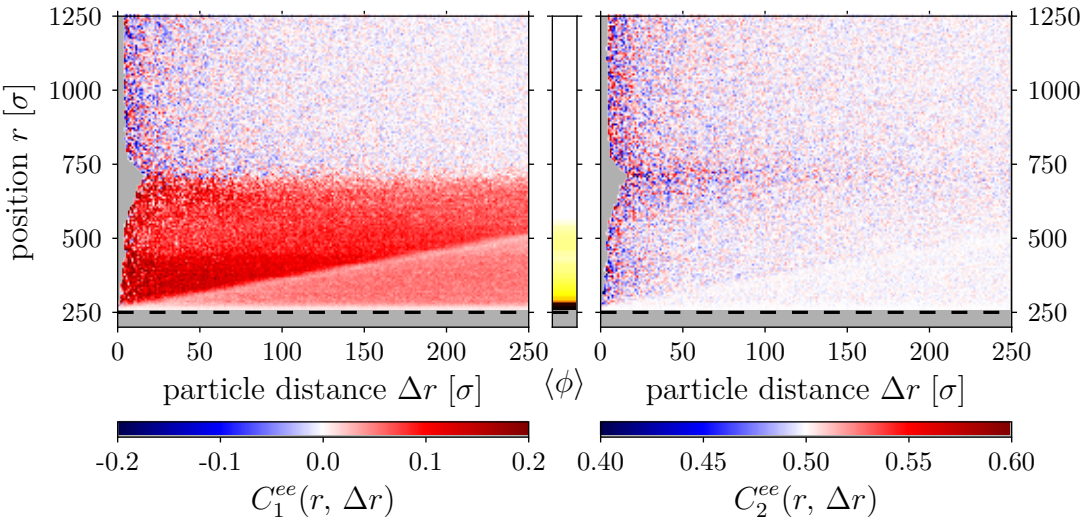

(c) $t = 6500$: band reaches bubble

Figure 5.7.: Spatial orientation correlation functions for different times t

differently than a value in a low-density area. Therefore, it is useful to have a look at the example quiver plots in Fig. 5.10. The grey regions in the plots indicate that there is no data for the point in question.

We begin with $t = 5100$, which shows a situation shortly after the first stage of the band has appeared (Fig. 5.7(a)). C_1^{ee} is distinctively different from zero only for $1000 \lesssim r/\sigma \lesssim 1250$, which also makes sense looking at the quiver plot in Fig. 5.10(a): For smaller r, all particles are still in an aerobic environment, i.e. they diffuse freely. Also it makes sense to have in mind C_1^{re} (green curve in Fig. 5.6), which indicates directed movement to the centre for this region. The same is valid for $t = 5600$, displayed in Fig. 5.10(b): We find positive correlations confined to the region $600 \lesssim r/\sigma \lesssim 1050$, again coinciding with the corresponding curve in Fig. 5.6.

In Fig. 5.7(c) ($t = 6500$) the band reaches the bubble. From the observation that $C_1^{ee}(r/\sigma = 250, \Delta r) \approx 0$ we can conclude that the very first front of the band is unordered because particles therein often collide with each other and with the bubble, and are therefore not correlated to any other part of the system. This also explains the bright line with slope $\Delta r/r = 1$ (i.e. $C_1^{ee} \approx 0$) in the red region because particle orientations at these distances are uncorrelated to the orientations in the band then, too.

The second correlation function C_2^{ee} never shows any notable feature. This is surprising at first sight, but is again due to the fact that the particles are generally aligned towards the bubble. While C_1^{ee} is able to detect this tendency, this is not

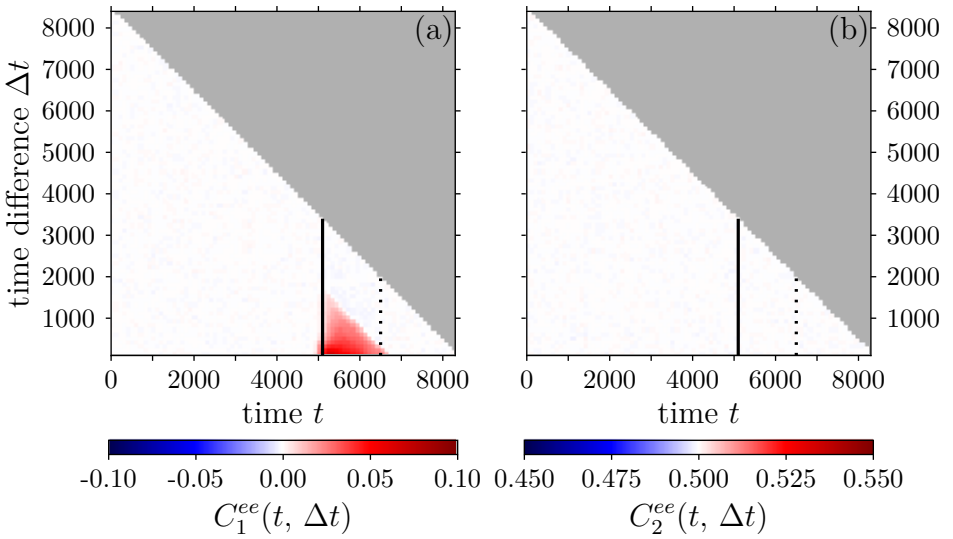

Figure 5.8.: Temporal orientation correlation functions

the case for C_2^{ee} because it does not play a role here if particles move parallel or antiparallel.

The temporal orientation correlation function $C_1^{ee}(t, \Delta t)$ in Fig. 5.8(a) does not show any feature until $t = 5000$, meaning that particles often change their orientation. Only from then up to $t = 6800$ we can see a small signal. This results from the persistence of the orientation of the band particles, that now steadily approach the bubble. Therefore it is in good agreement with C_1^{re} in Fig. 5.6. In contrast to that, C_2^{ee} again does not show any feature because the thermal noise makes particles change their orientation frequently.

5.1.5. Typical trajectories and quiver plots

In Fig. 5.9 we present typical particle trajectories for the system discussed. Trajectories 2, 4 and 6 stem from particles performing aerotaxis, approximately starting with the black marker at $t = 5100$, and are therefore most probably part of the aerotactic band. Additionally, trajectory 4 is an example of a particle that eventually diffuses back into a region farther away, thus making the band expand again into a wider region after it comes in contact with the bubble (see Fig. 5.1 for $t \gtrsim 7000$). Particle 1 is much slower, but also shows directed movement towards the bubble. In contrast to that, 3 and 5 only diffuse around their initial positions. Particle 7 also moves but does not exhibit aerotactic behaviour. In general we can see that the trajectories are warped initially, comparable to freely diffusing molecules, while they are almost straight and pointing towards the bubble during the aerotactic phase.

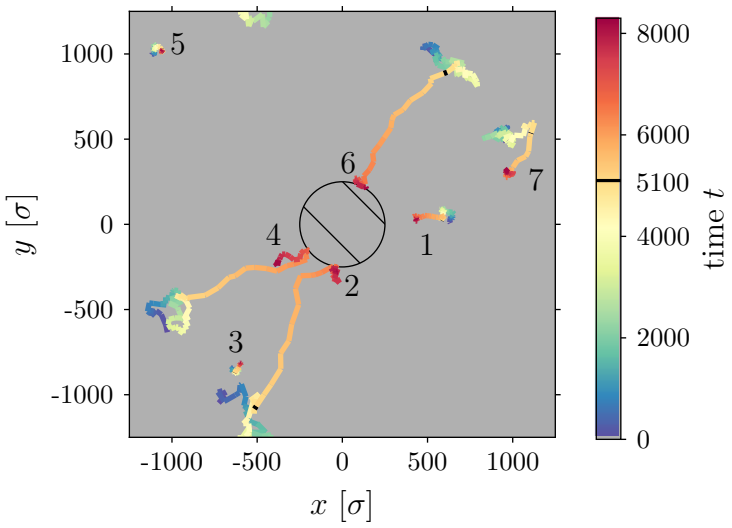

Figure 5.9.: Typical particle trajectories

The plots in Fig. 5.10 show positions and velocities of the same 1000 randomly picked particles (left) and the oxygen concentration in the system (right) at the four times considered before. The additional lines in the plots mark oxygen concentration isolines of the system (dotted: $c = 0.1$, dash-dotted: $c = 0.05$, solid: $c = 0.01$). In these pictures one can again see that there are many particles with velocity close to zero (blue dots or arrows). If an arrow is red, but apparently only very short it means that this particle primarily moves in z-direction which we neglect otherwise.

Figure 5.10(a) shows the initial stage of the band at $t = 5100$: Although the system

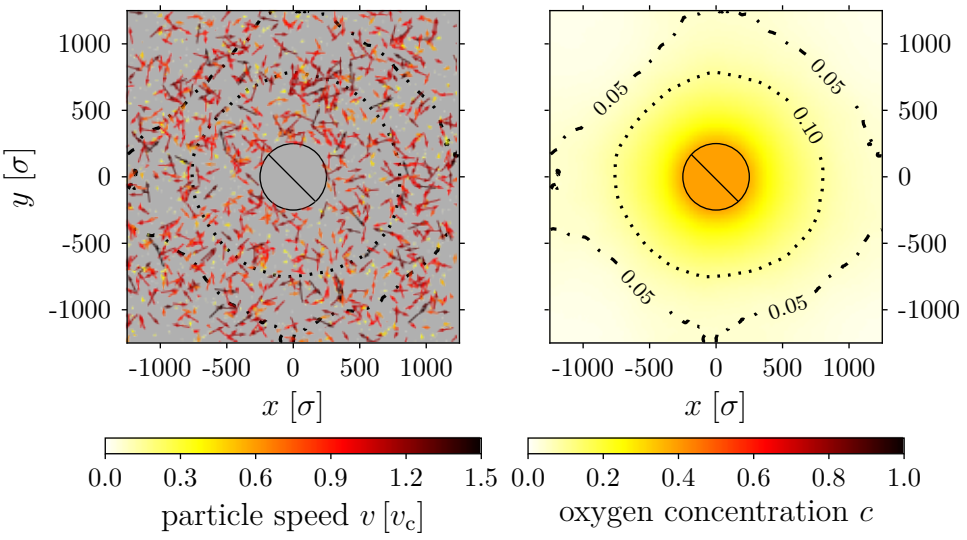

(a) $t = 5100$: early band situation

Figure 5.10.: Particle configurations for different times t

has a cylindrical symmetry, the periodic boundary conditions deform the shape of the isoconcentration lines. We notice that the particle density in the top left and right corners has already visibly decreased. In contrast to that, close to the bubble no density anomaly can be made out. Asymmetries in x- and y-direction result from slightly inhomogeneous particle distributions at the boundary at the time the band forms, and from the fact that we use square boxes in our diffusion scheme, which leads to inaccuracies around the bubble. At $t = 5600$ (see Fig. 5.10(b)), the oxygen isolines are almost circular. A dense region has formed, approximately between the

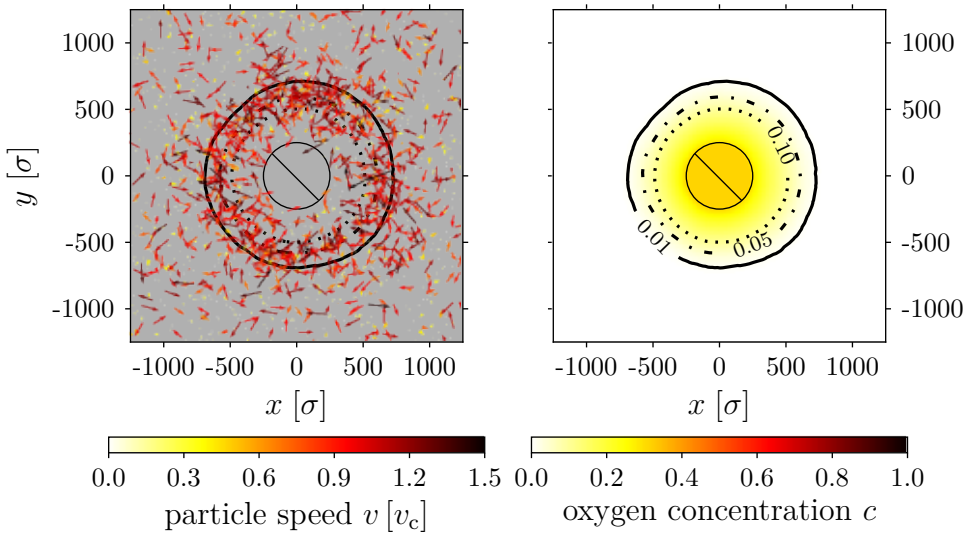

(b) $t = 5600$: intermediate band situation

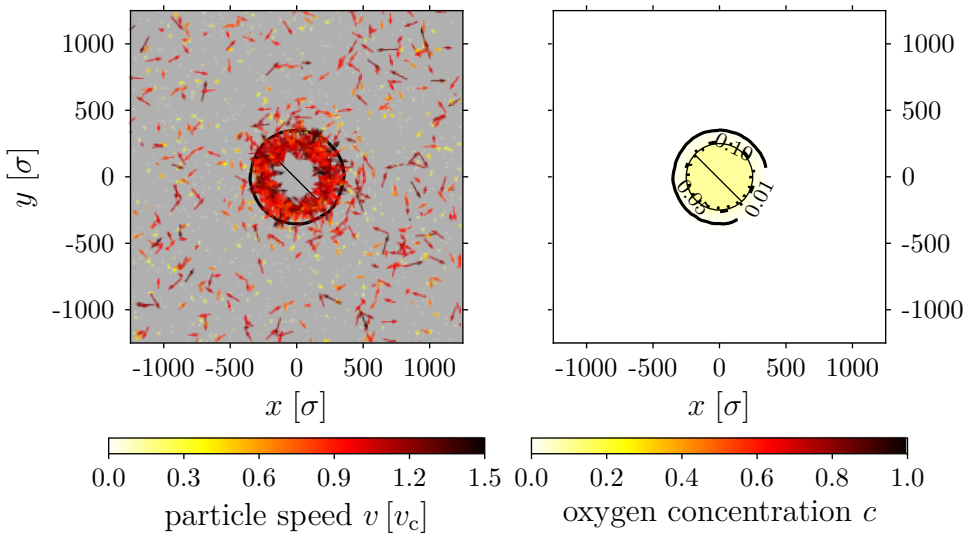

(c) $t = 6500$: band reaches bubble

Figure 5.10.: Particle configurations for different times t

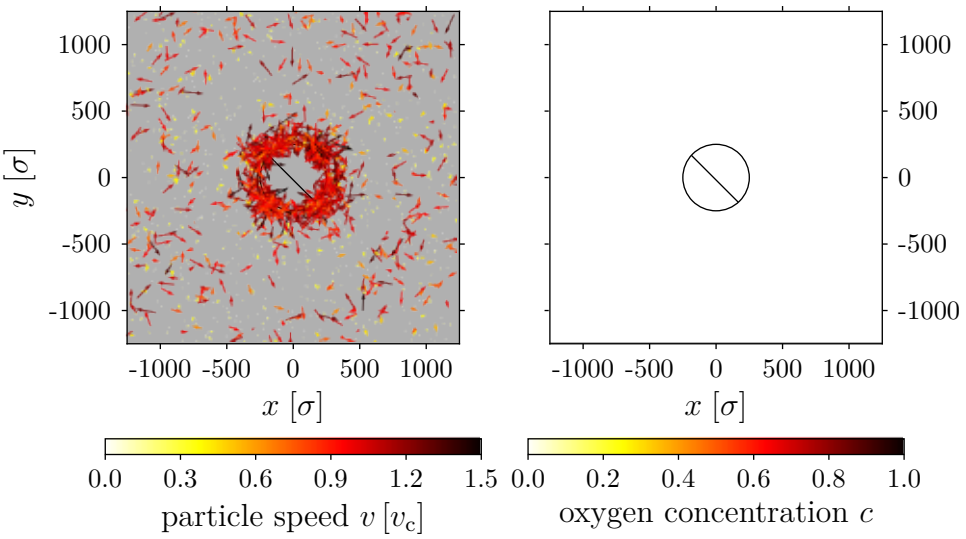

(d) $t = 8000$: situation after all oxygen has been consumed

Figure 5.10.: Particle configurations for different times t

isolines for $c = 0.1$ (dotted) and $c = 0.01$ (solid). Figure 5.10(c) shows the situation at $t = 6500$ when the band has reached the bubble and thus has reached maximum density (see Fig. 5.1). At $t = 8000$ (see Fig. 5.10(d)), almost all oxygen in the system has been consumed and some particles have already diffused back into the system.

5.1.6. Statistics of the band

In order to provide any statistics of the band, such as its width, distance from the bubble and propagation speed, we first need to give a mathematical definition of what we mean by "band". We propose the following points:

- We use a particle-based ansatz, i.e. we decide individually for each particle if it is part of the band or not. This has the advantage that we can take into account asymmetries in the band (which would not be the case if we used an ansatz based on e.g. the average particle density in some distance to the centre of the system).

- A particle belonging to the aerotactic band has to have at least a certain number of neighbours in a certain distance around it, well above the average number of neighbours. We choose twice the overall particle density in a cylinder with a radius of $30\,\sigma$ around a particle, which corresponds to 12 neighbouring particles in that volume.

In Fig. 5.11 we display the number of particles N_{band} in the band (red curve), averaged over 100 runs, and their weighted average distance to the surface of the bubble r_{band} (blue curve). We can use the standard deviation $\sigma_{r_{\text{band}}}$ as a measure of the width of the band, i.e. $d_{\text{band}} = 2\,\sigma_{r_{\text{band}}}$.

We can see that already in the beginning we obtain values for both N_{band} and r_{band}, which is unexpected. These are due to random fluctuations in the particle density, i.e. there are always some regions in the system where the particle density is twice the global value (see also Fig. 5.12(a)). However, this is no band situation, as becomes especially clear when one considers the fact that $N_{\text{band}} \approx 70$, i.e. a very low value. Only for $t \geq 4800$ we can see that r_{band} begins to decline from around $1000\,\sigma$ to $(824 \pm 11)\,\sigma$ at $t = 5300$. At this time, N_{band} has already significantly grown to 260 ± 60 particles, which is no longer due to fluctuations with high probability. The band then approaches the center until the minimum position $r/\sigma = 250 \pm 15$ at $t = 6700$. Between $t = 5300$ and $t = 5900$, N_{band} grows almost linearly up to 2450 ± 90 particles, before the growth slows down to a slower, still approximately linear regime until $N_{\text{band}} = 3880 \pm 60$ at $t \approx 6700$. After that, only few particles join the band, while r_{band} rises again slightly. This is due to the fact that fast particles begin to diffuse back into the system, i.e. the dense region gets broader.

We can compare d_{band} to its width as expected from Fig. 5.2, i.e. the region in the plot where $\langle\phi\rangle > 2\phi_0$. We find that at $d_{\text{band}}(t = 5600)/\sigma = 45$, while from that plot we would have guessed roughly $80\,\sigma$. This deviation can be explained from inspection of Fig. 5.12(b) where we see that the band is not perfectly circular, but

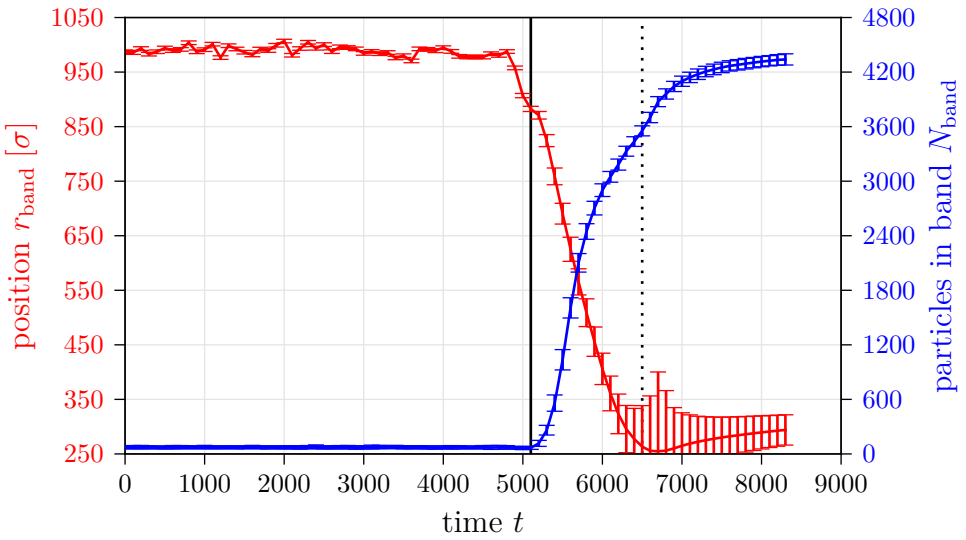

Figure 5.11.: Number of particles in the band N_{band} and its position r_{band}

generally closer to the center for $x < 0$ than for $x > 0$ in this snapshot. While we take this into account in our calculations in this chapter, we average over circular areas in Fig. 5.2, thus leading to a broader band.

In the interval $5200 \leq t \leq 6000$ the band moves with almost constant average speed $v_{\text{band}} \approx 0.058$, which is roughly 1/3 of the mean speed of the particles in it (see Fig. 5.1(b)). This means that the particles themselves travel three times the distance the band does and is due to their frequent reversals and the fact that they do not necessarily swim parallel to the gradient but possibly at a slight angle to it (compare to trajectories in Fig. 5.9).

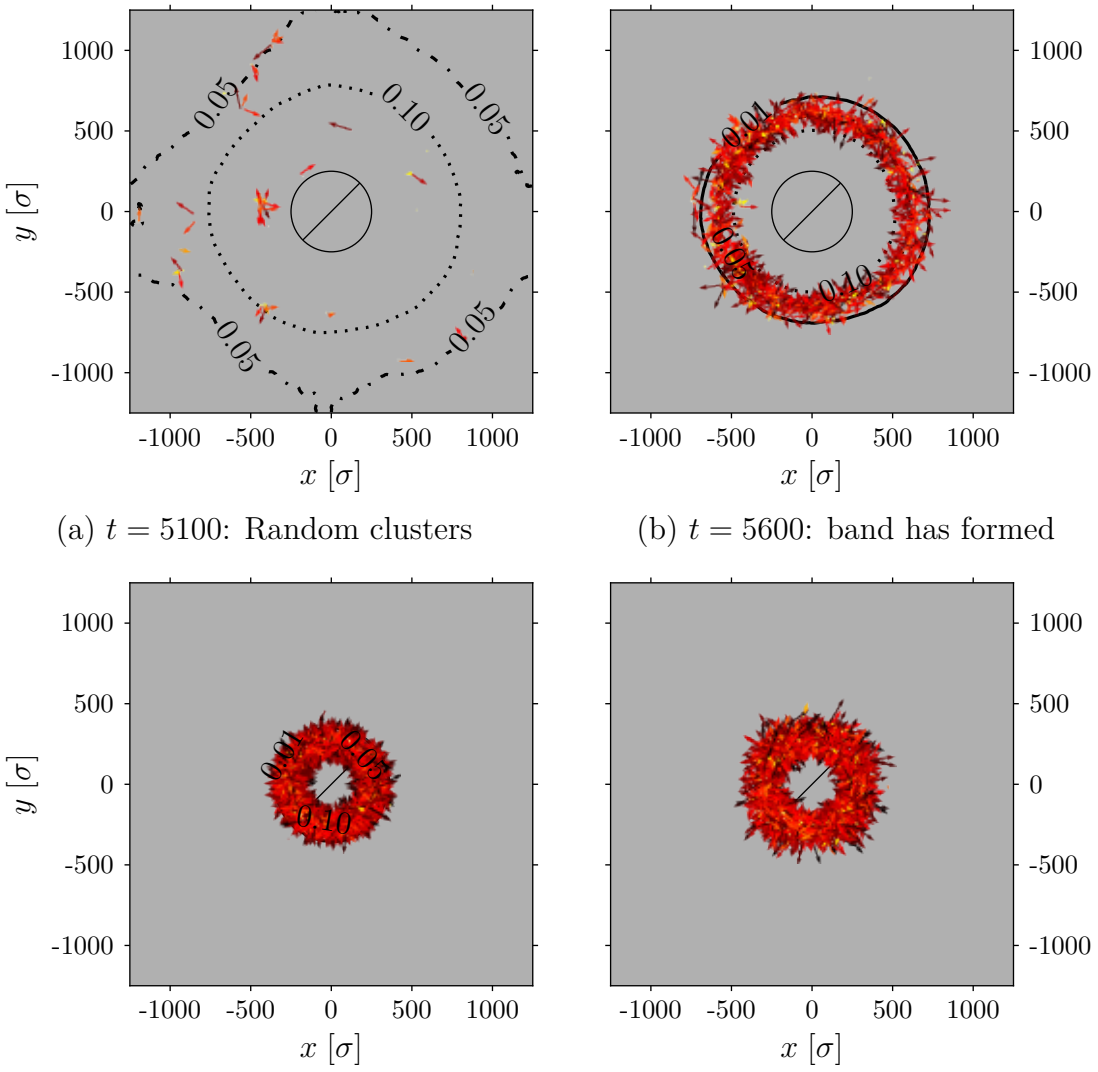

(a) $t = 5100$: Random clusters

(b) $t = 5600$: band has formed

(c) $t = 6500$: band has reached bubble

(d) $t = 8000$: particles diffuse back

Figure 5.12.: Particles belonging to the band for different times t

In Fig. 5.12 we display snapshots of all particles belonging to the band with the given definition in one run. We can see that for $t = 5100$ several clusters have formed throughout the system (see Fig. 5.12(a)). This makes us see that our definition of the band is not perfect because we would have expected a band-like structure for this time already. However, for $t = 5600$ in Fig. 5.12(b) this is clearly the case, where we can see an almost circular band covering the $c = 0.05$-isoline. At $t = 6500$ in Fig. 5.12(c) the particles form a very dense ring around the centre, which has become broader at $t = 8000$ (see Fig. 5.12(d)). The main difference between the last two snapshots is that for $t = 8000$ we spot more arrows pointing away from the bubble. In all cases we can see that the plot is dominated by dark, i.e. fast particles. On the one hand, this is related to the fact that dark arrows are longer than bright arrows and therefore take more space. On the other hand, as we know from Fig. 5.1(b), particles in the band possess higher speed on average, so we would also expect to observe this phenomenon.

5.2. System with low noise

In this chapter we consider a system with the same parameters as in Table 5.1 apart from the noise η: We set $\eta = 0.1$, i.e. we reduce the thermal noise in order to see in how far this parameter changes the results we obtained in Chap. 5.1.1.

5.2.1. Density and speed

The space-time plot of the average filling fraction displayed in Fig. 5.13(a) looks qualitatively the same as the one in Fig. 5.1(a): One can see that filling fraction and speed remain homogeneous up to $t \approx 5000$ (solid black line). At $t = 5100$, the average local filling fraction at a distance of $r/\sigma \approx 1100 \pm 100$ is already higher than the average (see Fig. 5.14). However, the plots differ quantitatively in so far as this time, the bubble is only reached by the densest part of the band at $t \approx 6800$ (dotted lines in Fig. 5.13 and the following plots), i.e. slightly later than in the system with stronger noise. Furthermore, both the peak filling fraction when the band reaches the bubble and the width of this dense region are higher for that case. The minimum filling fraction is roughly 0.6 ϕ_0, so here there is no dip down to 0.3 ϕ_0 for $r/\sigma \approx 600$.

The average speed, depicted in Figs. 5.13(b) and A.2, shows corresponding differ-

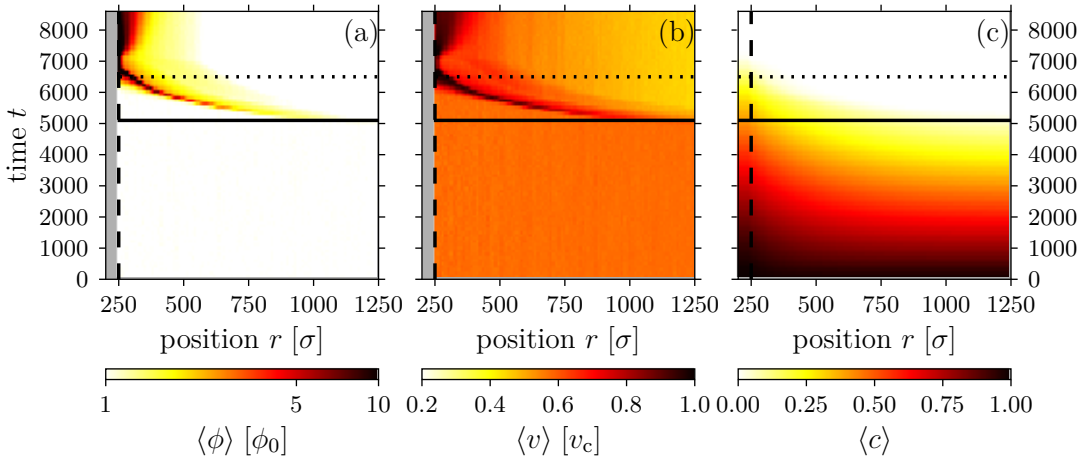

Figure 5.13.: Space-time plots of mean local filling fraction $\langle\phi\rangle$, mean speed $\langle v\rangle$ and mean oxygen concentration $\langle c\rangle$ for a system with $\eta = 0.1$

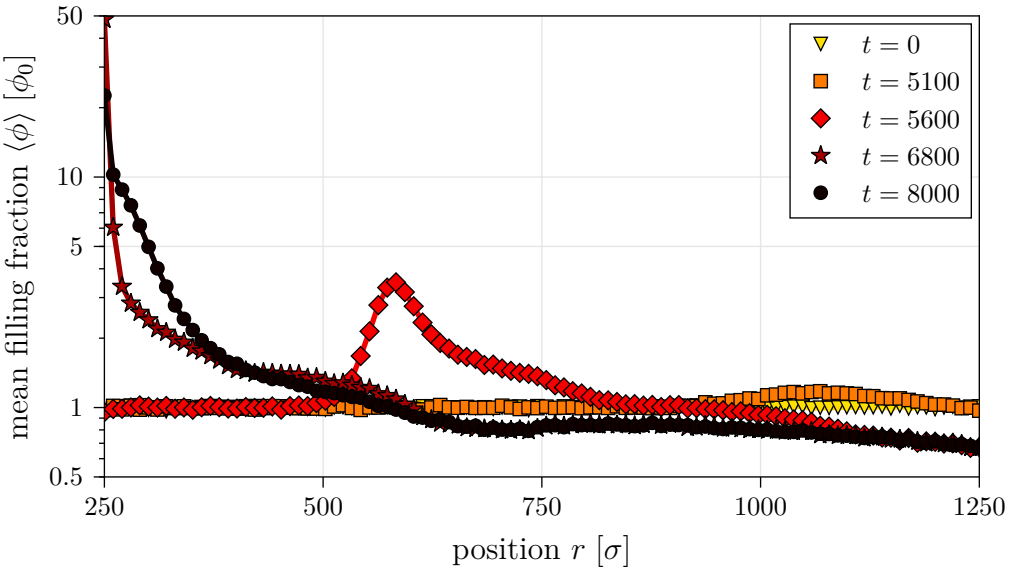

Figure 5.14.: Filling fraction profiles for a system with $\eta = 0.1$

ences: This time we can make out a continuous transition from fast particles close to the bubble to slow particles far away from it for all times after the appearance of the band, whereas Figs. 5.1(b) and 5.3 show a dip for intermediate values of r. However, we see that for $t \gtrsim 7200$ density and average speed grow again farther away from the bubble as particles begin to diffuse into the system. The oxygen concentration $\langle c\rangle$, displayed in Figs. 5.13(c) and A.3, looks identical to the one we observed in Chap. 5.1.2.

5.2.2. Positional and orientational ordering

In Fig. 5.15 we display the temporal evolution of $g(\Delta r), C_1^{re}$ and C_2^{re}. The first shows again no visible signal until $t \approx 6000$. However, looking at Fig. 5.16 we can see that the function at $t = 5600$ is already slightly larger than at $t = 5100$. We see that the band is densest at $t \approx 6800$ when it has reached the bubble. As could be expected from the density plots, the peak values of $g(\Delta r)$ are lower than the corresponding peaks in Fig. 5.5 for $\eta = 5$.

C_1^{re}, displayed in Figs. 5.15(b) and 5.17, looks qualitatively the same as in the

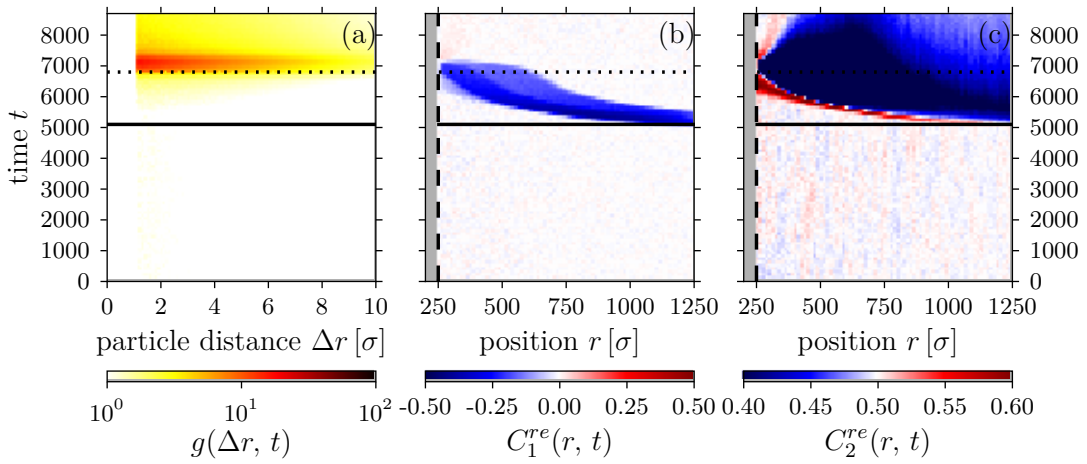

Figure 5.15.: Space-time plots of radial distribution function $g(\Delta r, t)$ and position-orientation scalar products $C_{1/2}^{re}(r, t)$ for a system with $\eta = 0.1$

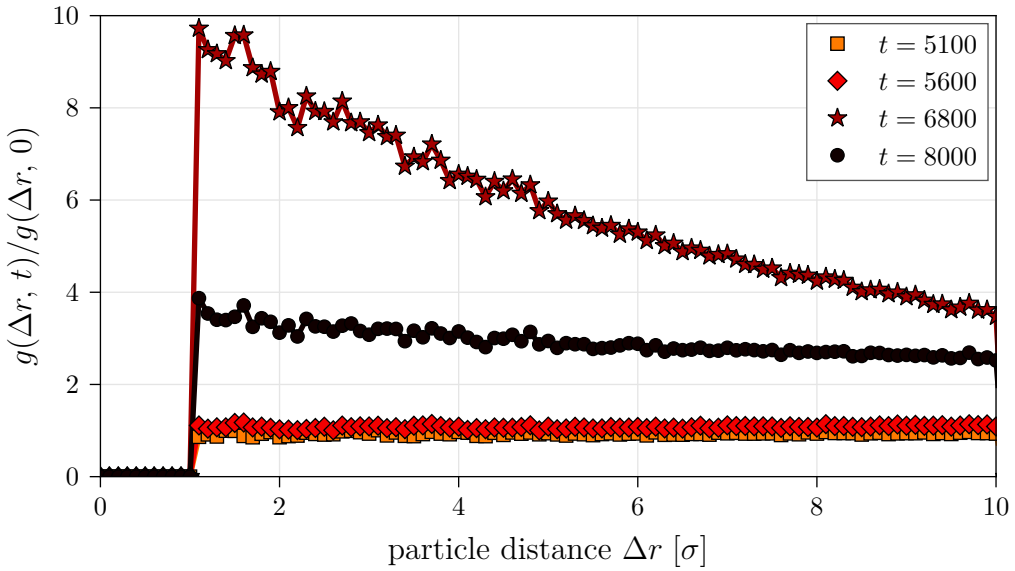

Figure 5.16.: Normalized radial distribution function $g(\Delta r, t)$ for a system with $\eta = 0.1$

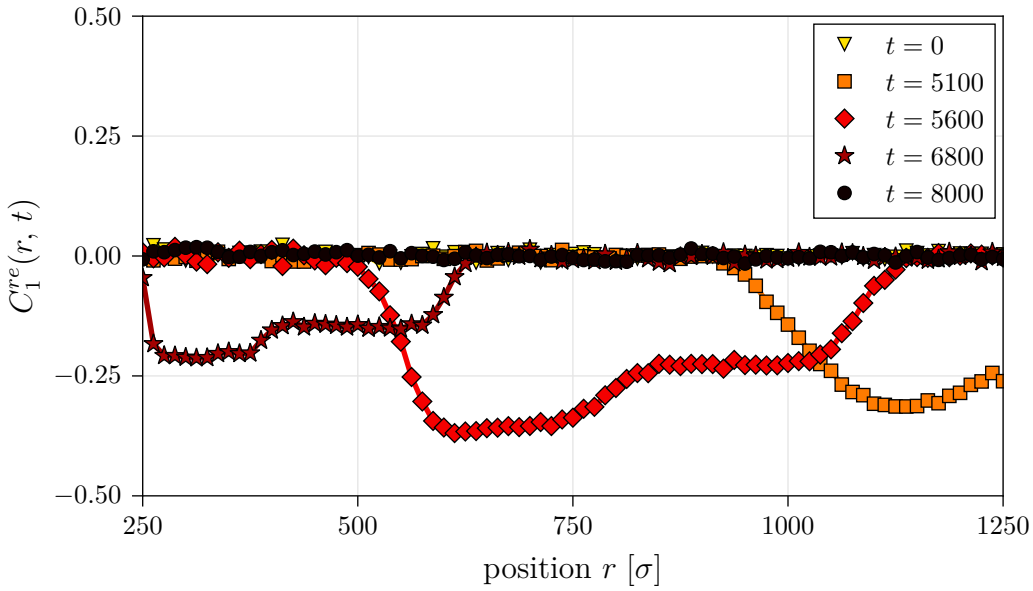

Figure 5.17.: Profiles of position-orientation scalar product $C_1^{re}(r,t)$ for a system with $\eta = 0.1$

case with $\eta = 5$, even though slightly less distinct. Still we can clearly make out the general tendency of the particles to approach the bubble for $5100 \lesssim t \lesssim 7000$. This time, also C_2^{re} shows an amplitude, which is mostly below average (see Figs. 5.4(c) and 5.18, respectively). Because we know that this quantity only becomes zero when the scalar product is zero itself, i.e. when particles move orthogonal to their position vector, this means that they move in circles around the centre. This is only possible of course because we are dealing with a system with low thermal noise. Only in front of this blue region, i.e. closer to the bubble, the particles have a tendency to swim parallel (or antiparallel) to the oxygen gradient, rather than perpendicular to it. This area corresponds to the first front of the band containing the fastest particles swimming towards the centre, which becomes clear when one compares the curves for $t = 5600$ in Figs. 5.18 and 5.14.

5.2.3. Correlation functions

We show the spatial particle orientation correlation functions for different times in Fig. 5.19 with a logarithmic plot of the average density as a function of distance r between it. C_1^{ee} looks very similar to the correlations discussed in Chap. 5.1.1, including the fact that the correlation in the band vanishes when it comes close to the bubble (see Fig. 5.22(c)).

As for C_2^{re} before, C_2^{ee} shows an amplitude in the low-noise case, too: For $t \geq 5600$

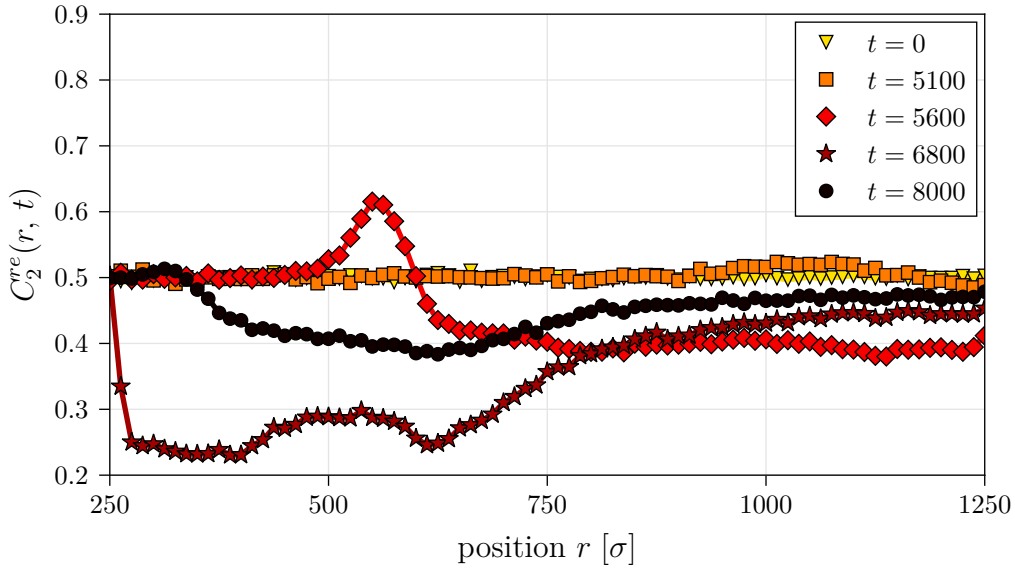

Figure 5.18.: Profiles of position-orientation scalar product $C_2^{re}(r,t)$ for a system with $\eta = 0.1$

we find several regions: The main part of the band is at $r/\sigma \approx 600$, indicated by the dark region in the density plot in the centre. This explains why there is positive correlation for $r/\sigma \approx 600$ and $0 \lesssim \Delta r/\sigma \lesssim 75$. The big, red region above is due to a different fact: Keeping in mind Fig. 5.18 and having a look at Fig. 5.22(b) where we plot 1000 randomly chosen particles one can see that for large values of r many particles move perpendicular to the gradient. Therefore, these particles move either parallel or antiparallel to each other, thus explaining positive correlation.

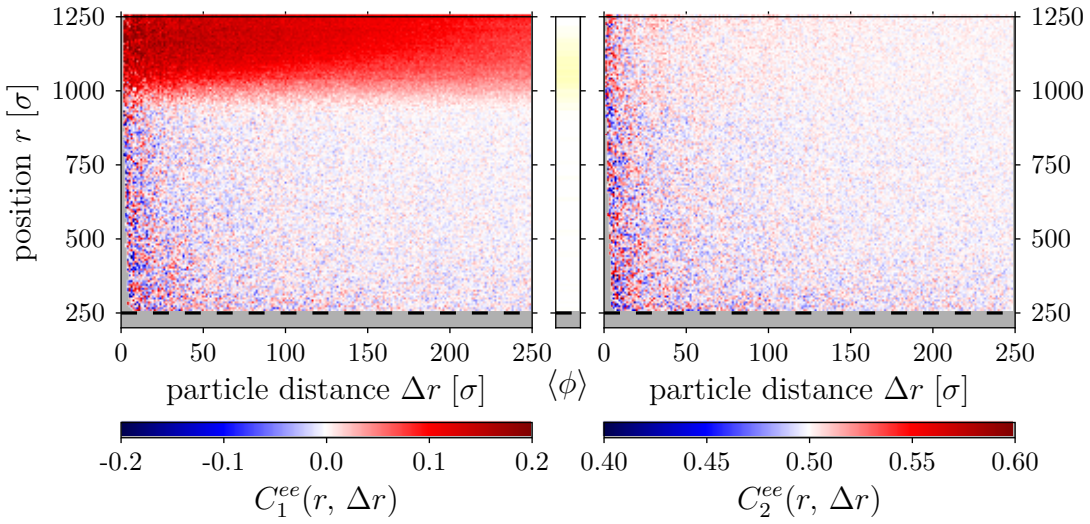

(a) $t = 5100$: early band situation

Figure 5.19.: Spatial orientation correlation functions for a system with $\eta = 0.1$

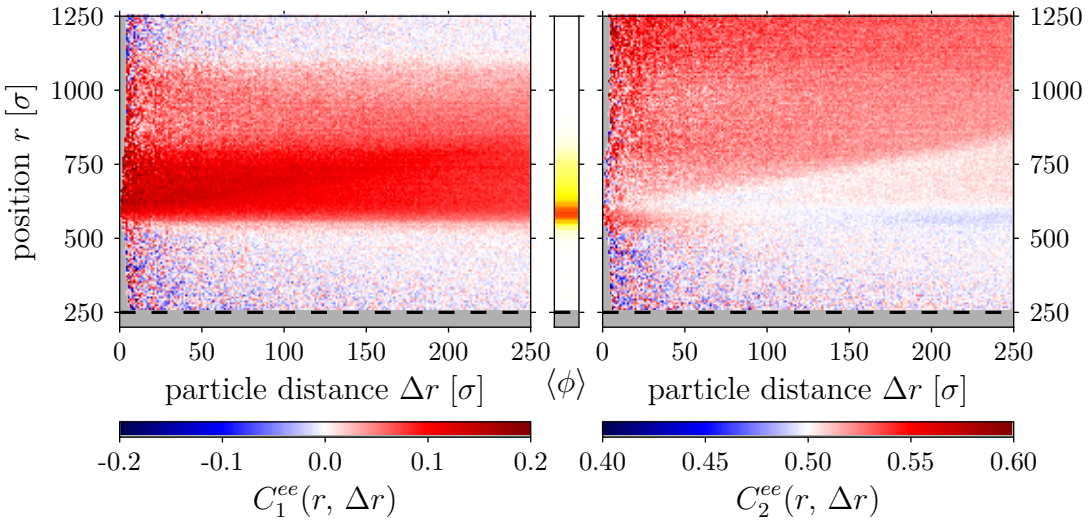

(b) $t = 5600$: intermediate band situation

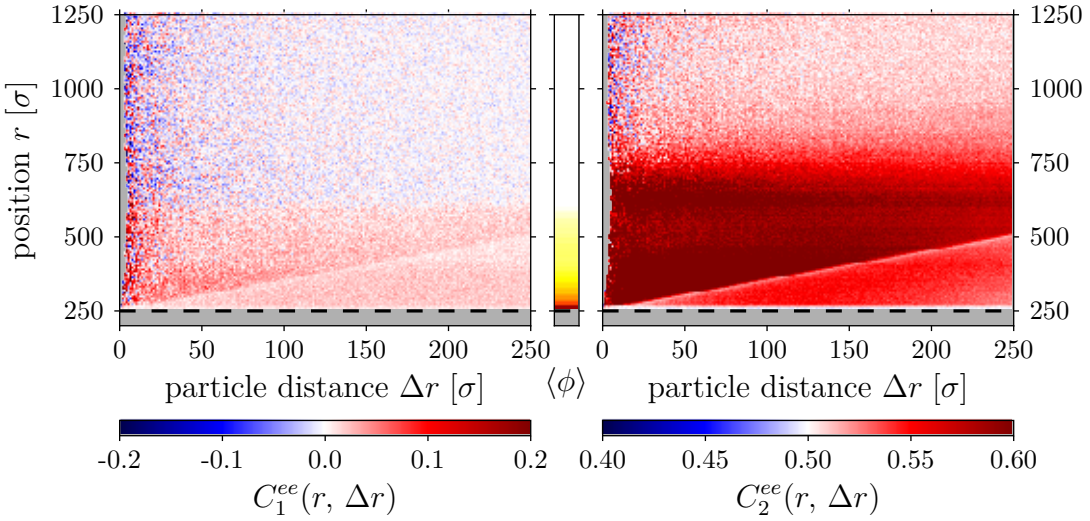

(c) $t = 6800$: band reaches the bubble

Figure 5.19.: Spatial orientation correlation functions for a system with $\eta = 0.1$

The slightly blue stripe for $200 \lesssim \Delta r/\sigma \lesssim 250$ results from this phenomenon, too, stemming from band particles in the band oriented perpendicular to these particles. The brighter, triangular area with increased density between $r/\sigma \approx 600$ and $r/\sigma \approx 800$ is due to uncorrelated orientations between particles following the band and these in front of it. The latter are also clearly the reason for the uncorrelated region for $250 \lesssim r/\sigma \lesssim 550$. C_1^{ee} does not show these features because particle orientations are either parallel *or* antiparallel, thus averaging out all contributions. Instead, the amplitude decaying with increasing r in this plot results from the general tendency of the particles to approach the bubble and their alignment due to that.

In the next plot (Fig. 5.19(c)), the band has reached the bubble. When examining C_2^{ee} one notices again the distinct, almost white line with slope one. As explained in Chap. 5.1.4, this structure is a direct consequence of the band itself, where particles collide and change their orientation frequently. The red region above implies that particles in these distances are still oriented perpendicular to the gradient, so C_2^{ee} is still positive for them. This becomes especially clear considering the snapshot in Fig. 5.22(c).

We display $C_1^{ee}(t, \Delta t)$ and $C_2^{ee}(t, \Delta t)$ in Fig. 5.20. While the former looks qualitatively the same as in Fig. 5.8 with the only non-zero feature appearing during band propagation phase, this is clearly not the case for the latter: This function, too, shows now an amplitude, which was not the case for $\eta = 5$. Because this amplitude is always positive we know that particles tend to keep their orientations, i.e. collisions with other particles are rare, while they might interact with the oxygen field and hence reverse their orientation frequently. Only during the band phase, particles have a higher probability (and therefore frequency) to move in the same direction as before, namely parallel to the oxygen gradient.

5.2.4. Typical trajectories and quiver plots

In Fig. 5.21 we show once more different types of particle trajectories for the system with $\eta = 0.1$. Again, we can differentiate between several types:

- Particles 1, 3 and 10 hardly move at all.

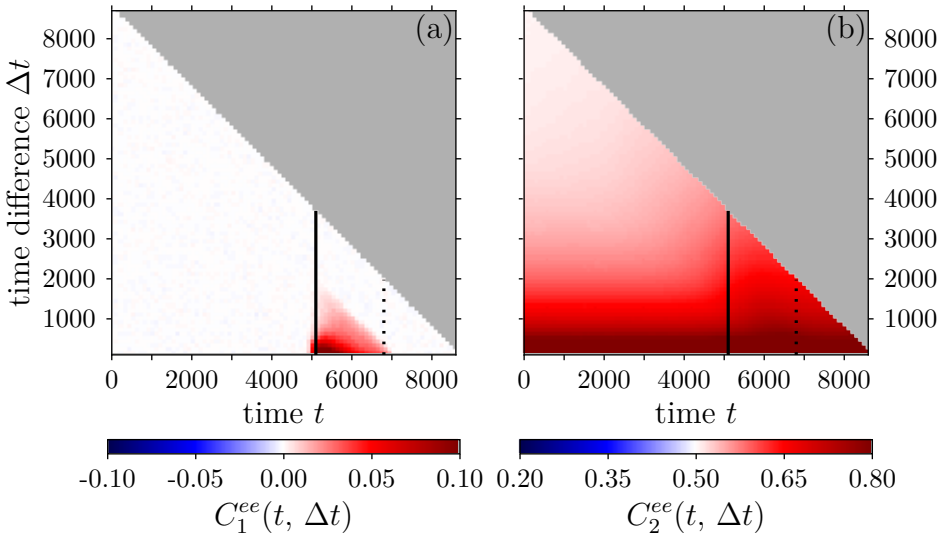

Figure 5.20.: Temporal orientation correlation functions for a system with $\eta = 0.1$

- Particles 2 and 8 perform aerotaxis towards the bubble.
- Particle 6 is also rather slow, but is clearly influenced by aerotaxis, too.
- Particles 5 and 7 have an orientation perpendicular to the oxygen gradient and therefore do not reach the bubble.
- Particles 4 and 9 are fast particles, but they are never part of the band because they are located at the boundary of the system when it forms. Probably the oxygen around them is already depleted before they can align with the gradient and hence do not follow it.

The main difference to the case where $\eta = 5$ (see Fig. 5.9) is that there are fast-moving particles, such as number 5 and 7, that are affected by aerotaxis, but not part of the band because they move perpendicular to the gradient. They are also the reason why C_2^{re} is lower than average in the regions behind the band (see Fig. 5.18).

In Fig. 5.22 we present again snapshots of 1000 randomly chosen particles. While the system at $t = 5100$ still looks the same as the system with $\eta = 5$, there is clearly a qualitative difference for the next two times (compare Figs. 5.22(b) and 5.22(c) to Figs. 5.10(b) and 5.10(c)): Behind the band a region of lower density has formed where the particles seem to move in circular trajectories around the centre. These correspond to trajectories 5 and 7 in Fig. 5.21. Because the noise is very weak and apart from collisions and orientation reversals due to the oxygen there is no other way for them to change their orientation, they always stay perpendicular to the band

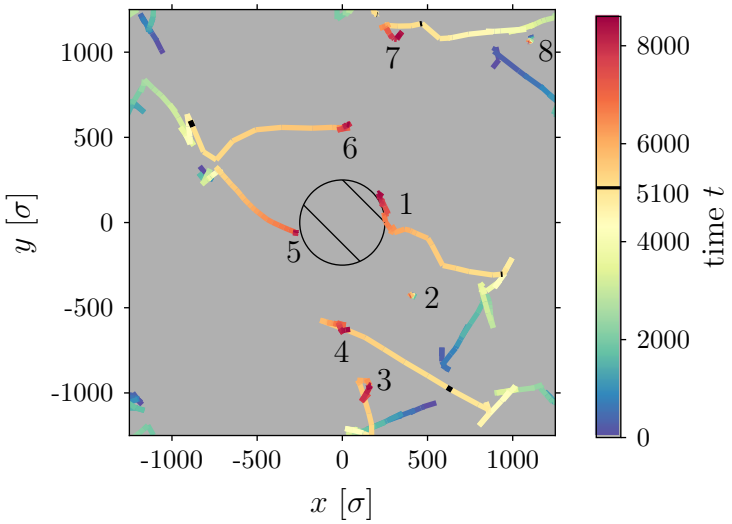

Figure 5.21.: Typical particle trajectories for a system with $\eta = 0.1$

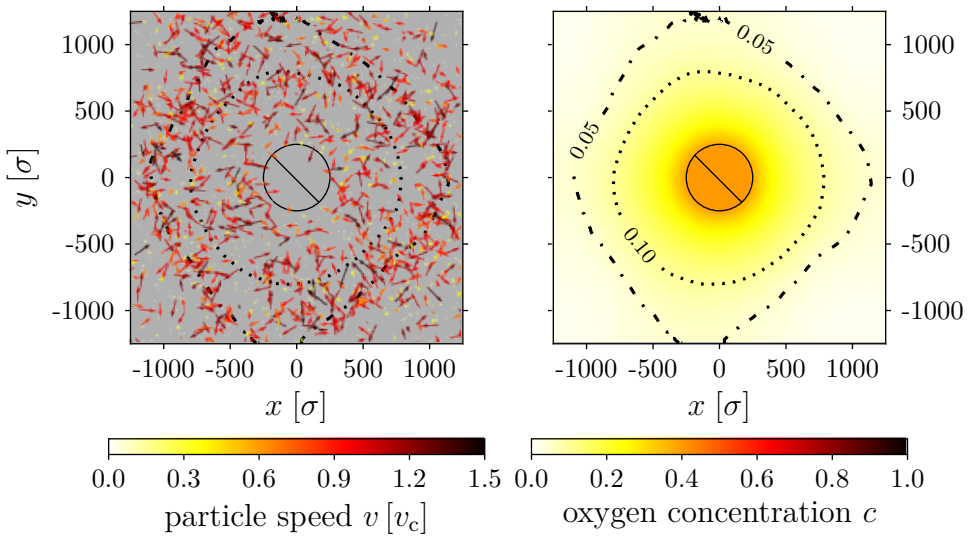

(a) $t = 5100$: early band situation

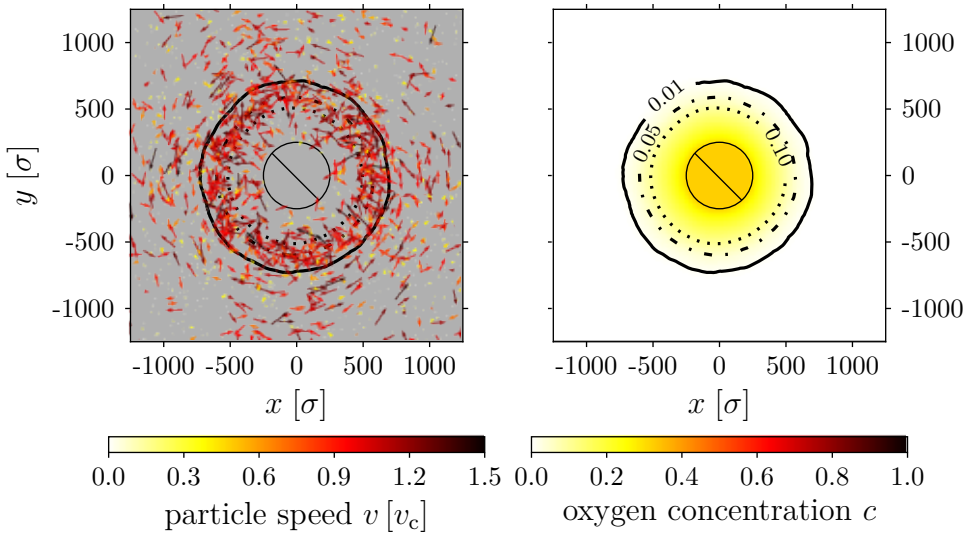

(b) $t = 5600$: intermediate band situation

Figure 5.22.: Particle configurations for a system with $\eta = 0.1$

and can therefore only be part of it for a very short time period. In Fig. 5.22(d) these particles still exist, but the picture is now again dominated by those particles that have diffused back into the system from the vicinity of the bubble after all oxygen has been consumed.

5.2.5. Statistics of the band

We plot the distance from the band to the centre and the number of particles in it in Fig. 5.23. The plots look qualitatively the same to the case for $\eta = 5$ on first view,

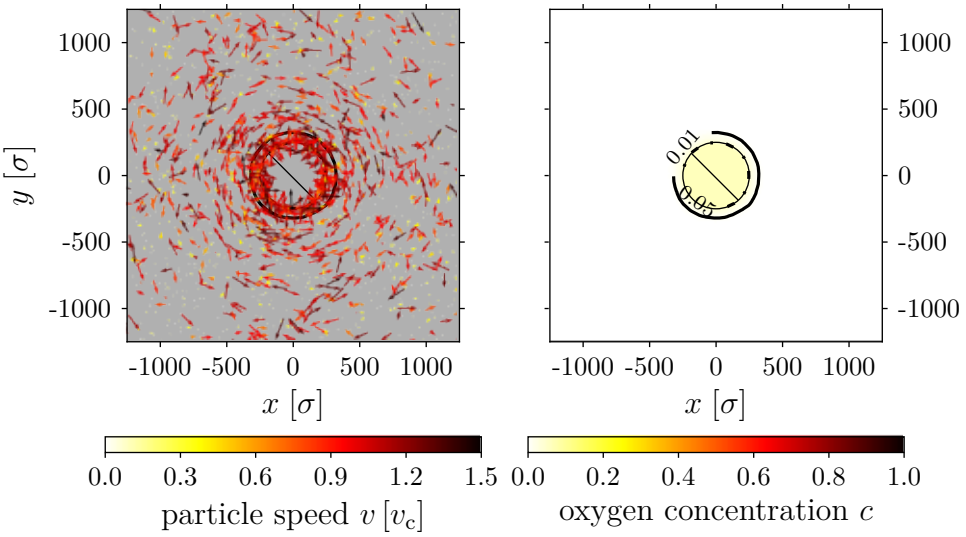

(c) $t = 6800$: band reaches bubble

Figure 5.22.: Particle configurations for a system with low noise

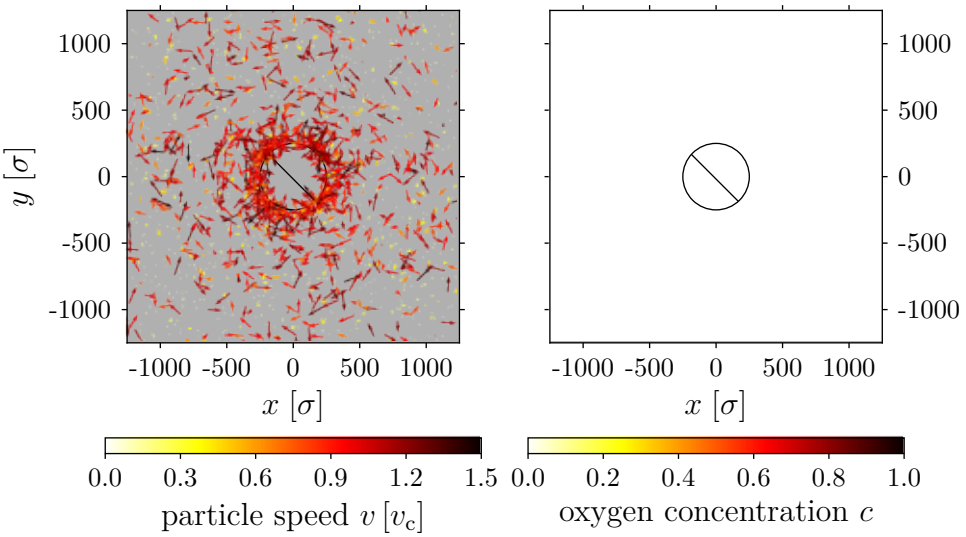

(d) $t = 8000$: situation after all oxygen has been consumed

Figure 5.22.: Particle configurations for a system with $\eta = 0.1$

but differ quantitatively: The first deviations from the initial values of N_{band} and r_{band} appear at $t = 5200$. Contrary to the case with stronger noise where the speed of the band stays almost constant, this time it slows down upon approaching the centre: Its average in the interval $5200 \leq t \leq 6800$ is roughly 0.039, but it amounts to 0.066 for $t \leq 5800$ and only 0.023 afterwards. Also the number of particles N_{band} belonging to the band is different from the calculations with $\eta = 5$: Indeed it rises again until $t = 6500$, where it peaks to a value $N = 2370 \pm 70$ particles, but this value

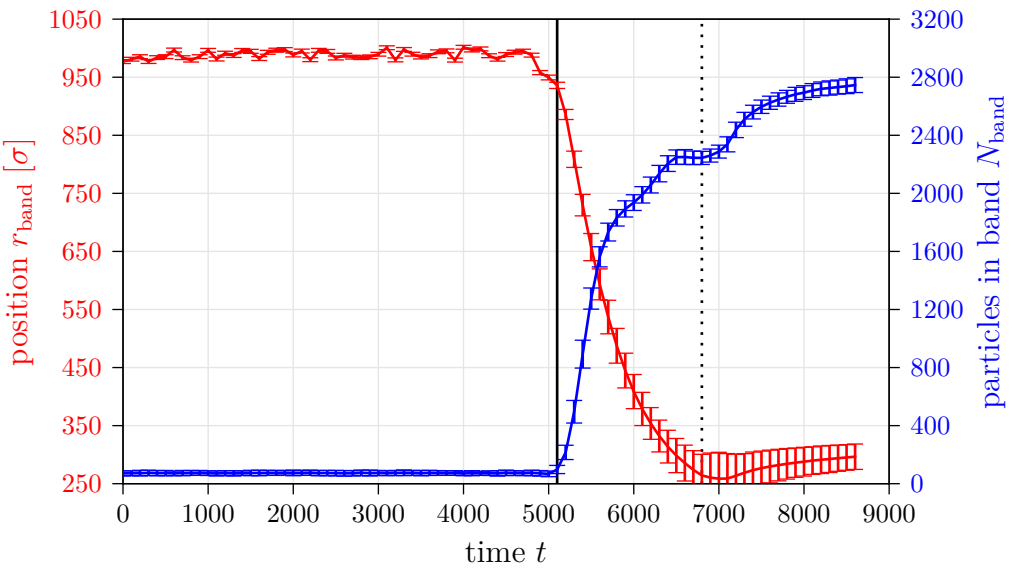

Figure 5.23.: Number of particles in the band N_{band} and its position r_{band} for a system with $\eta = 0.1$

is 1000 particles below the one in the previous case. Between $t \approx 6500$ and $t = 7000$ N_{band} stagnates at this level, before it rises again slowly. This stagnation occurs because the band is so close to the bubble that it does not pick up new particles on the one side, while on the other side there are hardly any slower particles swimming in direction of the band joining it from the outside. This is different from the situation in Fig. 5.11, where many slightly slower particles were aligned parallel to the gradient and could thus join the band while it slowed down.

The smaller number of particles in the band and its slowdown are mutually dependent: Initially, N_{band} is lower than for the higher noise case because many fast particles are not able to follow the band (see trajectories in Fig. 5.21). This leads to a decreased number of particles inside it and thereby to decreased total oxygen consumption. Therefore, the oxygen has more time to diffuse out of the bubble and for a given time t the threshold oxygen concentration $c_{\text{ideal, min}}$ will always be farther away from the bubble for $\eta = 0.1$ than for $\eta = 5$.

5.2.6. Diffusion coefficients and Péclet numbers

In this section we calculate diffusion coefficients and Péclet numbers of the two systems considered in Chaps. 5.1 and 5.2. To this end, we first plot the mean squared displacement

$$\text{MSD} \equiv \langle (\boldsymbol{r}(t) - \boldsymbol{r}(0))^2 \rangle, \tag{5.9}$$

from which we extract the diffusion rate

$$D \equiv \lim_{t\to\infty} \frac{\langle (\boldsymbol{r}(t) - \boldsymbol{r}(0))^2 \rangle}{6t}. \tag{5.10}$$

This is the corresponding case in three dimensions to the one-dimensional case we presented in Eq. (2.5). The Péclet number $\mathscr{P}$ is a dimensionless quantity that denotes the ratio of advective to diffusive forces in a system [42]:

$$\mathscr{P} \equiv \frac{\text{advective propagation}}{\text{diffusive propagation}} \equiv \frac{\bar{v} L_z}{D}. \tag{5.11}$$

We display the MSD for four different situations in Fig. 5.24: Apart from the noise η, we differentiate between two turning probabilities $p_{\text{turn}} = 1.25 \times 10^{-3}$ and $p_{\text{turn}} = 6.25 \times 10^{-3}$, respectively. Because we have set $\kappa = 0$, i.e. there is no oxygen consumption in the simulation, the latter are valid throughout the whole system and for all times. By this means we can calculate the particle diffusion rates for an aerobic (high oxygen $\Rightarrow p_{\text{turn}} = 1.25 \times 10^{-3}$) and for an anaerobic environment (low oxygen $\Rightarrow p_{\text{turn}} = 6.25 \times 10^{-3}$).

We can see that there is almost no difference between the different noises for an aerobic environment. In the anaerobic case, the diffusion turns out marginally larger for $\eta = 0.1$. This is a contrast to common systems of particles where the mean squared displacement increases with larger noise. Because we are dealing with self-propelled particles here this is not the case, though. As we have seen in

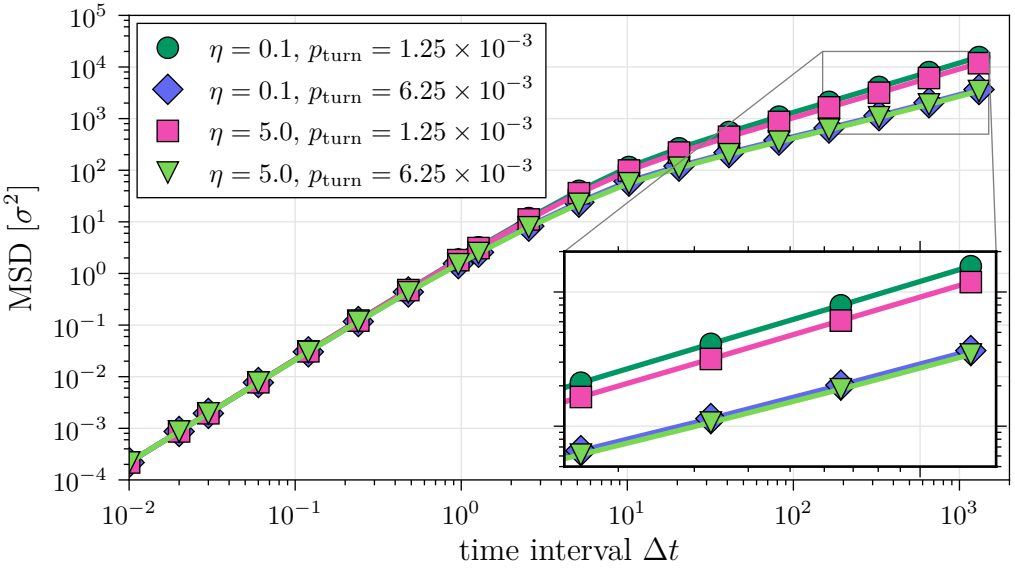

Figure 5.24.: Mean squared displacements

		$p_{\text{turn}} = 1.25 \times 10^{-3}$	$p_{\text{turn}} = 6.25 \times 10^{-3}$
D:	$\eta = 0.1$	1.972(13)	0.453(12)
	$\eta = 5$	1.499(13)	0.424(11)
$\mathscr{P}$:	$\eta = 0.1$	5.83(4)	25.386(29)
	$\eta = 5$	7.67(7)	27.123(23)

Table 5.2.: Diffusion coefficients D (in σ^2/ time unit) and Péclet numbers $\mathscr{P}$

Fig. 5.9, a larger noise leads to more warped trajectories instead of straight lines like in Fig. 5.21. Instead of η, the determining factor for the diffusivity is p_{turn}: The final mean squared displacement is approximately five times higher for the aerobic environment. This is of course due to the frequent particle reversals that prevent them from covering large distances.

In general we can make out two linear regimes in the graphs: For $t \lesssim 3$, i.e. 300 time steps, we are in the ballistic regime, i.e. the propagation is dominated by self-propulsion, and $\langle(\Delta r)^2\rangle \sim t^2$. A second regime with smaller slope and $\langle(\Delta r)^2\rangle \sim t$ can be identified for $t \gtrsim 10$, where reorientations due to noise or reversals become dominant. Based on this slope, we can now make use of Eq. (2.5) to calculate the diffusion coefficient D for the situations presented here. We note that we consider all particles independent of their speed.

To calculate $\mathcal{P}$, we insert the average speed $\bar{v} = 1.15\ \sigma$/time unit (see Chap. 5.1.2) in Eq. (5.11) to quantify the advective propagation in our system. The diffusive part is described by the diffusion coefficient divided by a characteristic distance, which we choose to be L_z. These values lead to the Péclet numbers given in Tab. 5.2. We see that our values are $\mathcal{O}(10)$, which lies inbetween typical Péclet numbers for bacteria ($\mathcal{O}(10^{-2} - 10^{-3})$, [44]) and these of other microorganisms (e.g. $\mathcal{O}(10^2)$ for volvocalean green algae, [45]).

5.2.7. Intermediate noise

Figure 5.25 shows the evolution of an ensemble of 100 systems with $\eta = 1$, i.e. intermediate noise. The solid line marks $t = 5100$, while the dotted line marks $t = 6500$ when the band reaches the bubble, which coincides with the time for $\eta = 5$ (see Fig. 5.13). Considering plots 5.25(a), 5.25(b) and in particular $C_2^{re}(r,t)$ in Fig. 5.26(c) we can state that the evolution of the system shows features of both the cases for $\eta = 5$ and $\eta = 0.1$: While the local densities are comparably high as for $\eta = 5$ and the speed profiles show the characteristic dip for $t \geq 6500$ (see

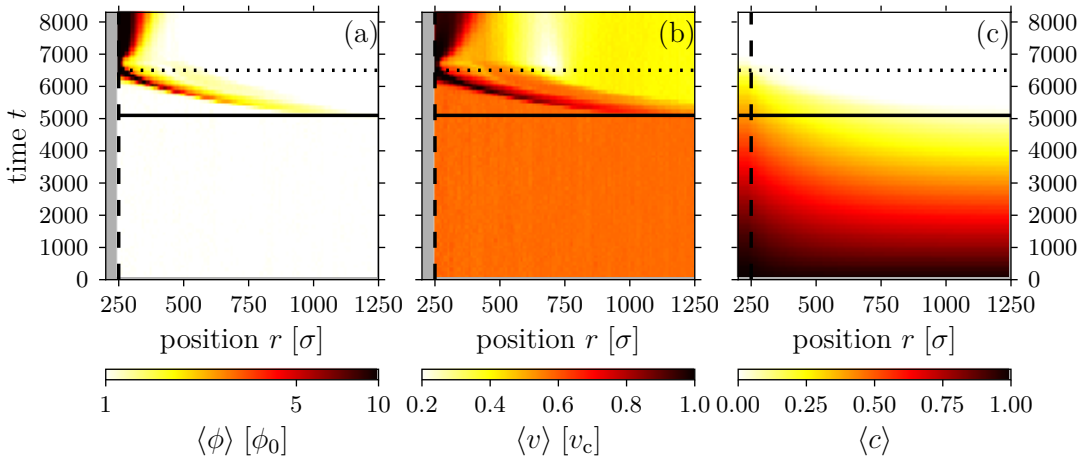

Figure 5.25.: Space-time plots of mean local filling fraction $\langle\phi\rangle$, mean speed $\langle v\rangle$ and mean oxygen concentration $\langle c\rangle$ for a system with $\eta = 1$

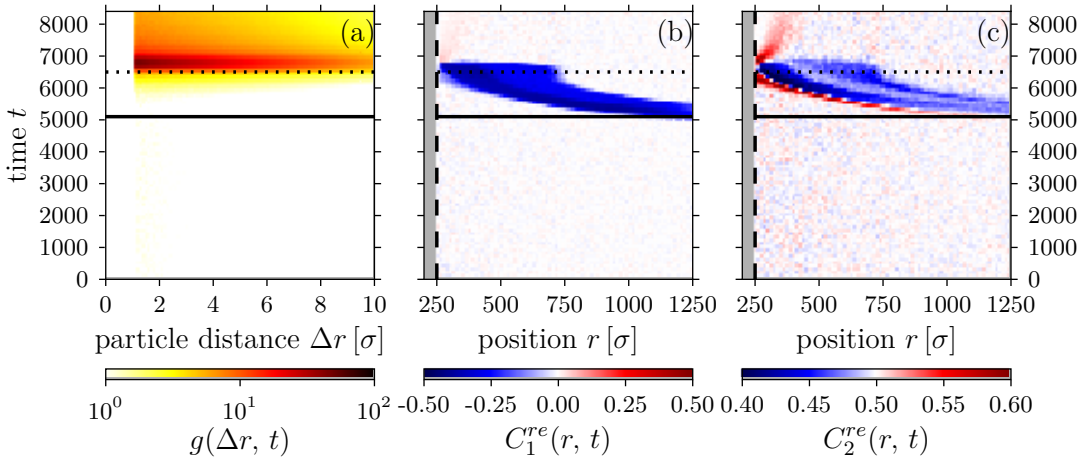

Figure 5.26.: Space-time plots of radial distribution function $g(\Delta r, t)$ and position-orientation scalar products $C^{re}_{1/2}(r, t)$ for a system with $\eta = 1$

also Figs. A.4 and A.5), we observe non-zero values in $C_2^{re}(r, t)$, even though weaker than for $\eta = 0.1$ (see also Fig. A.6). This classification is endorsed by the values of the temporal correlation function $C_2^{ee}(t, \Delta t)$ in Fig. A.7, showing that on average orientation correlations have decayed after $\Delta t \approx 300$.

5.3. Effect of parameter variations

5.3.1. Filling fraction

In Fig. 5.27 we display space-time plots of $\langle\phi\rangle$, $\langle v\rangle$ and $\langle c\rangle$ for a system with filling fraction $\phi_0 = 10^{-2}$ and other parameters according to Tab. 5.1. To this end, we

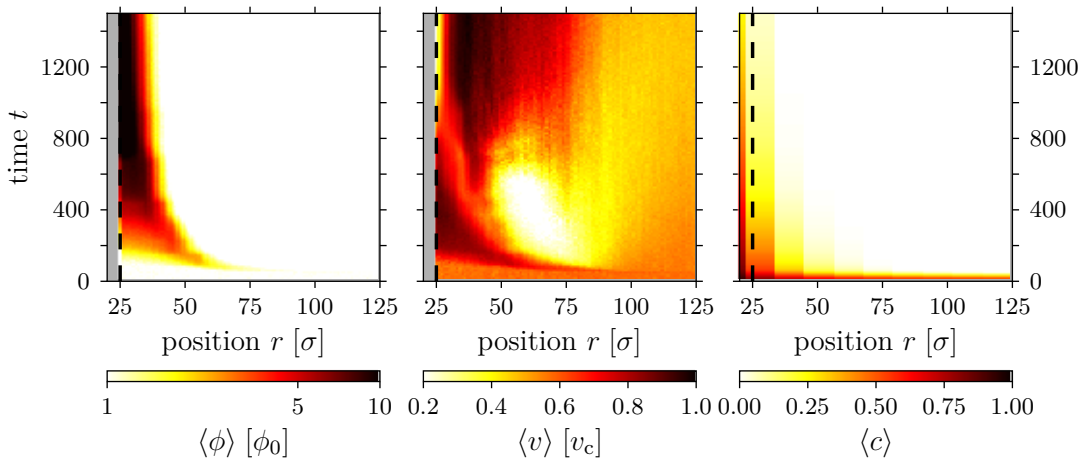

Figure 5.27.: Space-time plots of mean local filling fraction $\langle\phi\rangle$, mean speed $\langle v\rangle$ and mean oxygen concentration $\langle c\rangle$ for a system with $\phi_0 = 10^{-2}$

reduce the size of our container to $250\,\sigma$ in x- and y-direction, but keep the number of particles constant. We also keep the initial oxygen concentration per cell $c_0 = 1$ constant and thus reduce the global oxygen content C_0 by factor 100, compared to the values in Tab. 5.1. Because the number of particles per cell is now much higher, the oxygen is consumed much faster. However, we still see how a migrating band evolves and travels towards the bubble. A difference to the systems considered so far can be found in Figs. A.8 and A.9, respectively: The radial distribution function shows a small, but visible second peak around $\Delta r \approx 2.5$ indicating a shell of second next neighbours.

5.3.2. Speed rule

Figures 5.28(a) and 5.28(b) show space-time plots of $\langle\phi\rangle$, $\langle v\rangle$ and $\langle c\rangle$ for a system with the parameters from Tab. 5.1, except that we vary the speed rule: Instead of constant speed $v_i = v_{0,i}$ we choose concentration-dependent speeds according to Eqs. (3.5) and (3.6), respectively. We can see the behaviour is qualitatively the same as with independent particle speeds. However, because the average particle speed is higher now, the band propagates much faster and reaches the bubble already at $t \approx 6000$ and $t \approx 6300$, respectively. Also, especially for the two-state speed model in Fig. 5.28(a), the peak density is higher than for constant speed because more particles are able to follow the band. This impression is confirmed by the plot of $g(\Delta r)$ in Fig. A.10(a).

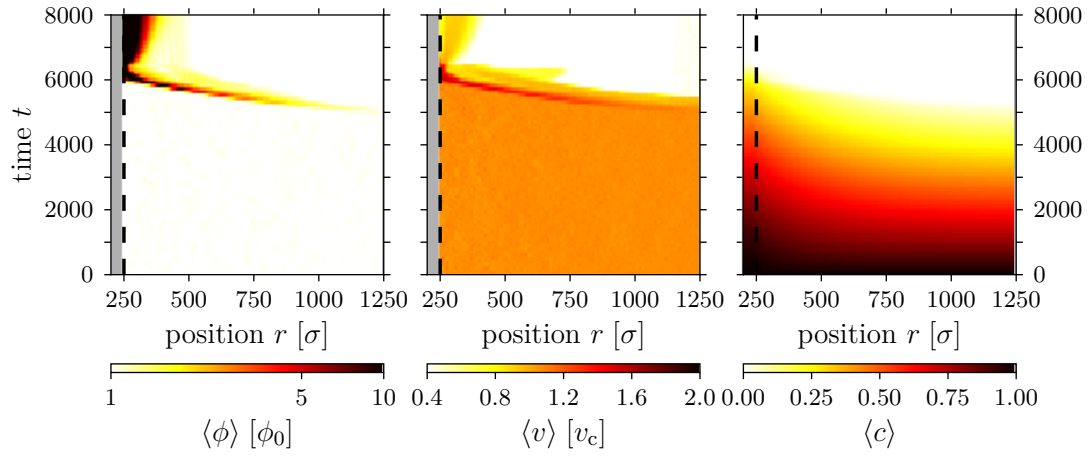

(a) Two-state speed model

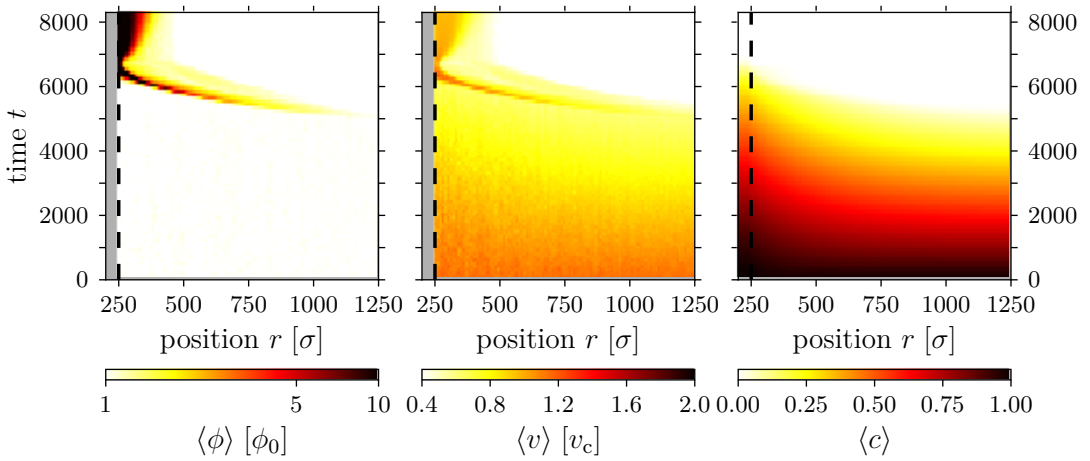

(b) Speed proportional to the concentration

Figure 5.28.: Space-time plots of mean local filling fraction $\langle\phi\rangle$, mean speed $\langle v\rangle$ and mean oxygen concentration $\langle c\rangle$ for systems with other speed rules

5.3.3. Consumption rate

In Fig. 5.29 we display space-time plots of $\langle\phi\rangle$, $\langle v\rangle$ and $\langle c\rangle$ for a system with a consumption rate $\kappa = 10^{-4}$, i.e. one order of magnitude smaller than in Chap. 5.1. We observe that the band forms only after $t \geq 50000$, i.e. ten times later than for $\kappa = 10^{-3}$. This is the expected order of magnitude, based on the total oxygen $C_{\text{consumed}} = \kappa N_{\text{part}} t$ consumed so far (see corresponding calculations in Chap. 5.1.2). Another qualitative difference appears for $t \gtrsim 57000$: We can see that some of the fast particles form a second band that travels back into the system. This is an artifact of the parameter choice: Because the amount of oxygen diffusing out of the bubble is larger than the amount the particles can consume, the concentration

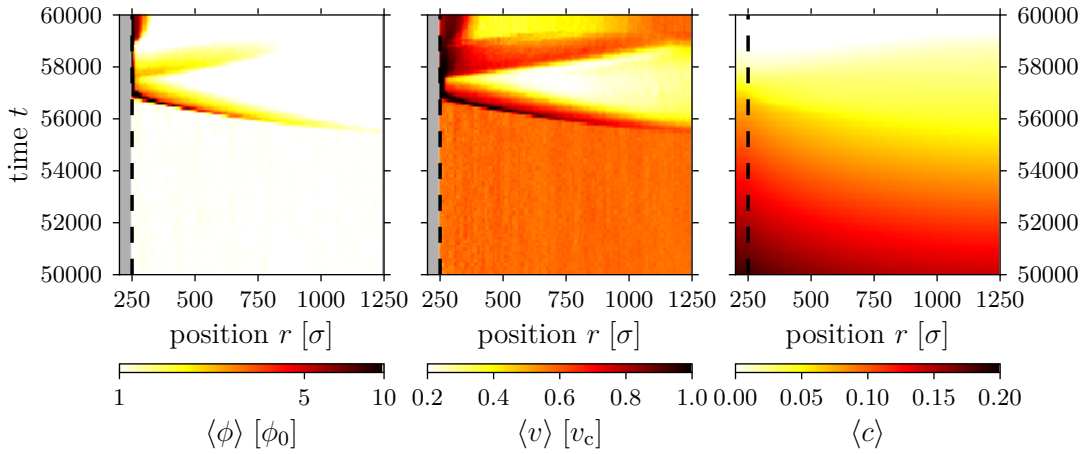

Figure 5.29.: Space-time plots of mean local filling fraction $\langle\phi\rangle$, mean speed $\langle v\rangle$ and mean oxygen concentration $\langle c\rangle$ for a system with $\kappa = 10^{-4}$

behind the band is not necessarily zero as in the cases considered so far. This observation coincides with the plot $C_1^{re}(r,t)$ in Fig. A.11, which shows us even two regions where this quantity is > 0, i.e. regions where particles move away from the centre.

5.3.4. Oxygen in the centre

Figure 5.30 shows space-time plots for a system with the same parameters as in Table 5.1, except that we set the number of virtual boxes in the bubble $N_{\text{cells, virtual}}$ to 0. This means that the bubble stores much less oxygen now and that, hence, the concentration gradient it establishes will turn out weaker.

The first consequence of this variation is that the oxygen in the system is already

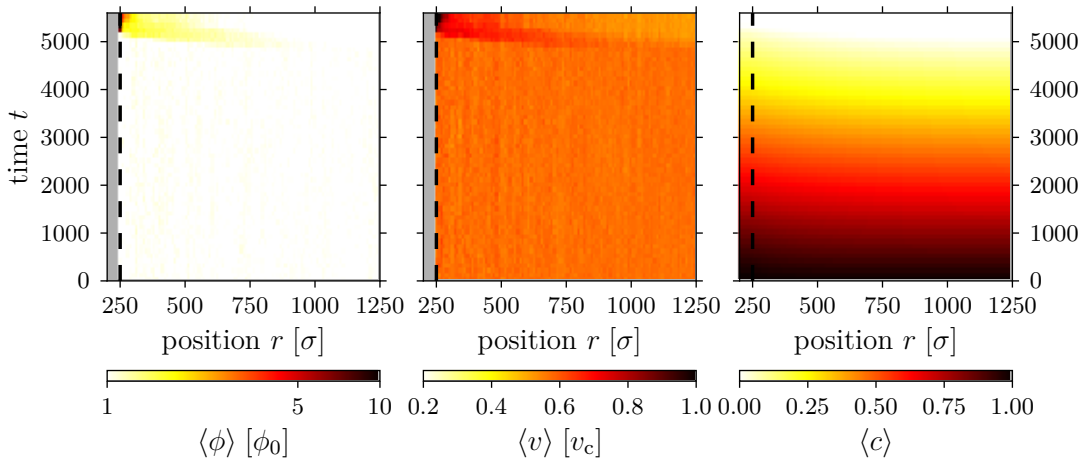

Figure 5.30.: Space-time plots of mean local filling fraction $\langle\phi\rangle$, mean speed $\langle v\rangle$ and mean oxygen concentration $\langle c\rangle$ for a system with $N_{\text{boxes, virtual}} = 0$

depleted for $t \approx 5500$ and no longer for $t \approx 8500$, because also C_0^{total} is lower than in Chap. 5.1.2. We can see that a region marginally denser than the average forms at $t \approx 5000$, so slightly earlier than in the cases considered so far. This is because the concentration in the whole system, including the outer regions where the band begins to form, is now lower than in the case with additional oxygen that comes from the bubble and diffuses into the system, i.e. the threshold concentration is reached earlier. On the other hand, the peak density in the band is comparably low. A reason for this behaviour is that the amount of oxygen coming from the bubble is too little to be noticed by all particles because it is consumed by other particles before. The immediate effect of the virtual boxes on the oxygen concentration and its gradient can be clearly seen comparing the oxygen concentration profiles in Figs. A.13 to those for the case $N_{\text{cells, virtual}} = 10^4$ in Fig. A.1.

5.3.5. Turning probability

In this section we discuss the effect of varying the turning probability p_{turn} in the Mazzag model, covering a range of five orders of magnitude. In doing so, we only modify the basic turning probability, but keep $k_1 = 1$ and $k_2 = 5$ constant, i.e. the factors determining the difference between optimal, too low and too high oxygen concentrations (see Tab. 5.1). The results present the average over 20 runs with each parameter set. Figure 5.31 shows space-time plots of average filling fractions, speeds and oxygen concentrations for $1.25 \times 10^{-6} \leq p_{\text{turn}} \leq 1.25 \times 10^{-2}$. We can see that

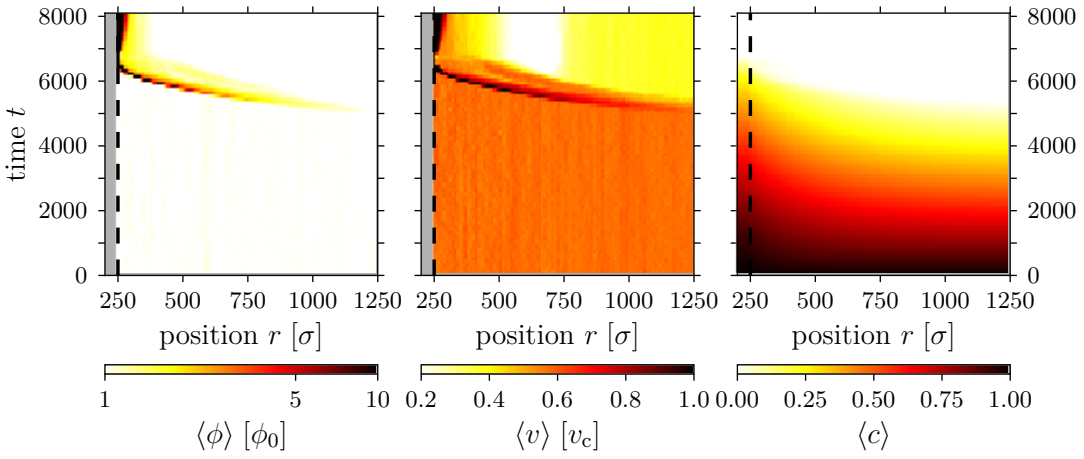

(a) $p_{\text{turn}} = 1.25 \times 10^{-2}$

Figure 5.31.: Space-time plots of mean local filling fraction $\langle\phi\rangle$, mean speed $\langle v\rangle$ and mean oxygen concentration $\langle c\rangle$ for systems with varying p_{turn}

there are only qualitative differences between the first two values: For the biggest probability in Fig. 5.31(a) the band is slightly more distinct and the spreading after reaching the bubble turns out weaker than for 1.25×10^{-3} in Fig. 5.31(b), which corresponds to the parameters discussed in Chap. 5.1.1. The differences to the next probability are much bigger: The band is still visible for $p_{\text{turn}} = 1.25 \times 10^{-4}$ (see Fig. 5.31(c)), but it is much less pronounced with peak filling fractions of $18\,\phi_0$ at $t = 7400$. The dip in the speed plot for $600 \leq r/\sigma \leq 750$ has also vanished in favour of a low-speed plateau. For $p_{\text{turn}} = 1.25 \times 10^{-5}$, displayed in Fig. 5.31(d), the band is hardly visible any longer and the peak filling fraction is only $1.8\,\phi_0$, while for the smallest value it has vanished completely (see Fig. 5.31(e)). Two more facts can be noticed: On the one hand, the oxygen consumption becomes increasingly

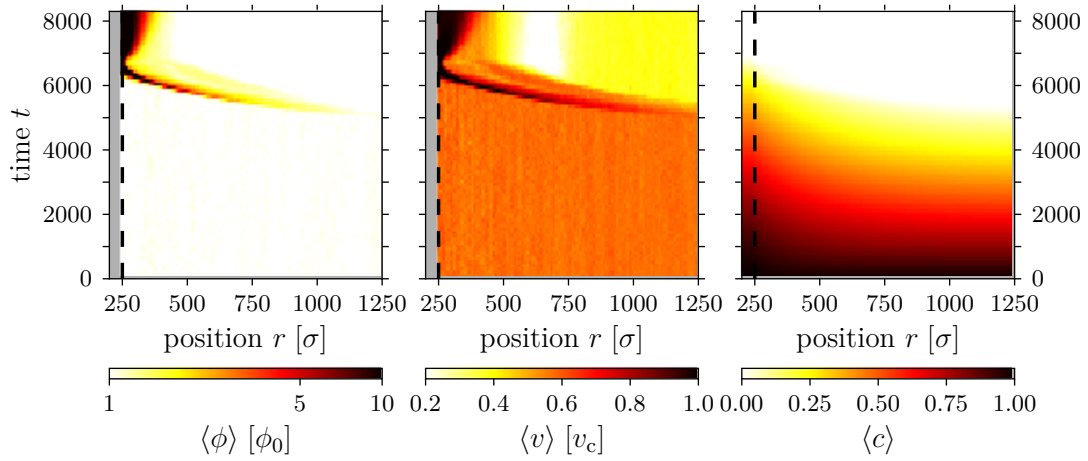

(b) $p_{\text{turn}} = 1.25 \times 10^{-3}$

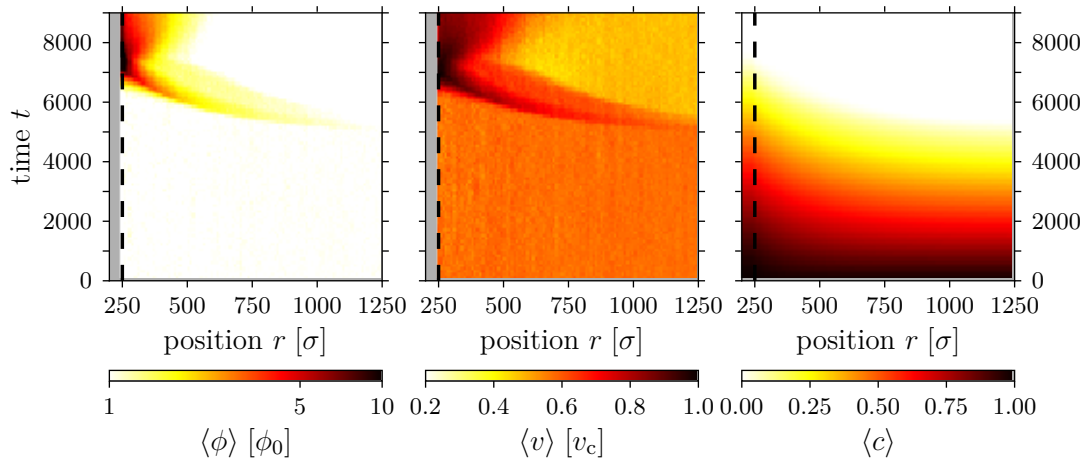

(c) $p_{\text{turn}} = 1.25 \times 10^{-4}$

Figure 5.31.: Space-time plots of mean local filling fraction $\langle\phi\rangle$, mean speed $\langle v\rangle$ and mean oxygen concentration $\langle c\rangle$ for systems with varying p_{turn}

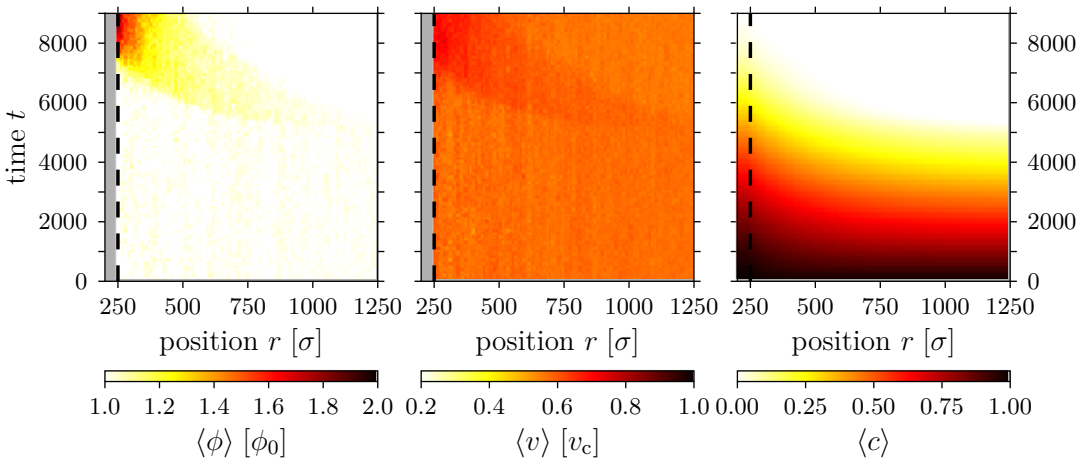

(d) $p_{\text{turn}} = 1.25 \times 10^{-5}$

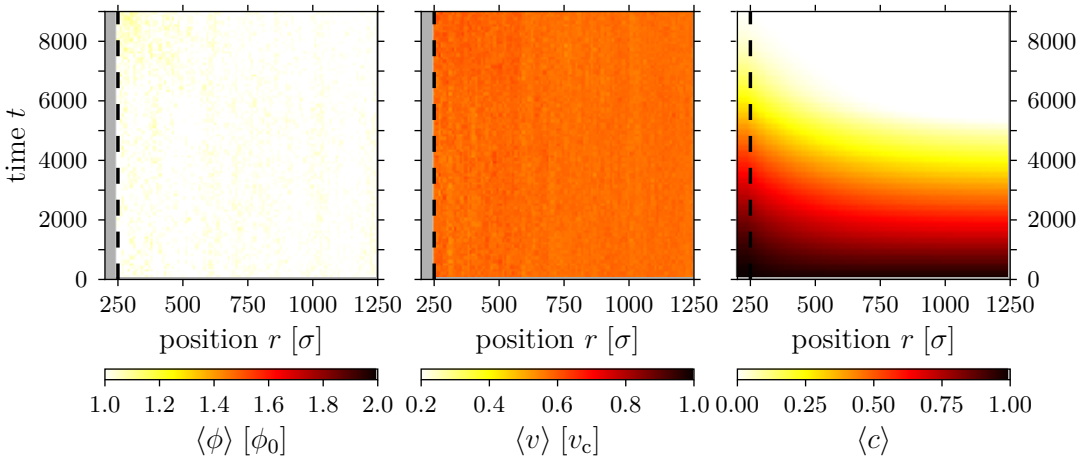

(e) $p_{\text{turn}} = 1.25 \times 10^{-6}$

Figure 5.31.: Space-time plots of mean local filling fraction $\langle\phi\rangle$, mean speed $\langle v\rangle$ and mean oxygen concentration $\langle c\rangle$ for systems with varying p_{turn}

slower. This is due to the fact that the oxygen diffusion out of the bubble slows down because the concentration gradient in the system reduces when no band forms. As a direct consequence, the band itself decelerates: Because fewer particles are part of it, consumption inside it is smaller, which is why it contacts the bubble at later times for smaller p_{turn}. The same gradual decline of all features with declining p_{turn} is also visible for $g(\Delta r)$ and $C_1^{re}(r,t)$ that we display in Fig. A.14.

5.3.6. Aerotactic mechanism

Figures 5.32(a) and 5.32(b) show space-time plots of the evolution of a system with the Harris rule (Eq. (3.12)) and the Anti-Harris rule (Eq. (3.13)) applied as aerotactic

mechanisms, i.e. as rules determining p_{turn}. We observe that neither of them leads to the formation of a dense area or, let alone, a migrating band. The same applies to the correlation functions displayed in Fig. A.15. This is clearly due to the fact the Harris rule as used here stems from an anaerobic scenario where bacteria perform electrokinesis rather than aerotaxis [30]. However, we will see in Chap. 5.4.2 that with slight further modifications of our model we can reproduce behaviour similar to that in the reference.

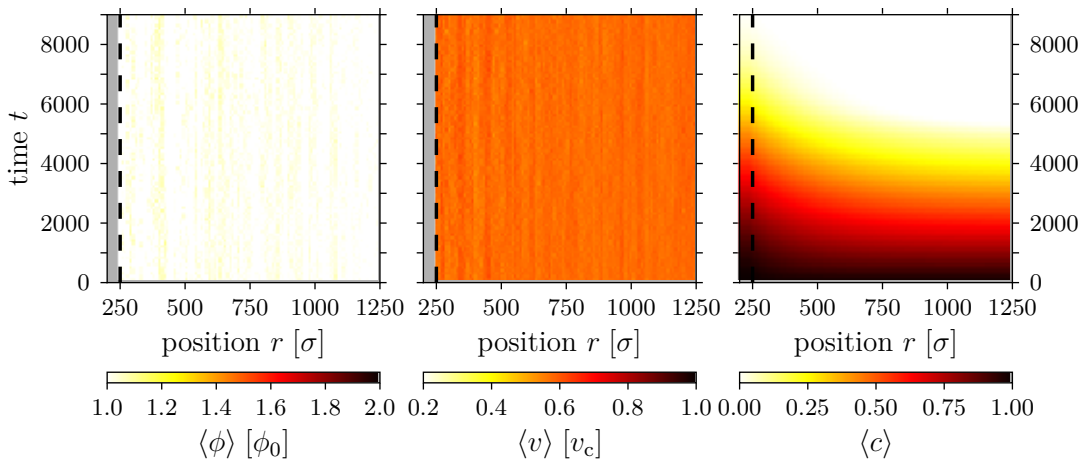

(a) Harris reversal rule

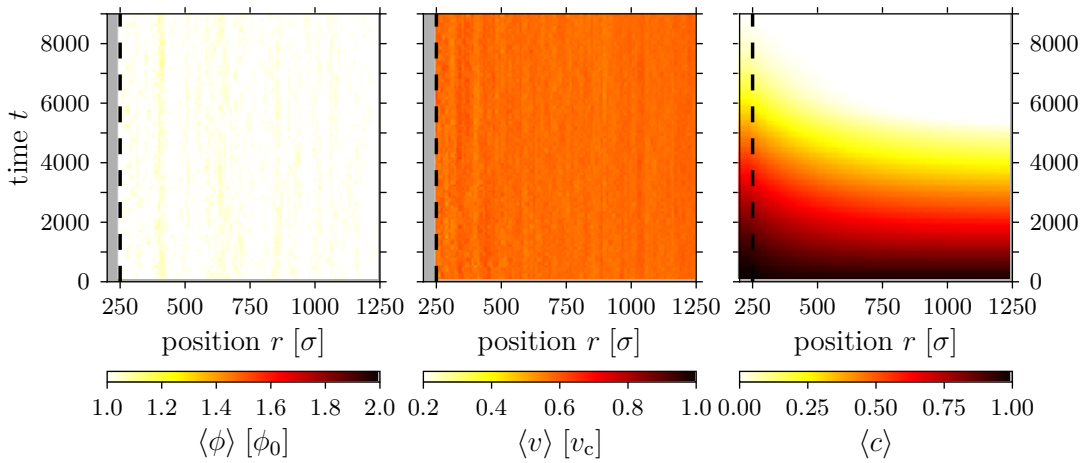

(b) Anti-Harris reversal rule

Figure 5.32.: Space-time plots of mean local filling fraction $\langle\phi\rangle$, mean speed $\langle v\rangle$ and mean oxygen concentration $\langle c\rangle$ for systems with other aerotactic mechanisms

5.4. Extension to different models

5.4.1. Steady oxygen inflow into the bubble

In this chapter we discuss a system that has a steady inflow of oxygen into the bubble, i.e. a two-dimensional version of the one-dimensional system in the experiment displayed in Fig. 2.4. To this end, we set c_0 to a constant value in the whole system initially like in Chap. 5.1, but while the oxygen is consumed in the system, its concentration stays constant inside the bubble. To accelerate the evolution of the system, we set $\kappa = 3 \times 10^{-3}$. Additionally we account for the toxicity of oxygen now by setting $k_1 = k_2 = 5$, which means that particles want to escape regions with both

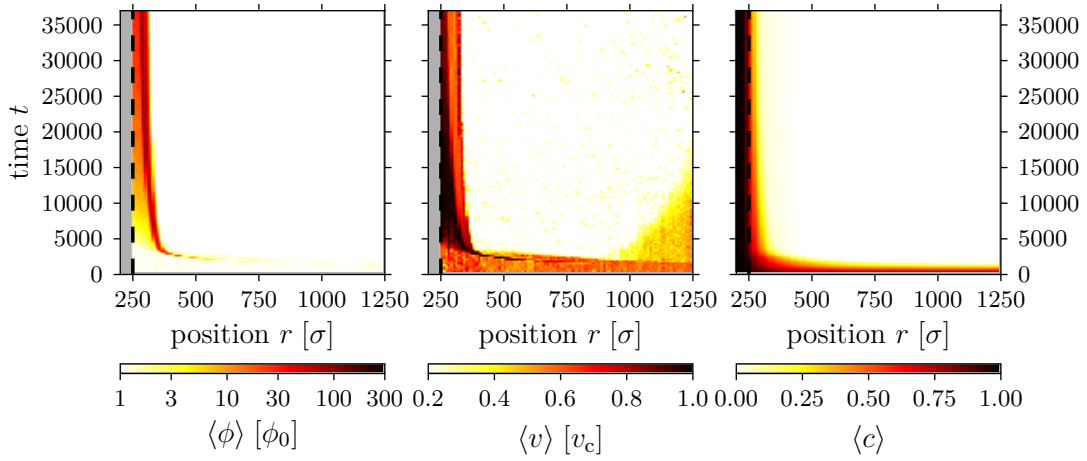

(a) $c_0 = 1$

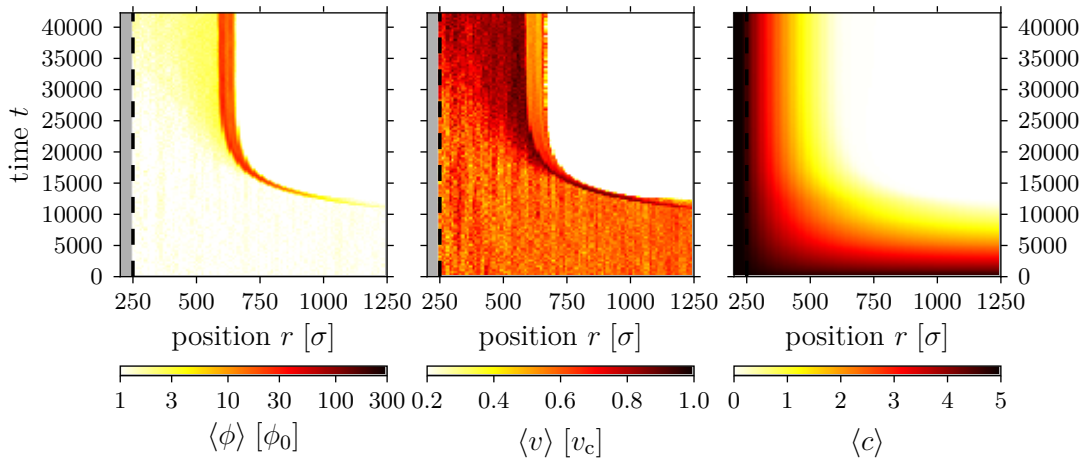

(b) $c_0 = 5$

Figure 5.33.: Space-time plots of mean local filling fraction $\langle\phi\rangle$, mean speed $\langle v\rangle$ and mean oxygen concentration $\langle c\rangle$ for systems with steady oxygen supply

too high and too low oxygen now. Apart from these changes, we use the parameters given in Tab. 5.1.

The temporal evolution of the system for $c_0 = 1$ and $c_0 = 5$ is displayed in Fig. 5.33. Just as in Chap. 5.1 we can see that a dense region forms and approaches the centre. However, this time the propagation stops and the system seems to settle into a steady state. This behaviour is particularly visible for $c_0 = 5$ in Fig. 5.33(b).

The correlation functions in Fig. A.16 do not show further surprising results: From $g(\Delta r)$ we can learn once more that the band is denser for $c_0 = 1$ than for $c_0 = 5$. $C_1^{re}(r,t)$ tells us three things: Firstly, the initial, migrating phase is marked by a negative amplitude, just as for systems without constant oxygen supply. Secondly, the slow particles behind the band keep their tendency to approach the band, indicated by the large, blue regions. Thirdly, one could have supposed that a migrating band forms also for too high concentrations, moving away from the bubble. However, this is not the case because the threshold concentration between too high and ideal oxygen concentration is never reached in this region, contrasting the situation for larger r.

5.4.2. Harris model

In this chapter we mimic a situation similar to the one described in [30]: There, the authors study the anaerobic behaviour of *S.o.* in presence of an insoluble electron acceptor (IEA). They conclude that only after a bacterium has contacted the IEA its motility undergoes changes in both speed and turning frequency, i.e. both are increased. This behaviour will finally make the particles congregate close the IEA, as is also depicted in Fig. 2.6.

To approximate this configuration as closely as possible, we vary our model in the following way: We consider again a system with the Harris reversal rule (Eq. (3.12)), but also make use of Eq. (3.6) as a speed rule, i.e. the speed is the base speed plus an additional term proportional to the oxygen concentration. Another major modification is that these two changes in motility only take effect after a particle has contacted the bubble. By this means of these variations we have almost reproduced the anaerobic conditions described above.

Figures 5.34(a) and 5.34(b) present space-time plots of $\langle\phi\rangle$, $\langle v\rangle$ and $\langle c\rangle$ for two systems with these rules, averaged over 20 simulations. Additionally, in Fig. 5.34(a) p_{turn} is ten times higher than in Fig. 5.34(b). We can see that we do not obtain a propagating band. However, we can observe that the particles congregate next to

the bubble in the first case, while there is no feature visible in the second. This is a behaviour very similar to that described in [30].

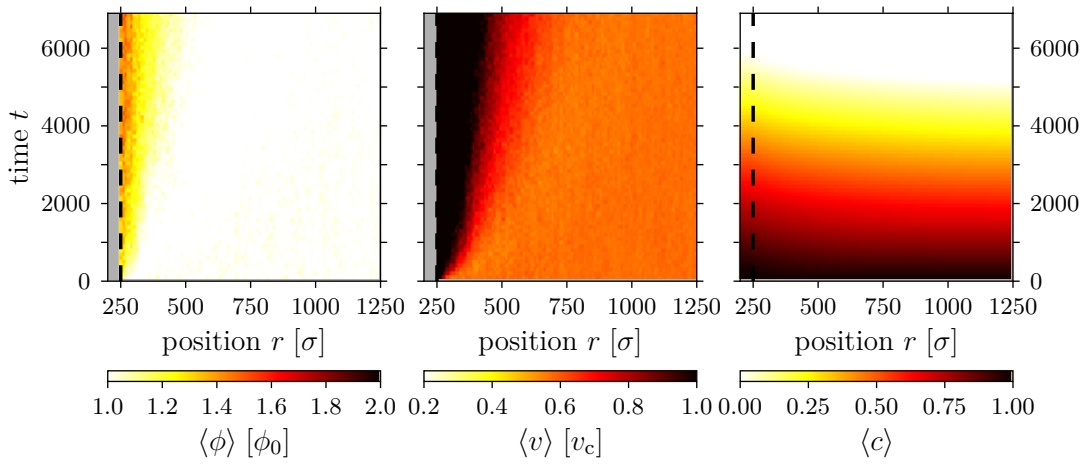

(a) High p_{turn}

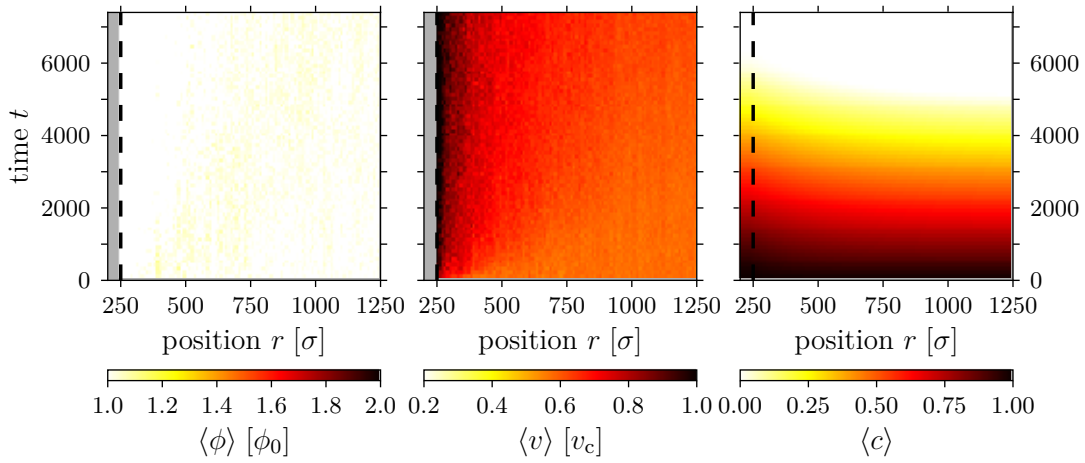

(b) Low p_{turn}

Figure 5.34.: Space-time plots of mean local filling fraction $\langle\phi\rangle$, mean speed $\langle v\rangle$ and mean oxygen concentration $\langle c\rangle$ for systems following the Harris model

6. Summary and outlook

In the following we want to summarise our findings from the previous chapters. Also, we want to point out how our model can be improved and which kind of future studies are possible in this area, if not necessary.

6.1. Summary

We have shown that our model, based on a MD simulation of self-propelled particles interacting with an oxygen field, is able to reproduce the aerobic behaviour of bacteria, such as *Shewanella oneidensis*: If the oxygen concentration in the system sinks locally below a threshold value, the formation of a migrating aerotactic band following a concentration gradient in the system can be observed (see Chap. 5.1).

The formation of the aerotactic band is robust under changes of many of the parameters of the system: We have shown that variations of the thermal noise η (see Chap. 5.2), the filling fraction ϕ (see Chap. 5.3.1), the functional dependence of the speed on the local concentration (see Chap. 5.3.2) or the bacterial consumption rate κ (see Chap. 5.3.3) do not inhibit band formation. This is only partly true for other parameters, such as the amount of oxygen stored in the bubble (see Chap. 5.3.4) and the frequency of orientation reversals f_{turn} and the underlying probability p_{turn} (up to a certain value, see Chap. 5.3.5), respectively: Upon decrease, these lead to a drastic reduction or even disappearance of the effects observed. However, even more important than the magnitude of the turning probability is the underlying model: We have seen that a band only forms if we choose p_{turn} according to the Mazzag motility rule (see Chap. 5.3.6). The key difference between this rule and the other two is that it includes buffer regions where p_{turn} does not only depend on the local concentration, but on the orientation of a particle, too. By this means the Mazzag rule is also the only mechanism tested here that actually accounts for *tactic* behaviour, while the other two depict *kinetic* scenarios (see Chap. 2.1.3).

The quantities we use to analyse our system show corresponding results: While

we do not see any particular features in them during the regular, initial diffusion phase, all of them show amplitudes during the propagation phase of the band. This includes both the single-particle functions $C_1^{ee}(t, \Delta t)$ and $C_1^{re}(r, t)$ and the many-particle quantities $C_1^{ee}(r, \Delta r)$ and $g(\Delta r)$: The latter shows that the band is indeed a very dense region constantly attracting more particles. We would have expected to see a more distinct structure where one can make out different neighbour shells like in a fluid, but apart from next neighbours this is not the case. This is due to the comparably low filling fraction we use in our simulations, as can be seen from the weak second peaks for $\phi_0 = 10^{-2}$ in Fig. A.9. The correlation functions $C_1^{ee}(t, \Delta t)$ and $C_1^{ee}(r, \Delta r)$ give strong evidence for temporal and spatial correlations during the time period and at the position of the band. The scalar product of orientation and position $C_1^{re}(r, t)$ confirms these observations. While the former quantities are also easily accessible in an experiment, this is not the case for the latter: In order to calculate this quantity from video data, one needs to define positions and orientations with respect to the oxygen source in the system, which probably has a more complex geometry than our cylindrical air bubble.

The "second" correlation functions, i.e. $C_2^{ee}(r, \Delta r)$, $C_2^{ee}(t, \Delta t)$ and $C_2^{re}(r, t)$, show features only if the noise η is sufficiently low: While there is no amplitude for $\eta = 5$, this is the case for $\eta = 1$ and, even more pronounced, for $\eta = 0.1$. On the one hand, these additional correlations are due to particles that move perpendicular to the oxygen gradient; on the other hand, because collisions are rare in out dilute system, particles keep their orientation if not rotated due to noise, which is the reason for the amplitudes $C_2^{ee}(t, \Delta t)$ shows.

6.2. Comparison with analytical predictions

In Chap. 2.2.6 we have proven that for a reasonable, space-dependent diffusivity the theoretical solution to the diffusion equation is in fact a peaked function, similar to the distribution we observe in our simulations. The assumption that the diffusivity is high in an aerobic region, while it is low in an anaerobic environment is confirmed by the actual diffusivities measured in the system (see Chap. 5.2.6). We would have expected this agreement because the diffusion equation is equivalent to a description by means of a Langevin equation, which is at the core of our model.

Another analytical solution for the steady-state density of an aerotactic band can be found in [40]: For a one-dimensional system with constant oxygen supply at the

meniscus, the authors propose a function consisting of six intervals in which the oxygen concentration is equal to a particular value. The distance of the band from the bubble and its width can then be calculated from the input parameters such as the oxygen concentration at the meniscus and the bacterial consumption rate.

6.3. Comparison with literature values

The statistics of our band are at least qualitatively in accordance with the experimental results: From Fig. 2.4 we can learn that the distance between band and meniscus rises with increasing oxygen concentration at the latter. We can confirm this in Chap. 5.4.1. The same applies to the width of the band, as is observed by the authors of [40] and [43], respectively, in experiments with *Azospirillum brasilense*. However, actual values differ strongly, as the band appears at a distance of about 2 mm, which is much farther away than in our system, where it settles close to the bubble. The width of the band is smaller than expected, too, especially for low c_0 ($\mathcal{O}(50\,\mu\text{m})$ in our simulations versus $\mathcal{O}(200\,\mu\text{m})$ in experiments). These contradictions indicate that some of our model parameters are not chosen appropriately, presumably the consumption rate κ.

When we compare the diffusion constants we determined in Chap. 5.2.6 to the literature values for *V. alginolyticus*, we find a difference of one order of magnitude: While for the latter it has been found that $D = 210\,\mu\text{m}^2\,\text{s}^{-1}$ (see Chap. 2.2.2), our particles diffuse with $D \approx 1\ \sigma^2/\text{time unit} \equiv 20\,\mu\text{m}^2\,\text{s}^{-1}$. This is partly due to the fact that we have taken into consideration all particles in our system, independent of their speed. If we constrain the calculation of D to $v_0 > v_c/2$, i.e. we consider only motile particles, we obtain values roughly twice as large as before. Another reason for the weak diffusivity is the high reversal probability: While our particles turn on average 0.125 (0.625) times per time unit in the aerobic (anaerobic) regime, i.e. 2.5 (12.5) times per second, Mazzag suggests to use a reversal frequency of 0.1 (0.5) times per second. Dimming that quantity would hence lead to a further increase of D, thus approximately yielding its expected order of magnitude.

We have shown that the Péclet number for our system is $\mathcal{O}(10)$ and depends mainly on the turning frequency, not the noise. This tells us that active propulsion is more important than diffusion for the locomotion of the particles, especially in an anaerobic environment. The value of $\mathscr{P}$ does not depend on the choice of particles like D does, because both $\bar{v}$ and D grow about the same size when we consider only

fast particles and thus do not change $\mathscr{P}$ according to Eq. (5.11). With this order of magnitude, our value is larger than often found for single bacteria or cyanobacteria ($\mathcal{O}(10^{-2} - 10^{-3})$, [44]), but smaller than for other flagellated microorganisms, such as certain volvocalean green algae ($\mathcal{O}(10^{2})$, [45]).

6.4. Outlook and possible improvements

So far we have only adapted some of the model parameters to real quantities measured in an experiment. To be able to transfer our results to the experimental outcomes, this needs to happen with as many parameters as possible. At the time being, we do not know about some of them, so instead we choose suitable values that facilitate the evolution of the system as expected. This problem applies especially to quantities intrinsic to the bacteria, e.g. their actual turning frequencies and oxygen consumption rates depending on the aerobicity of the environment. Apart from these simple parameters, it also concerns the models we decided to use in our simulations, such as the aerotactic mechanism, the initial speed distribution or the dependence of the speed on the oxygen concentration. We are confident to infer some of the dynamic quantities in question from a particle tracking system that can be used to analyse data from a real colony of *S.o.*

In order to systematically analyse higher filling fractions it makes sense not only to decrease the size of the system, but also to increase the number of particles N_{part}. So far this is hardly possible because it drastically prolongs the time needed for a single simulation. In Chap. 5.3.3 we have seen that too low a number of particles additionally leads to unreasonable results when a second band arises that propagates away from the bubble. This disadvantage can be overcome by parallelising the code or reimplementing it as a version for GPU systems instead of CPU systems.

An advantage of our model is that it is very general: While most of our studies deal with a system with finite amount of oxygen, we have shown that we are also able to reproduce a situation where oxygen flows steadily into the system (see Chap. 5.4.1). Furthermore, we have tried to imitate the experimental setup described in [29] in Chap. 5.4.2 and are able to capture some of the features observed: The authors describe an anaerobic situation where bacteria are located in vicinity to an insoluble electron acceptor and behave kinetic instead of tactic, i.e. without a concentration gradient, but they still vary their motility after contacting the acceptor, finally leading to a congregation around the IEA. Our work focusses clearly on the aerobic

behaviour of *S.o.*; however, we describe in Chap. 2 in how far their behaviour under anaerobic conditions is special and why it deserves attention. Hence, it is worthwhile to follow and study these characteristic traits in a separate project.

Apart from these two model variations, we can go even further: Even if this work is motivated by and based on observations made on *S.o.*, our code does not rely on a feature unique to these bacteria. As long as we deal with self-propelled particles performing aerotaxis we can adapt the parameters to make the model fit the species in question. Furthermore, by this means we can also find out if the dynamics of the latter can be reproduced by our code correctly or if there are other features not included in the model.

A. Appendix: Additional plots

Regular system

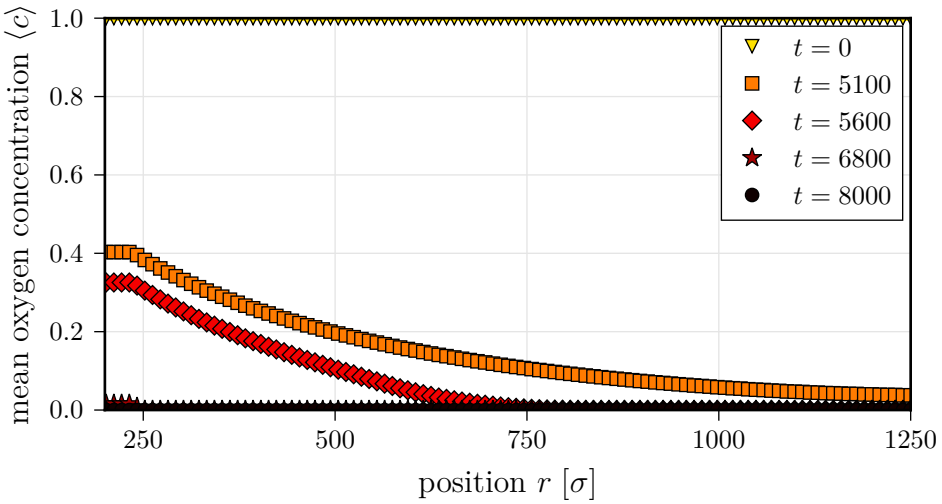

Figure A.1.: Oxygen profiles for the regular system

Low noise

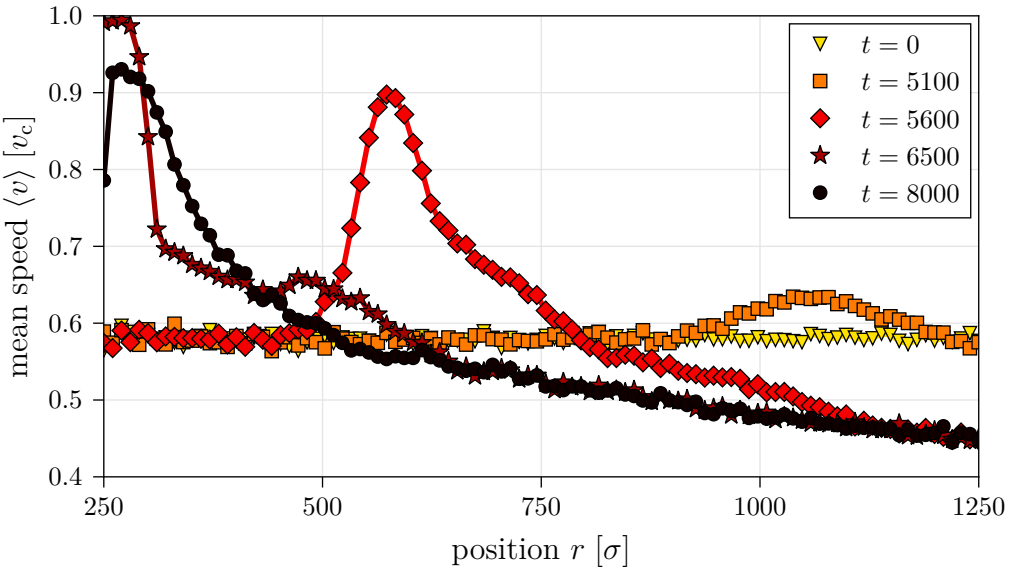

Figure A.2.: Speed profiles for a system with $\eta = 0.1$

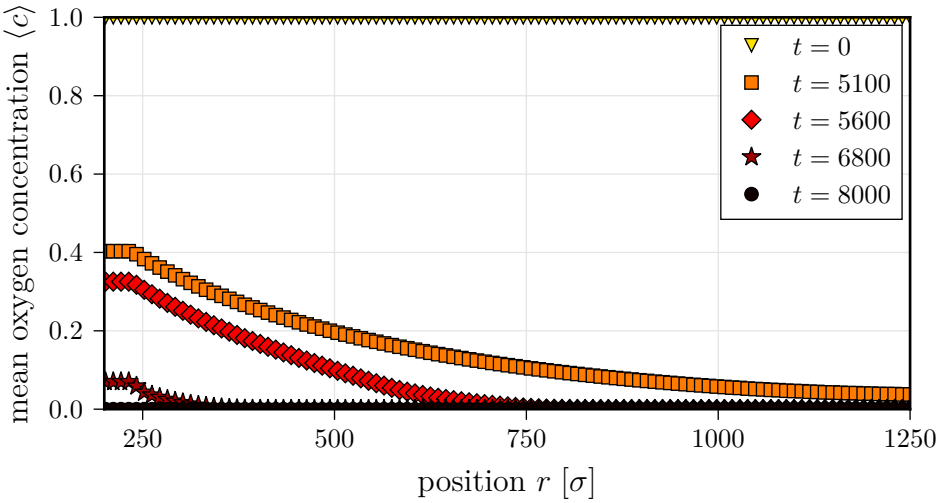

Figure A.3.: Oxygen profiles for a system with $\eta = 0.1$

Intermediate noise

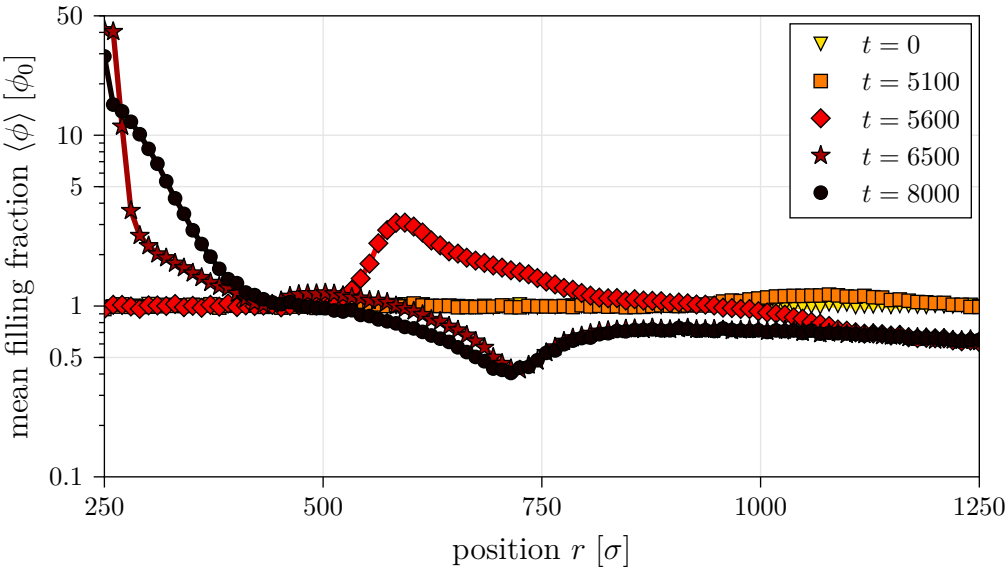

Figure A.4.: Filling fraction profiles for a system with $\eta = 1$

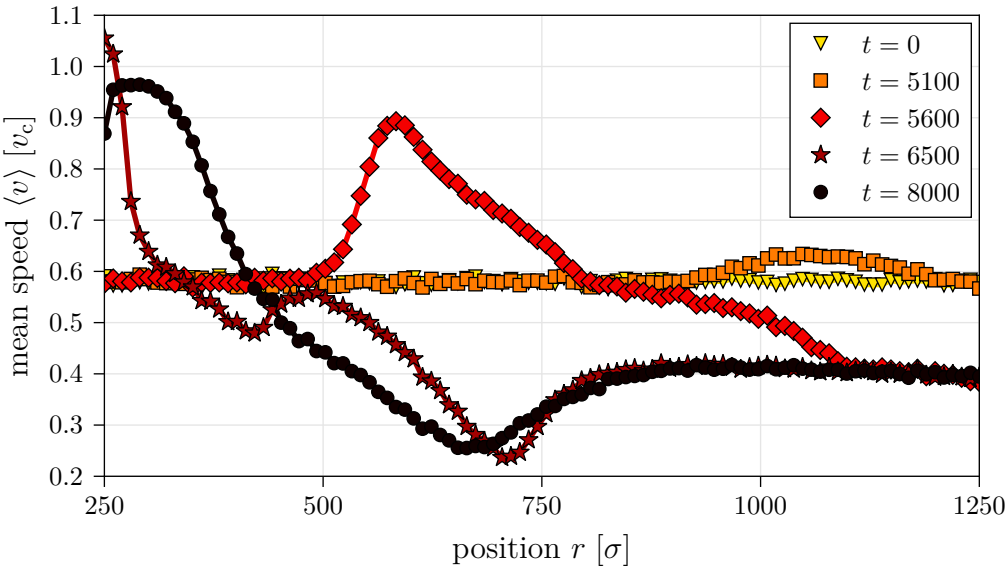

Figure A.5.: Speed profiles for a system with $\eta = 1$

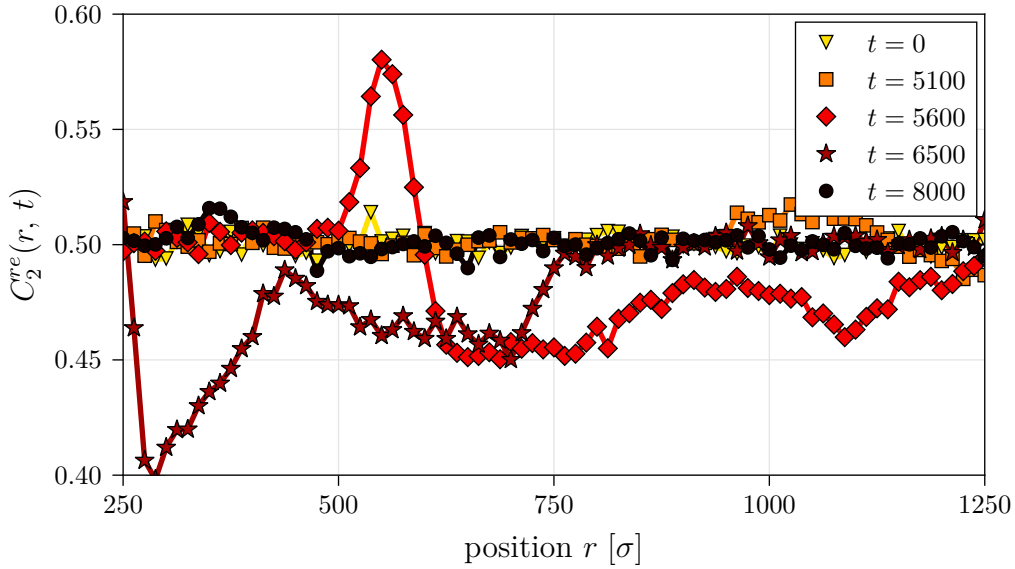

Figure A.6.: Profiles of position-orientation scalar product $C_2^{re}(r, t)$ for a system with $\eta = 1$

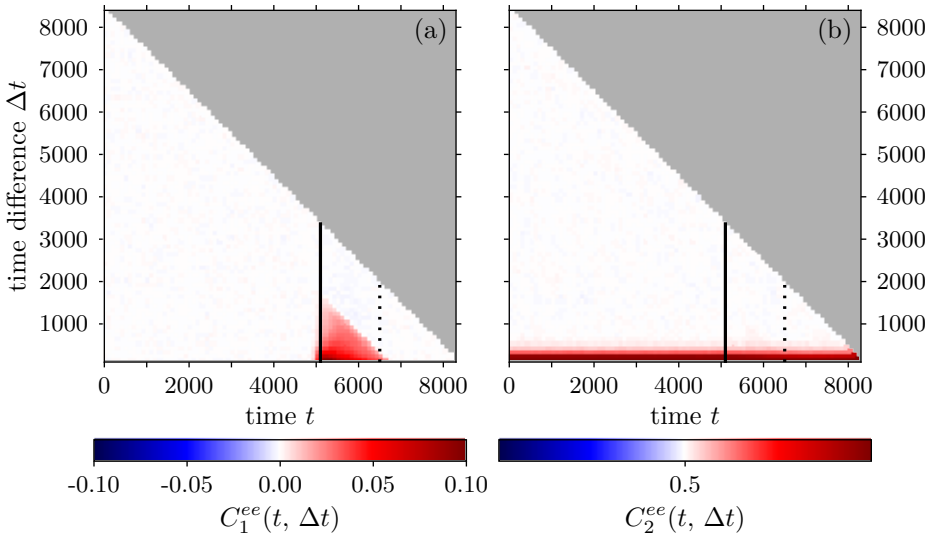

Figure A.7.: Temporal orientation correlation functions for a system with $\eta = 1$

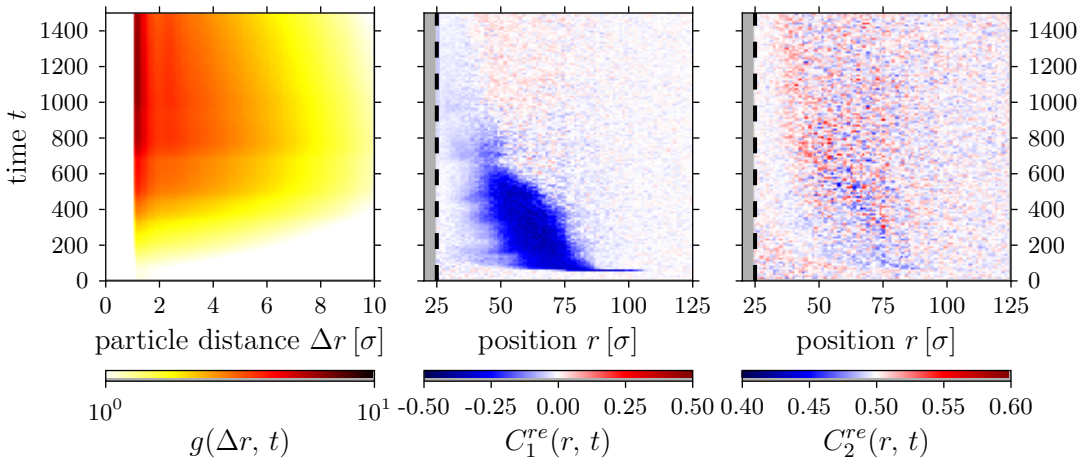

Figure A.8.: Space-time plots of radial distribution function $g(\Delta r, t)$ and position-orientation scalar products $C^{re}_{1/2}(r, t)$ for a system with $\phi_0 = 10^{-2}$

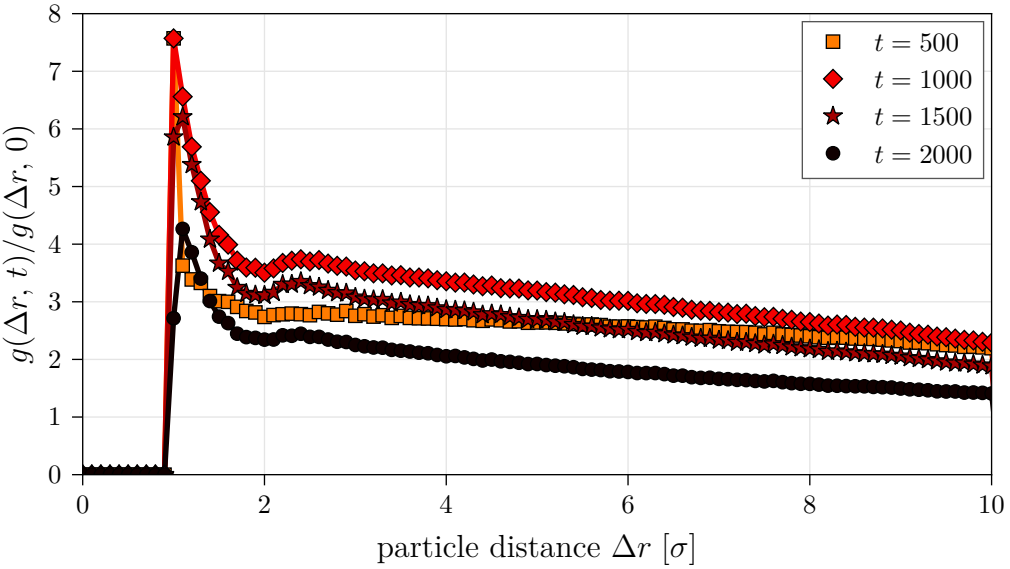

Figure A.9.: $g(\Delta r, t)$ for a system with $\phi_0 = 10^{-2}$

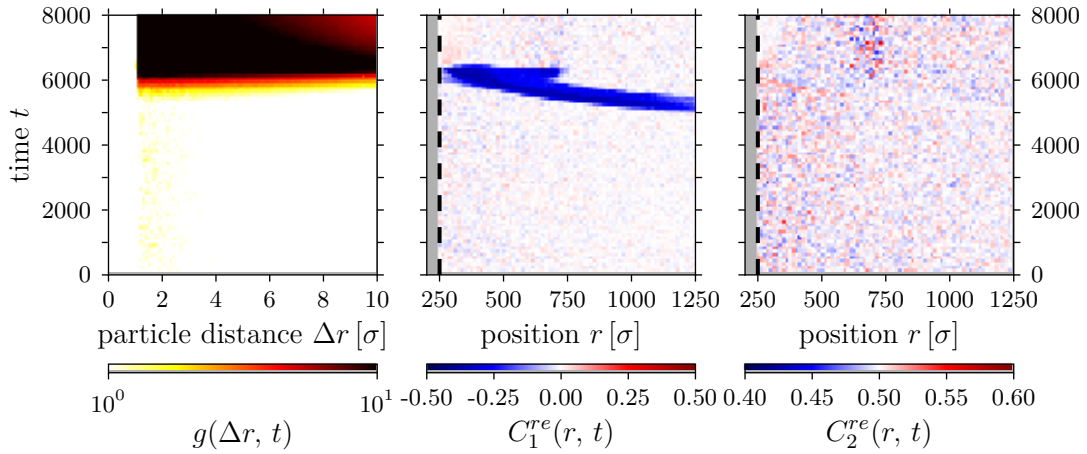

(a) Two-state speed model

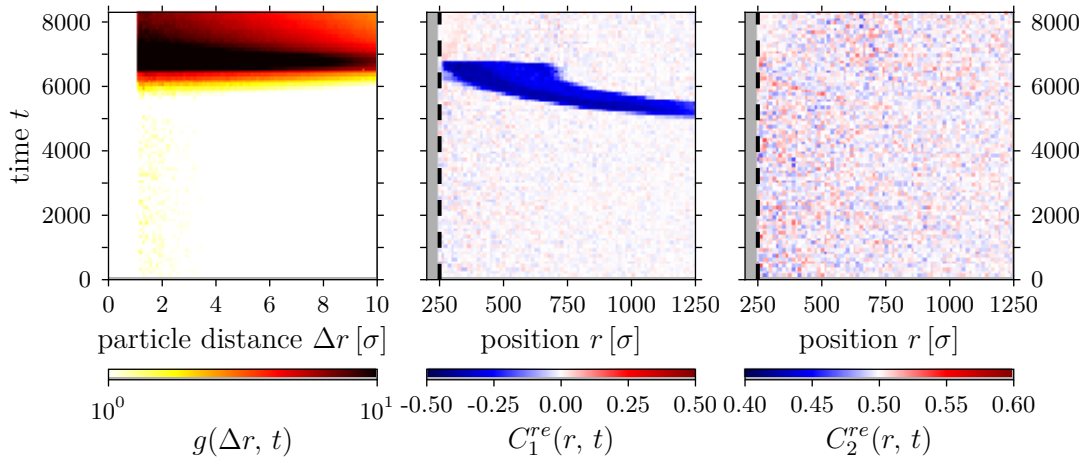

(b) Speed proportional to the concentration

Figure A.10.: Space-time plots of radial distribution function $g(\Delta r, t)$ and position-orientation scalar products $C^{re}_{1/2}(r, t)$ for systems with other speed rules

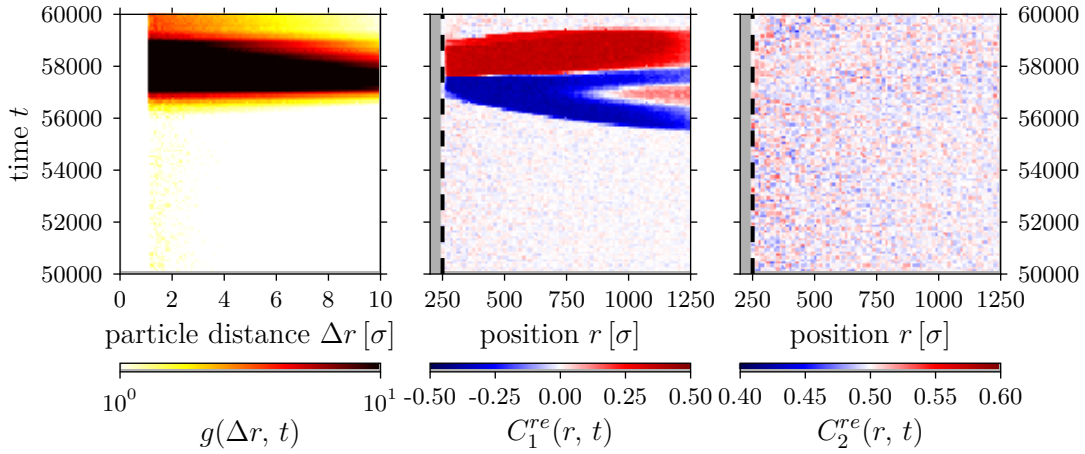

Figure A.11.: Space-time plots of radial distribution function $g(\Delta r, t)$ and position-orientation scalar products $C^{re}_{1/2}(r, t)$ for a system with $\kappa = 10^{-4}$

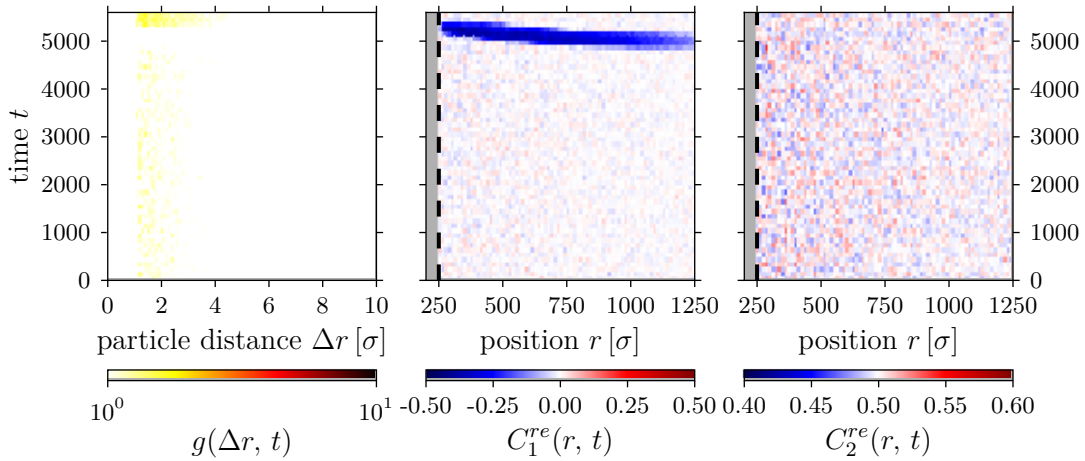

Figure A.12.: Space-time plots of radial distribution function $g(\Delta r, t)$ and position-orientation scalar products $C^{re}_{1/2}(r, t)$ for a system with $N_{\text{boxes, virtual}} = 0$

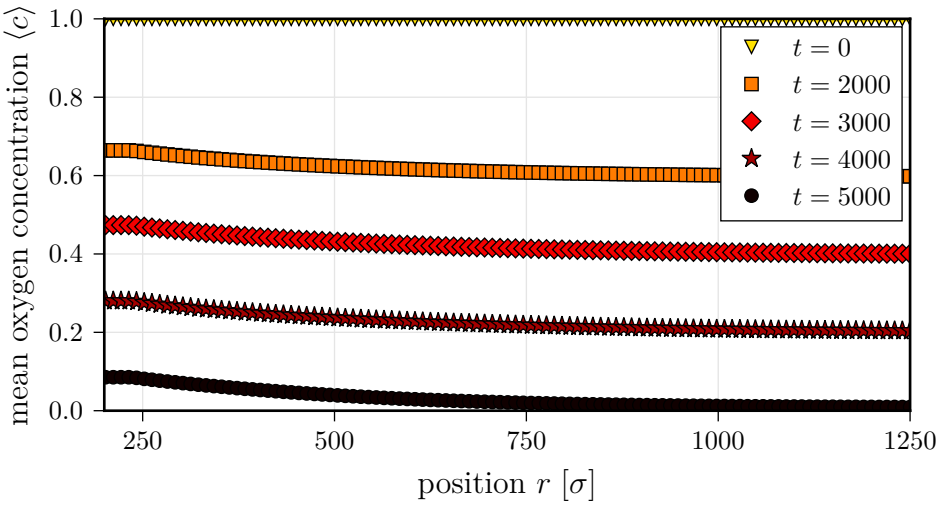

Figure A.13.: Oxygen concentration profiles for a system with $N_{\text{boxes, virtual}} = 0$

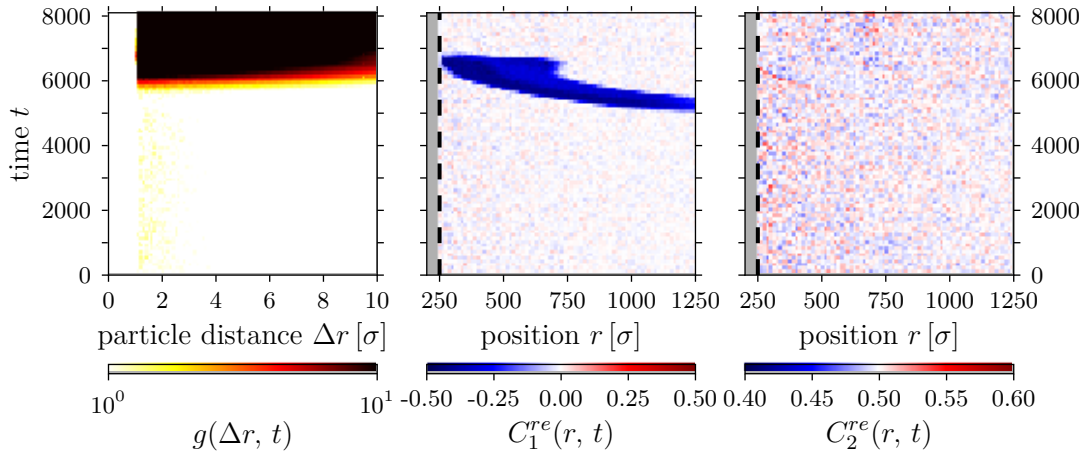

(a) $p_{\text{turn}} = 1.25 \times 10^{-2}$

Figure A.14.: Space-time plots of radial distribution function $g(\Delta r, t)$ and position-orientation scalar products $C^{re}_{1/2}(r, t)$ for systems with varying p_{turn}

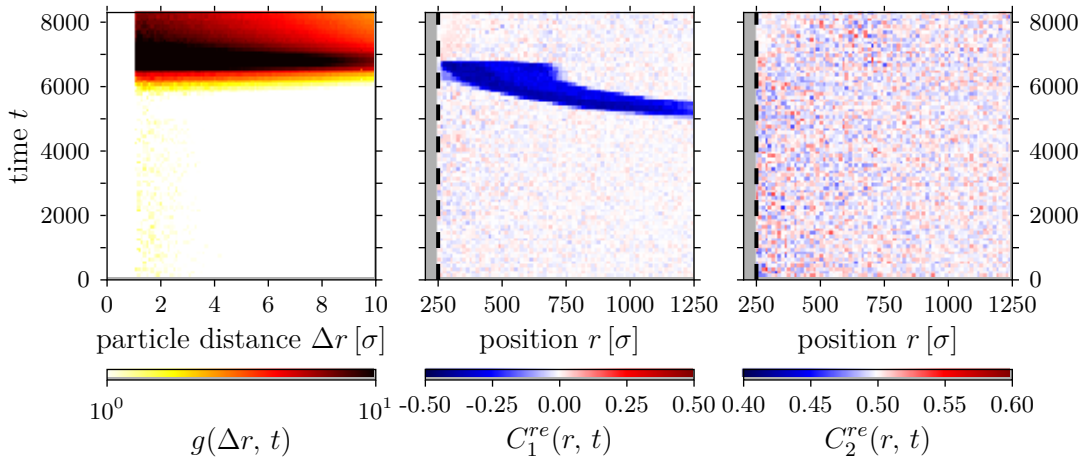

(b) $p_{\text{turn}} = 1.25 \times 10^{-3}$

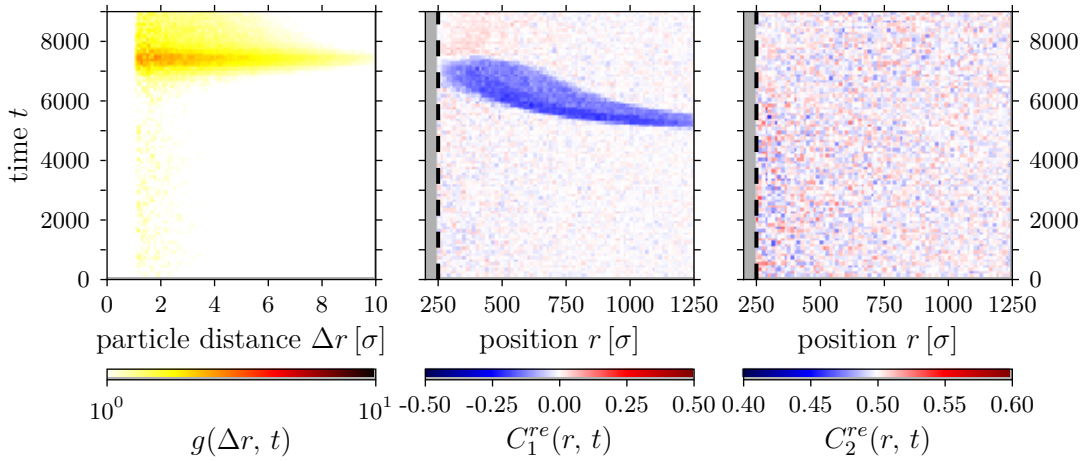

(c) $p_{\text{turn}} = 1.25 \times 10^{-4}$

Figure A.14.: Space-time plots of radial distribution function $g(\Delta r, t)$ and position-orientation scalar products $C_{1/2}^{re}(r, t)$ for systems with varying p_{turn}

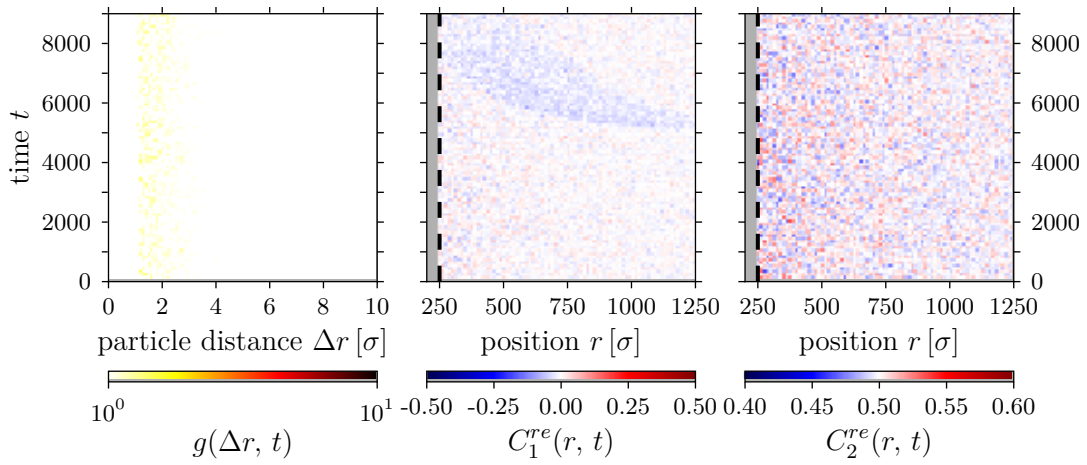

(d) $p_{\text{turn}} = 1.25 \times 10^{-5}$

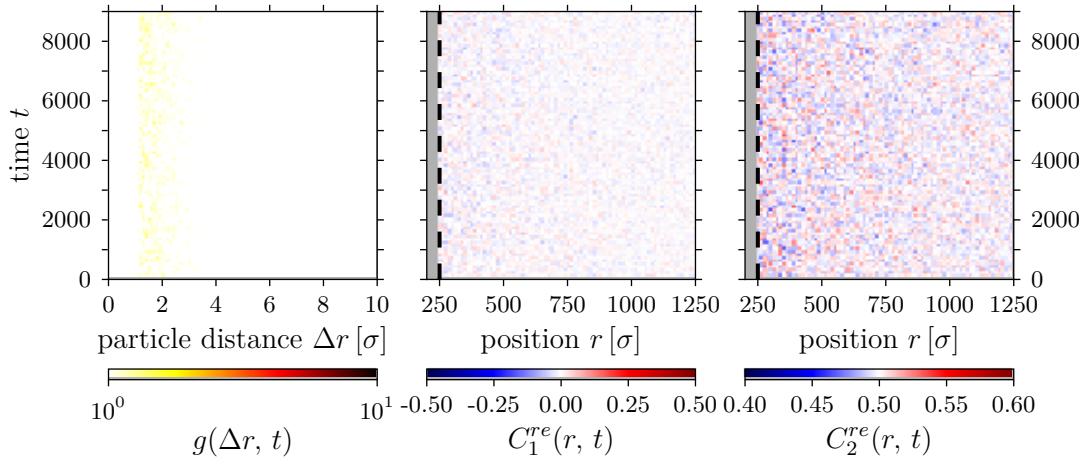

(e) $p_{\text{turn}} = 1.25 \times 10^{-6}$

Figure A.14.: Space-time plots of radial distribution function $g(\Delta r, t)$ and position-orientation scalar products $C_{1/2}^{re}(r, t)$ for systems with varying p_{turn}

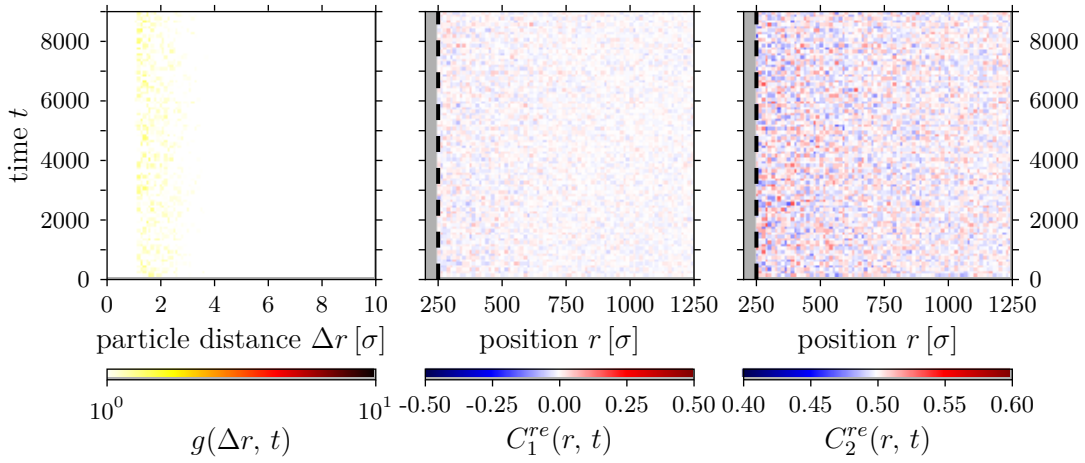

(a) Harris reversal rule

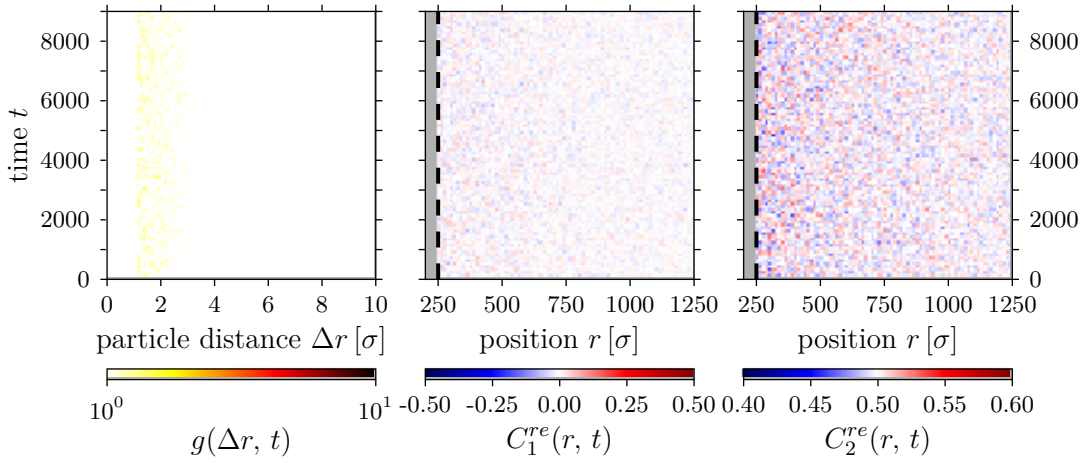

(b) Anti-Harris reversal rule

Figure A.15.: Space-time plots of radial distribution function $g(\Delta r, t)$ and position-orientation scalar products $C^{re}_{1/2}(r, t)$ for systems with other aerotactic mechanisms

Extension to different models

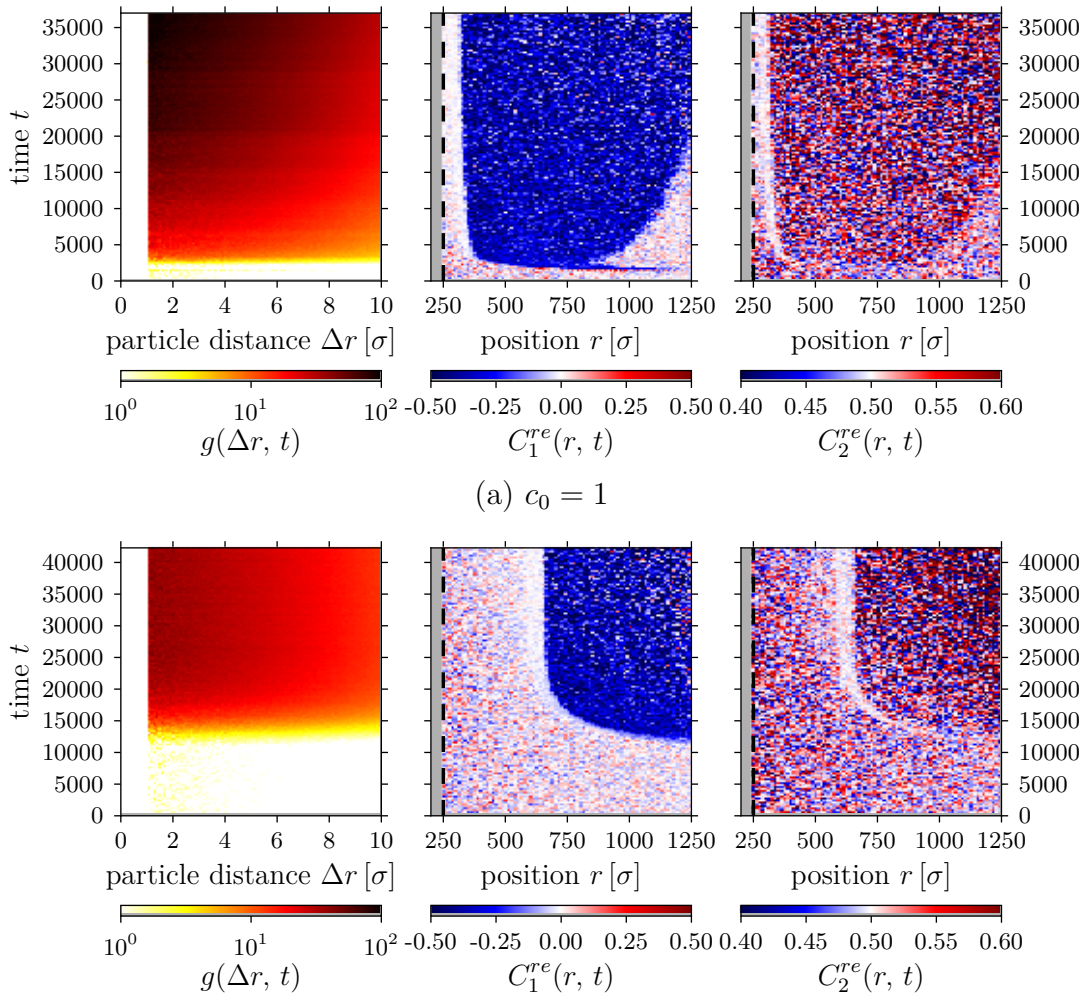

(a) $c_0 = 1$

(b) $c_0 = 5$

Figure A.16.: Space-time plots of radial distribution function $g(\Delta r, t)$ and position-orientation scalar products $C_{1/2}^{re}(r, t)$ for systems with steady oxygen supply

Bibliography

[1] E. Gellhorn and F. Alverdes, in *Energieumsatz*, Handbuch der Normalen und Pathologischen Physiologie No. 8 / 1, edited by F. Alverdes, H. J. Deuticke, G. Embden, W. O. Fenn, E. Fischer, H. Fühner, E. Gellhorn, H. Hentschel, K. Hürthle, F. Jamin, H. Jost, F. Kramer, F. Külz, E. Lehnartz, O. Meyerhof, S. M. Neuschlosz, O. Riesser, H. Sierp, E. Simonson, J. Spek, W. Steinhausen, K. Stern, and K. Wachholder (Springer Berlin Heidelberg, 1925) pp. 37–69.

[2] T. Vicsek, A. Czirók, E. Ben-Jacob, I. Cohen, and O. Shochet, Phys. Rev. Lett. **75**, 1226 (1995).

[3] H. H. Hau and J. A. Gralnick, Annu. Rev. Microbiol. **61**, 237 (2007).

[4] K. Venkateswaran, D. P. Moser, M. E. Dollhopf, D. P. Lies, D. A. Saffarini, B. J. MacGregor, D. B. Ringelberg, D. C. White, M. Nishijima, H. Sano, J. Burghardt, E. Stackebrandt, and K. H. Nealson, Int. J. Syst. Bacteriol. **49**, 705 (1999).

[5] K. M. Thormann, R. M. Saville, S. Shukla, D. A. Pelletier, and A. M. Spormann, J. Bacteriol. **186**, 8096 (2004).

[6] J. K. Fredrickson, M. F. Romine, A. S. Beliaev, J. M. Auchtung, M. E. Driscoll, T. S. Gardner, K. H. Nealson, A. L. Osterman, G. Pinchuk, J. L. Reed, D. A. Rodionov, J. L. M. Rodrigues, D. A. Saffarini, M. H. Serres, A. M. Spormann, I. B. Zhulin, and J. M. Tiedje, Nat. Rev. Micro. **6**, 592 (2008).

[7] J. F. Heidelberg, I. T. Paulsen, K. E. Nelson, E. J. Gaidos, W. C. Nelson, T. D. Read, J. A. Eisen, R. Seshadri, N. Ward, B. Methe, R. A. Clayton, T. Meyer, A. Tsapin, J. Scott, M. Beanan, L. Brinkac, S. Daugherty, R. T. DeBoy, R. J. Dodson, A. S. Durkin, D. H. Haft, J. F. Kolonay, R. Madupu, J. D. Peterson, L. A. Umayam, O. White, A. M. Wolf, J. Vamathevan, J. Weidman, M. Impraim, K. Lee, K. Berry, C. Lee, J. Mueller, H. Khouri, J. Gill, T. R.

Utterback, L. A. McDonald, T. V. Feldblyum, H. O. Smith, J. C. Venter, K. H. Nealson, and C. M. Fraser, Nat. Biotech. **20**, 1118 (2002).

[8] Y. A. Gorby, S. Yanina, J. S. McLean, K. M. Rosso, D. Moyles, A. Dohnalkova, T. J. Beveridge, I. S. Chang, B. H. Kim, K. S. Kim, D. E. Culley, S. B. Reed, M. F. Romine, D. A. Saffarini, E. A. Hill, L. Shi, D. A. Elias, D. W. Kennedy, G. Pinchuk, K. Watanabe, S. Ishii, B. Logan, K. H. Nealson, and J. K. Fredrickson, Proc. Natl. Acad. Sci. USA **103**, 11358 (2006).

[9] R. H. Luchsinger, B. Bergersen, and J. G. Mitchell, Biophys. J. **77**, 2377 (1999).

[10] S. Bubendorfer, M. Koltai, F. Rossmann, V. Sourjik, and K. M. Thormann, Proc. Natl. Acad. Sci. USA **111**, 11485 (2014).

[11] R. Stocker, Proc. Natl. Acad. Sci. USA **108**, 2635 (2011).

[12] L. Xie and X.-L. Wu, Biophys. J. **107**, 1712 (2014).

[13] C. Qian, C. C. Wong, S. Swarup, and K.-H. Chiam, Appl. Environ. Microbiol. **79**, 4734 (2013).

[14] J. Taktikos, *Modeling the random walk and chemotaxis of bacteria: aspects of biofilm formation*, Ph.D. thesis, Technische Universität Berlin (2013).

[15] H. C. Berg, Annu. Rev. Biophys. Bioeng. **4**, 119 (1975).

[16] C. Bücking, F. Popp, S. Kerzenmacher, and J. Gescher, FEMS Microbiol. Lett. **306**, 144 (2010).

[17] M. Y. El-Naggar, G. Wanger, K. M. Leung, T. D. Yuzvinsky, G. Southam, J. Yang, W. M. Lau, K. H. Nealson, and Y. A. Gorby, Proc. Natl. Acad. Sci. USA **107**, 18127 (2010).

[18] K. E. Pitts, P. S. Dobbin, F. Reyes-Ramirez, A. J. Thomson, D. J. Richardson, and H. E. Seward, J. Biol. Chem. **278**, 27758 (2003).

[19] H. von Canstein, J. Ogawa, S. Shimizu, and J. R. Lloyd, Appl. Environ. Microbiol. **74**, 615 (2008).

[20] J. A. Gralnick and D. K. Newman, Mol. Microbiol. **65**, 1 (2007).

[21] J. Adler, Science **153**, 708 (1966).

[22] A. Kühn, in *Handbuch der Normalen und Pathologischen Physiologie*, edited by A. Bethe, G. v Bergmann, G. Embden, and A. Ellinger (Springer Berlin Heidelberg, 1929) pp. 17–35.

[23] R. P. Blakemore, Annu. Rev. Microbiol. **36**, 217 (1982).

[24] T. W. Engelmann, Pflüger, Arch. **25**, 285 (1881).

[25] M. Beijerinck, Zentralblatt Für Bakteriol. Parasitenkd. Infekt. Hyg. **14**, 827 (1893).

[26] J. Li, *Molecular mechanisms of behavioral responses in Shewanella oneidensis MR-1*, Ph.D. thesis, John Hopkins University (2009).

[27] D. L. Gunn, Anim. Behav. **23, Part 2**, 409 (1975).

[28] F. Schweitzer and J. D. Farmer, *Brownian Agents and Active Particles: Collective Dynamics in the Natural and Social Sciences* (Springer Science & Business Media, 2007).

[29] H. W. Harris, M. Y. El-Naggar, and K. H. Nealson, Biochem. Soc. Trans. **40**, 1167 (2012).

[30] H. W. Harris, M. Y. El-Naggar, O. Bretschger, M. J. Ward, M. F. Romine, A. Y. Obraztsova, and K. H. Nealson, Proc. Natl. Acad. Sci. USA **107**, 326 (2010).

[31] N. G. V. Kampen, in *Stochastic Processes in Physics and Chemistry (Third Edition)*, North-Holland Personal Library, edited by N. G. V. Kampen (Elsevier, Amsterdam, 2011) pp. 52–72.

[32] H. G. Othmer and T. Hillen, SIAM J. Appl. Math. **62**, 1222 (2002).

[33] E. M. Purcell, in *Physics and Our World* (WORLD SCIENTIFIC, 2013) pp. 47–67.

[34] W. M. Haynes, in *CRC Handbook of Chemistry and Physics* (CRC Press, 2013) 94th ed., pp. 6–250.

[35] H. G. Othmer, S. R. Dunbar, and W. Alt, J. Math. Biology **26**, 263 (1988).

[36] E. A. Codling, M. J. Plank, and S. Benhamou, J. R. Soc. Interface **5**, 813 (2008).

[37] E. F. Keller and L. A. Segel, J. Theor. Biol. **26**, 399 (1970).

[38] J. M. Ilnytskyi and M. R. Wilson, Comput. Phys. Commun. **148**, 43 (2002).

[39] J. D. Weeks, D. Chandler, and H. C. Andersen, J. Chem. Phys. **54**, 5237 (1971).

[40] B. C. Mazzag, I. B. Zhulin, and A. Mogilner, Biophys. J. **85**, 3558 (2003).

[41] T. J. Chung, in *Computational Fluid Dynamics* (Cambridge University Press, 2002) pp. 67–71.

[42] S. Vogel, in *Comparative Biomechanics: Life's Physical World (Second Edition)* (Princeton University Press, 2013) 2nd ed., p. 159.

[43] I. B. Zhulin, V. A. Bespalov, M. S. Johnson, and B. L. Taylor, J. Bacteriol. **178**, 5199 (1996).

[44] V. Magar, Q. J. Mech. Appl. Math. **56**, 65 (2003).

[45] C. A. Solari, S. Ganguly, J. O. Kessler, R. E. Michod, and R. E. Goldstein, Proc. Natl. Acad. Sci. USA **103**, 1353 (2006).